# Wide-bandgap Donor Polymers Based on Thiophene-Vinyl-Thiophene Ester (TVT-Ester) or Thiophene-Alkyloxime (TO) Units in Organic Solar Cells

by

Zhaoyi Yin

A thesis
presented to the University of Waterloo
in fulfillment of the
thesis requirement for the degree of
Master of Applied Science
in
Chemical Engineering (Nanotechnology)

Waterloo, Ontario, Canada, 2021

©Zhaoyi Yin 2021

# Author's Declaration

I hereby declare that I am the sole author of this thesis. This is a true copy of the thesis, including any required final revisions, as accepted by my examiners.

I understand that my thesis may be made electronically available to the public.

# Abstract

The organic solar cells (OSCs), a branch of the third-generation solar cell as a viable future energy resource has received a lot of attention in lab and industry today. The OSCs have advantages of low cost, light weight, flexible, and roll-to-roll printing for large area manufacture. The bulk heterojunction structure (BHJ) is wildly accepted in the active layer of OSCs, which is a blend film of donor polymer and acceptor material for efficient charge transfer. Recently, the combination of non-fullerene acceptors (NFAs) with wide-bandgap donor polymers as active layer has come to the forefront of OSC research, which has achieved high power conversion efficiency (PCE) over 18%.

In this work, we will introduce donor polymers in D-A copolymer structure, based on benzodithiophene (BDT) or polythiophene (PT) as the donor backbone unit combining with electron-withdrawing sidechains as the acceptor unit. Two novel series of polymers, thiophene-vinyl-thiophene easter (TVT-ester) polymer and thiophene-alkyloxime (TO) polymer based on different electron-withdrawing sidechains, were designed, synthesized, and characterized to function as wide-bandgap donor polymers in organic solar cells.

Among the designed TVT-ester polymers, the PEBDT exhibits planar backbone structure, low synthetic complexity, and high quenching efficiency with the non-fullerene acceptors $(3PS)_2$-SiPc and Y6, which is a promising candidate for OSCs. The solar cell device based on PEBDT:Y6 blend film had the highest PCE of 1.23%, with Jsc of 7.32 mA/cm$^2$, Voc of 0.54V, and FF of 31%. The carrier mobilities of blend film were calculated to be $1.37 \times 10^{-6}$ cm$^2$V$^{-1}$s$^{-1}$ ($\mu_h$) and $0.84 \times 10^{-6}$ cm$^2$V$^{-1}$s$^{-1}$ ($\mu_e$). The low PCE and mobilities were mainly due to poor film morphology with incontinuous network of the blend films. The amorphous property and low carrier mobility of PEBDT could relate to its disordered sidechain packing, so increasing the planarity and rigidity of the backbone maybe beneficial to achieve a more ordered

molecule packing and enhanced charge carrier mobility. Further optimized will focus on novel polymer structures by replacing TVT unit with fused ring on the backbone.

For the TO based polymers, our group has reported two TO polymers based on BDT and PT, respectively. To further improve the crystallinity of those polymers, two novel polymers based on BDT-terthiophene backbone with alkyloxime side chains substituted on spacing thiophenes were designed by taking the advantages of previous polymers' structures. The novel polymers P3TOBDT and P4TOBDT both demonstrated wide optical bandgaps and low-lying HOMO energy levels, which can obtain the complementary light absorption spectra and large Voc when blending with acceptor Y6. P3TOBDT neat film achieved a face-on orientation tendency with higher crystallinity than P4TOBDT after thermal annealing, which also exhibited higher SCLC hole mobility. The highest PCE up to 10.17% was achieved based on P4TOBDT:Y6 bland film, which was mostly contributed to high Jsc of 25.95 mA/cm$^2$, indicating the TO unit is a promising acceptor unit on donor polymers. The P3TOBDT:Y6 system exhibited lower PCE and carrier mobilities than P4TOBDT:Y6 indicating the poor phase separation in blend film, which may be due to high miscibility of materials in processing solvent chlorobenzene. However, both systems showed extremely low electron mobilities, resulting from poor interconnecting network of Y6. Thus, there are still large spaces for optimizing the OSC devices, and the improvement of film morphology will be focused in the future direction.

# Acknowledgements

# Table of Contents

# List of Figures

# List of Tables

# List of Abbreviations and Symbols

AFM          Atomic Force Microscopy

BDT          Benzodithiophene

BT          Bithiophene

CV          Cyclic Voltammetry

D-A          Donor-Acceptor

DSC          Differential Scanning Calorimetry

$E_g^{opt}$          Optical Energy Bandgap

$E_{loss}$          Energy Loss

FF          Fill Factor

GPC          Gel Permeation Chromatography

HOMO          Highest Occupied Molecular Orbital

HT-GPC          High-Temperature Gel Permeation Chromatography

$J_{SC}$          Short-Circuit Current

LUMO          Lowest Unoccupied Molecular Orbital

NMR          Nuclear Magnetic Resonance

OTFT          Organic Field Effect Transistor

OPV          Organic Photovoltaic

OSC          Organic Solar Cell

PCE          Power Conversion Efficiency

PT          Polythiophene

RMS          Root Mean Square

$R_s$          Series Resistance

$R_{sh}$          Shunt Resistance

| | |
|---|---|
| TGA | Thermogravimetric Analysis |
| UV-Vis | Ultraviolet-Visible |
| $V_{OC}$ | Open-Circuit Voltage |
| μ | Charge Carrier Mobility |
| XRD | X-ray Diffraction |

Other abbreviations and symbols are defined in the text.

# Chapter 1  Introduction

## 1.1 Overview of Organic Solar Cells

As the ongoing population growth and economy development, the limited natural resources such as fossil fuels can no longer meet world's demand. It is essential to develop the renewable resources and use them as priority power to ensure a sustainable future for human. Solar energy is one of the most promising renewable resources, which is clean and abundant. Nowadays, the commercial solar cells are made of inorganic semiconductors, from the first- and second-generation solar cells, such as crystalline silicon, copper indium gallium selenide (CIGS), and cadmium telluride (CdTe). [1] The third-generation solar cells are solar cells with latest technologies in research phase. Their core parts are made from inorganic nanoparticles and organic macromolecules, which are solution processable, for fabricating cheap and flexible photovoltaic devices in the future. [2] The organic solar cells (OSCs), an important and representative branch of the third-generation solar cell, have been studied extensively in lab and industry today, as a promising future energy resource.[2]

The silicon solar cell, which dominate the photovoltaic cell market nowadays. The atoms of silicon pack in an ordered structure as hard crystals, shown in **Figure 1-1**.[3] This crystal structure of silicon leads to inflexible and brittle properties of solar cell, which need to input much energy to obtain the super-thin film silicon.[3] Comparing with the inorganic semiconductor silicon, the organic semiconductors have a disordered atomic structure, as shown in **Figure 1-1**, which will reduce the fabricating difficulty and cost. Besides, the solar cells based on organic semiconductors with amorphous structure can not only lower the manufacturing cost, but also has broader application fields than the silicon solar cells. The organic semiconductor is carbon-based compounds, which is light and flexible. It can be easily printed on materials with cambered surface, such as walls, curtains, wearable devices, and car roofs, using roll-to-roll printing technology. [3]
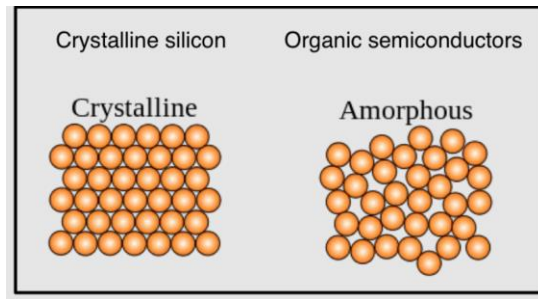
**Figure 1-1** Atomic structure of silicon and organic materials [3]

Although organic semiconductors have many unique properties and broad application prospects, there are still series of challenges related to the commercialization of organic solar cells (OSCs). One of the most important issue is the efficiency, which is much lower than that of silicon solar cell. As shown in **Figure 1-2**[4], a chart of the highest confirmed conversion efficiencies for research cells plotted by NREL, the single crystal silicon cells have achieved an efficiency of 27.6% in 2005, while the organic cell was developed around 2000 and it has reached an efficiency of 18.2% in 2020.[4]
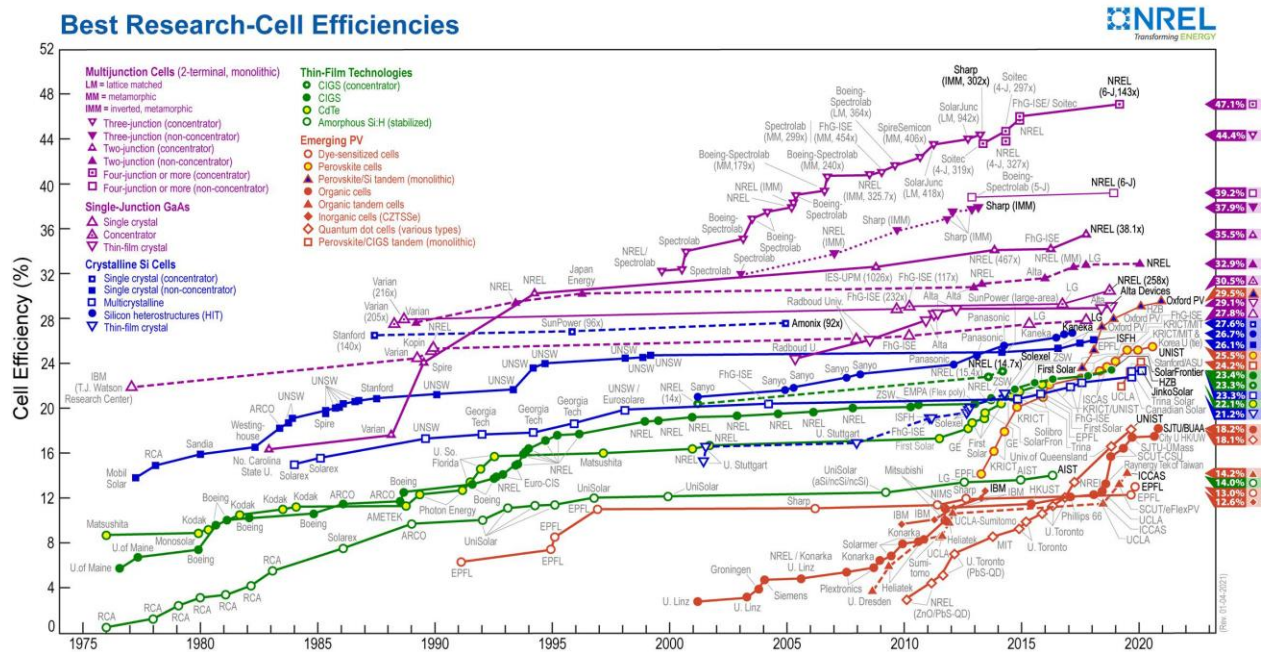


**Figure 1-2** Best research-cell efficiency chart [4]

In crystalline silicon (c-Si) solar cell, a p-n junction is formed by placing n-type and p-type silicon as sandwich structure to generate and transfer electricity.[2] Due to the Shockley-Queisser limit, the maximum efficiency of a single p-n junction solar cell is 33.7% with a bandgap of 1.34 eV under the typical sunlight conditions, which means the efficiency of a single junction c-Si solar cell cannot exceed this upper limit.[5] There are several methods to overcome the theoretical limit, one is using multijunction solar cells instead of single junction; the other is introducing different semiconductors as active layer, such as organic semiconductors. Despite organic solar cells do not have a theoretical efficiency limit, the highest efficiency reported is lower than 20%.[4] Regarding to the process of generating electricity, comparing with crystallin silicon solar cells, there are two main reasons for low efficiency: high binding energy and low carrier mobility.[2] The researches on OSCs nowadays are focusing on material development and structure design to overcome those weaknesses. The materials and structures of OSCs will be discussed in detail in the following sections. OSCs have a long way to go before they can complete with silicon-based solar cells.

## 1.2 Junction Types of Organic Solar Cells

The ideal structure of the photovoltaic layer consists of small donor and acceptor domains as interpenetrating network to enhance exciton dissociation but also large enough to promote carrier's mobility for reaching the electrodes.[6] Currently, the typical OSC devices adopt bulk heterojunction structure, which is a blend of electron donor and acceptor materials with phase separated in a few nanometers.[7] **Figure 1-3** shows the schematic of two common types of OSC structures, **(a)** bilayer and **(b)** bulk heterojunctions.

### 1.2.1 Single Layer

The earliest OSC structure is the simple layer with a film of organic semiconductor sandwiching between two electrodes. In 1981, Weinberger er al. used the conjugated polymer polyacetylene as the

active layer, with graphite and aluminum as electrodes, producing a photovoltaic device with internal energy conversion efficiency of 0.3%.[8] The single layer junction has low power conversion efficiencies due the difference of work function between two electrodes is not sufficient to separate excitons into electrons and holes, resulting in low exciton dissociation and high electron recombination rate.

**(a)**                                                **(b)**
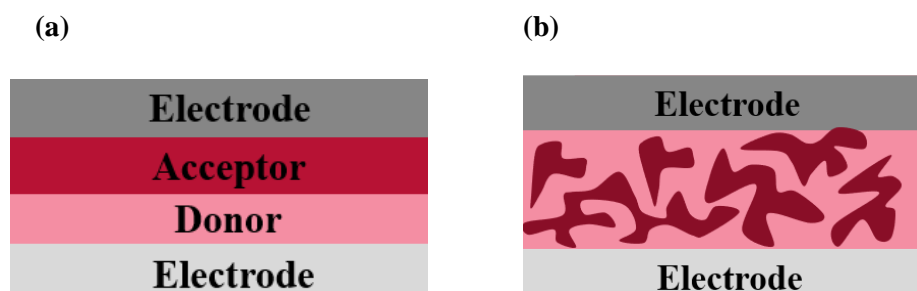


**Figure 1-3 (a)** Bilayer and **(b)** Bulk Heterojunction organic solar cell.

### 1.2.2 Bilayer

Bilayer junction structure consists of two layers between two electrodes, shown in **Figure 1-3 (a)**. The two materials in bilayer are chosen with different electron affinity and ionization energies, which enable the local electric field strong enough to split excitons and enhance the absorption range in the solar spectrum.[6] In 1986, the first bilayer organic photovoltaic cell was reported by Tang, using copper phthalocyanine (CuPc) as donor and a perylene tetracarboxylic derivative as acceptor, and a high FF of 0.65, a PCE about 1% has been achieved under AM2 illumination.[9] However, bilayer junction has a low charge separation efficiency due to the limiting small interfacial area between two active layers. Only the excitons close to the donor-acceptor interface have chances to separate, otherwise they will decay to ground state.[6] This drawback limits the thickness of the bilayers, resulting in the limitation of sufficient light absorption from thick films. Thus, the bilayer structure was further improved by mixing the donor and acceptor materials in a blend film to enlarge the interface between them, which is the bulk heterojunction.

### 1.2.3 Bulk Heterojunction (BHJ)

Bulk heterojunction was developed to overcome the issue in bilayer structure due to the limitation length of exciton diffusion. In BHJ, the donor and acceptor materials are intimately mixed in one layer, shown in **Figure 1-3 (b)**, which allow excitons to reach the donor-acceptor interface within a few nanometers.[6] The large interface area and small domains of donor and acceptor in BHJ not only increase the efficiency of exciton dissociation, but also relax the film thickness limitation for more light harvesting.[6] However, the phase separation and morphology are hard to control in the process of spin coating, and small domain size in blend film will decrease the order of molecular packing. When the charge carriers transfer in BHJ structure, the continuous pathway of both donor and acceptor materials are preferred, while the isolated domains may also exist causing bimolecular recombination.[6] Thus, for BHJ structure, balancing the film crystallinity and domain size of active layer is required to achieve high Jsc and FF.

## 1.3 Working Mechanism of Organic Solar Cells

The key concept behind the solar cell is photovoltaic effect. The photovoltaic processes of a typical OSC device can be schematically illustrated in four steps, shown in **Figure 1-4** [10]:

Step 1: Exciton is generated by absorbing photon. The photoactive layer (donor-acceptor composite) will absorb photons when the sun light illustrates on it, and the photons will give up its energy to the electrons to excited them and generate excitons in the donor and acceptor phase, which is electron-hole pairs.[3,7] The active layer can only absorb the photons with energy larger than the material bandgap (difference between HOMO and LUMO of the material), to obtain adequate energy for exciting electrons from ground state to excited state. After excitation, the electron-hole pair is localized at a single conjugated segment, which is due to low dielectric constant of organic semiconductors leading to strong electrostatic attraction, while inorganic semiconductors have a relatively high dielectric

constant, which can produce free charge carriers directly.[11] Furthermore, the Coulombic attraction of the electron-hole pair is called exciton binding energy ($E_B$), which is around 0.3-0.5 eV for organic materials.[6,11] While the binding energy is much smaller (around 0.01 eV) for inorganic semiconductors, resulting in easy separation of electron and hole under room temperature (thermal energy $k_BT \sim$ 0.025eV at room temperature).[6]

Step 2: The exciton diffuses towards the donor-acceptor interphase. The exciton undergo diffusion in the active layers within the length of 10-20 nm, and some of them can reach the interface of the donor and acceptor materials, otherwise the recombination occurs resulting in excitons back to ground state via radiative or nonradiative transition.[11] Thus, the D/A material separation phase length should be comparable with the exciton diffusion length to reach an efficient exciton dissociation process.[6]

Step 3: The exciton dissociates into hole and electron at the interphase by the electric field.[6] The electron and hole are separated at donor-acceptor interphase by the electric filed to overcome the binding energy, which require the $E_{LUMO}$ offset between D and A usually larger than 0.3eV.[11] The free electrons are produced in the LUMO of acceptor materials, and free holes are produced in the HOMO of the donor material.[6] Minimizing the binding energy is benefit for charge carrier generation, and photophysical studies show that more delocalized charge transfer pathway may decrease the binding energy, which was proofed by Lan et.al, they modulated the $E_b$ of linear D-A copolymers by adjusting the planarity and extending conjugation structure.[12]

Step 4: Each charge carrier (hole and electron) transports toward electrode, creating current and producing voltage. The electrons will drift along the acceptor to the cathode (Channel 1) while the holes will drift along the donor to the anode (Channel 2) as shown in **Figure 1-4**. [6, 10]
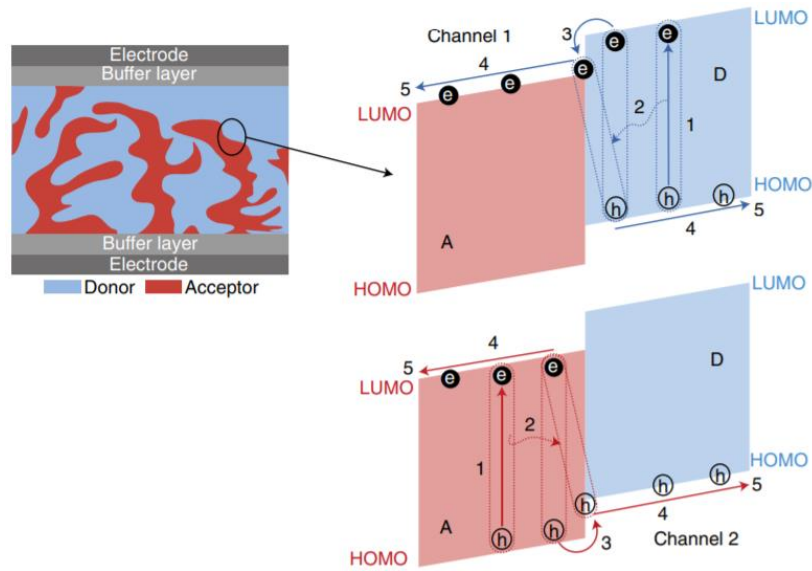
**Figure 1-4**  Working mechanism of OSCs 1. exciton generation; 2. exciton diffusion; 3. exciton dissociation; 4. charge carriers transfer; 5. charge carriers transport to electrodes.[10]

Power conversion efficiency (PCE) is the ultimate photovoltaic parameter to evaluate OSCs, which is characterized through current-voltage analysis. From the **Eq. 1-1** below,

$$PCE = \frac{J_{SC} \times V_{OC} \times FF}{P_{in}} \qquad \textbf{1-1}$$

PCE is proportional to the short-circuit current density (Jsc), open-circuit voltage (Voc), and fill factor (FF) of the OSC devices, which is closely related to the efficiencies of the four steps above. $P_{in}$ is the input power density of light source, which is AM 1.5G 100 mW/cm$^2$. [7]
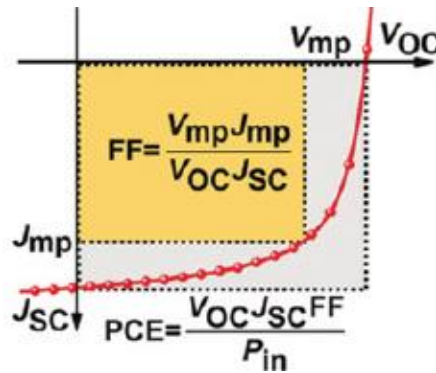


**Figure 1-5**  J-V curve and equations [7]

A J-V curve diagram and calculating equations of FF and PCE for an OSC device are shown in **Figure 1-5**. The short-circuit current density (Jsc, mA/cm$^2$) reflects the number of charges go through the solar cell per unit time per area, which is also the highest value of current density the OSC can achieve.[6] For the OSCs, there are several main factors affect Jsc: light harvesting by active layer, film thickness and morphology, and charge generation efficiency. Although, the absorption coefficient of the organic semiconductor film is high (around 10$^5$ cm$^{-1}$), the absorption tends to happen in narrow bandgaps. To match with the donor material, whose absorption peak is around 600nm, a narrow bandgap acceptor with absorption at long wavelength is desirable to achieve a complementary absorption ranges from infrared to ultraviolet of the donor-acceptor blend film, which can promote sun light harvesting and exciton generation.[6]

The open-circuit voltage (Voc) is the amount of forward bias on the solar cell, which is the maximum voltage available from an OSC.[13] In a donor-acceptor BHJ organic solar cell, the Voc is dependent on the offset between the $E_{HOMO}$ of donor material and $E_{LUMO}$ of acceptor material, which is shown in the **Eq. 1-2**,

$$V_{OC} = \frac{1}{e} (E_{ALUMO} - E_{DHOMO}) - E_{loss} \qquad \textbf{1-2}$$

where $E_{loss}$ is ~0.3V as an empirical value of energy loss in Shockley-Queisser framework, due to the recombination occurred when charge transfer in disordered D-A phases.[13] Thus, according to **Eq. 1-2**, one strategy to enhance Voc is increasing the energy level offset, another is decreasing the energy loss. By rising the percentage of electron withdrawing building blocks in D-A copolymer, the $E_{HOMO}$ of donor material can be effectively lowered and the energy level offset between donor and acceptor will be increased.[7] However, tunning the energy bandgap of donor or acceptor also results in increasing the electron excitation energy and decreasing the driving force for hole/electron transfer in the D-A interphase, both of which will reduce the Jsc in the solar cell devices, as shown in **Figure 1-6**.[6]
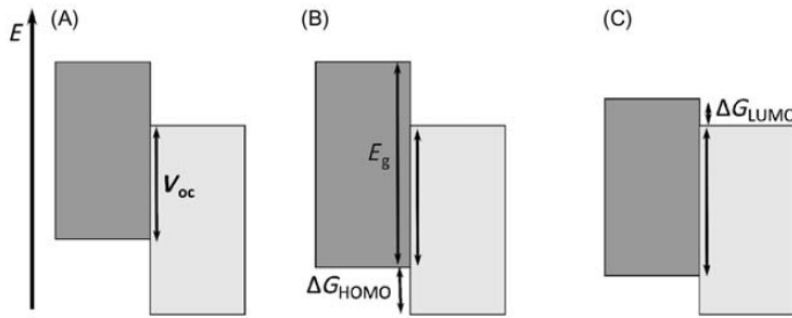
**Figure 1-6** Strategy to increase open-circuit voltage by tunning energy bandgap (A) energy offset between donor and acceptor; (B) lowering the $E_{HOMO}$ of donor will reduce the driving force of hole transfer; (C) rising the $E_{LUMO}$ of acceptor will reduce the driving force of electron transfer.[6]

The fill factor (FF) is the ratio of the maximum power ($V_{mp} \times J_{mp}$) obtained to the product of Voc and Jsc, as shown in **Figure 1-5**, it is the area ratio of yellow rectangle in gray rectangle, characterizing how "square" the J-V curve is.[14] An equivalent circuit model is introduced to characterize the solar cell performance: the BHJ is simulated as a diode, and the current loss is modeled by series resistance ($R_s$) and shunt resistance ($R_{sh}$), as shown in **Figure 1-7**.[14] Generally, series resistance consists of bulk resistance of layers, electrodes, and contact resistance of every interface. Shunt resistance is derived from current leakage by pinhole or edge of the cell.[14]
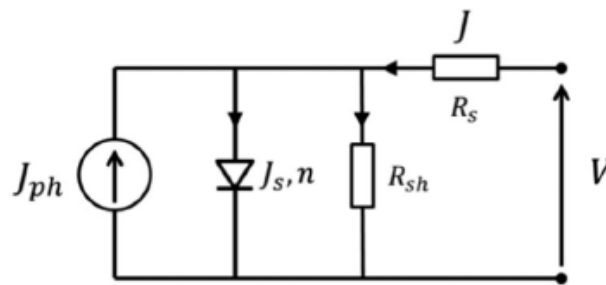


**Figure 1-7** Equivalent circuit of solar cells; $J_{ph}$: photo-generated current density, Js: reverse saturation current density of diode, J: recorded current density flow in external load.[14]

From the equivalent circuit, a large Rs can divide the applied voltage from the diode, then the diode has less voltage drop, which leads to slower increase of current with voltage in diode; a small Rsh can divide the current from diode, then the current under reverse bias will flow into Rsh, which results in a sharp increase of J with the reverse voltage increasing. Both situations will lower FF of the organic solar cell.[14] Commonly, there are several methods to increase FF in the fabrication of OSC: choosing suitable buffer layer to minimize the contact resistance and current leakage, enhancing the crystallinity of active layer to improve morphology, and balancing the weight ratio of donor and acceptor based on carrier mobility.[14]

## 1.4 Materials in BHJ Organic Solar Cells

Conventional structure and inverted structure are two main configurations of BHJ solar cells, as shown in **Figure 1-8**.[15] Anode and cathode materials are chosen to form Ohmic contacts for transporting and collecting charge carriers efficiently, and the buffe layers are used to accomplish energy level matching.[16] Indium tin oxide (ITO) is a widely used transparent conducting oxides due to its good electrical conductivity and optical transparency.[17] It can be deposited as thin film on glass as the transparent bottom electrode in lab level small devices. It works as anode in conventional structure OSC and as cathode in inverted structure. The buffer layers under electrodes function as the hole transport layers (HTL) or electron transport layers (ETL) for increasing the one-way charge transport. In the conventional OSC, the polymer mixture PEDOT:PSS is used as hole transport layer (HTL), which is a polymer mixture of two ionomer used as a water dispersion of gelled particles.[18] In the inverted OSC, the inorganic p-type transition metal sulfides or metal oxides such as $MoO_3$ and $MoS_2$ are usually applied to HTL with high stability and transparency.[19] For the ETL materials which play an important role in extracting electrons and blocking holes in OSCs, the metal oxide ZnO and $SnO_2$ are frequently utilized in inverted OSCs, and a ~1nm thin film of LiF is widely used as cathode buffer layer

10

in conventional OSCs.[20, 21] The active layer is the core part in BHJ OSCs for light absorption and exciton generation, which contains a blend film of electron-rich material (donor) and electron-deficient material (acceptor) to form a nanoscale bicontinuous morphology as shown in **Figure 1-8**. Donor materials are π-conjugated polymers such as P3HT, and the acceptor material are small molecules, which can be divided into two categories: fullerene acceptors (FAs), and non-fullerene acceptors (NFAs).[22]
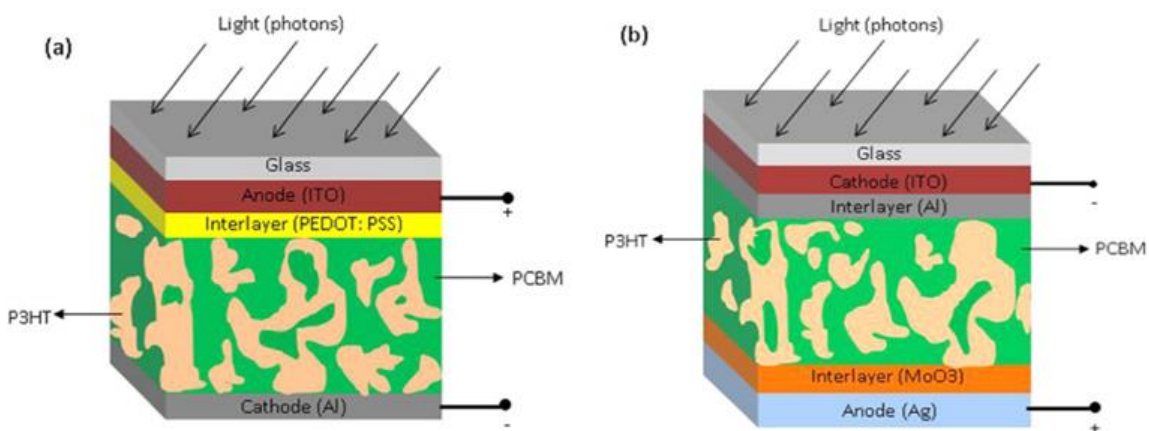


**Figure 1-8** Schematic structure of BHJ organic solar cells, (a) conventional structure and (b) inverted structure[15]

### 1.4.1 Fullerene and Non-fullerene Acceptors

In the past decades, the fullerene derivatives have been utilized as the electron acceptor universally in OSCs, due to their high electron affinity, high electron mobility and ease of polymer crosslinking properties.[22] The $C_{60}$ fullerene contains 12 pentagons and 20 hexagons with 30 double bonds and 30 single bonds. Since the pristine fullerene molecule $C_{60}$ exhibited poor solubility results in low performance in OSCs, a series of fullerene derivatives with high solubility were developed to obtain better device performance. $PC_{61}BM$ and $PC_{71}BM$ are two most wildly studied FAs, as shown in **Figure 1-9**.[23] $PC_{61}BM$ has a symmetrical structure with high aggregation property and poor absorption in the visible region while $PC_{71}BM$ is unsymmetrical with stronger absorption than the former. The single

11

junction BHJ-OSCs have been reported a high PCE ~10% based on PTB7-Th polymer and $PC_{71}BM$. The tandem OSCs have reached a PCE of 15% based on $PC_{61}BM$ and $PC_{71}BM$ as acceptor layers.[23]
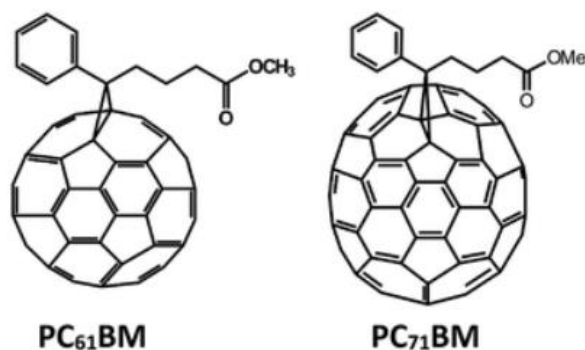


**Figure 1-9** Structures of fullerene derivatives $PC_{61}BM$ and $PC_{71}BM$ [24]

However, the fullerene acceptors have several limitations and disadvantages. The poor light harvesting property and energy levels cannot be tuned easily due to the poor synthetic flexibility of the symmetric structure. It is reported that they are sensitive to light and oxygen resulting in degradation performance of OSCs.[22] These constraints worked as motivators for community to look for new acceptor materials in order to commercialize the OSCs. Recently, non-fullerene acceptors (NFAs) based on small molecules have come to the forefront of OSC research. The high synthetic flexibility of small molecule can flexibly adjust the light absorption properties and energy levels of the materials, resulting in a sharp risen of PCE from 4% to over 16% in the single-junction OSCs in the past five years.[22] Several representative NFAs were listed in **Figure 1-10**, which have been frequently used in high performance BHJ OSCs. The electron acceptor ITIC was developed by Lin's group in 2015, which has a A-D-A structure consisting of a bulky seven-ring fused core (indacenodithieno[3,2-b]thiophene, IT), and end-capped 2-(3-oxo-2,3-dihydroinden-1-ylidene)malononitrile (INCN) groups, with four 4-hexylphenyl groups substituted.[25] The broad absorption (500~800nm) and low-lying $E_{HOMO}$ of ITIC made it successfully matched with a variety of donor materials, resulting in PCE surpassing 13% in the BHJ OSCs.[26] Another non-fullerene n-type small molecule acceptor Y6 was developed by Yuan's group in

12

2019, which has a A-DA'D-A structure consisting of electron-deficient central fused ring (dithienothiophen[3.2-b]- pyrrolobenzothiadiazole) with benzothiadiazole (BT).[27,28] The structure extended the absorption of Y6 to near infrared region, leading to a significant improving of Jsc of the OSCs, and the PCE of 15.7% was obtained in PM6:Y6 based device.[27] In this thesis, the NFA Y6 will be utilized as the acceptor in the OSCs, due to its matching energy level and complementary absorption range with the donor polymers.
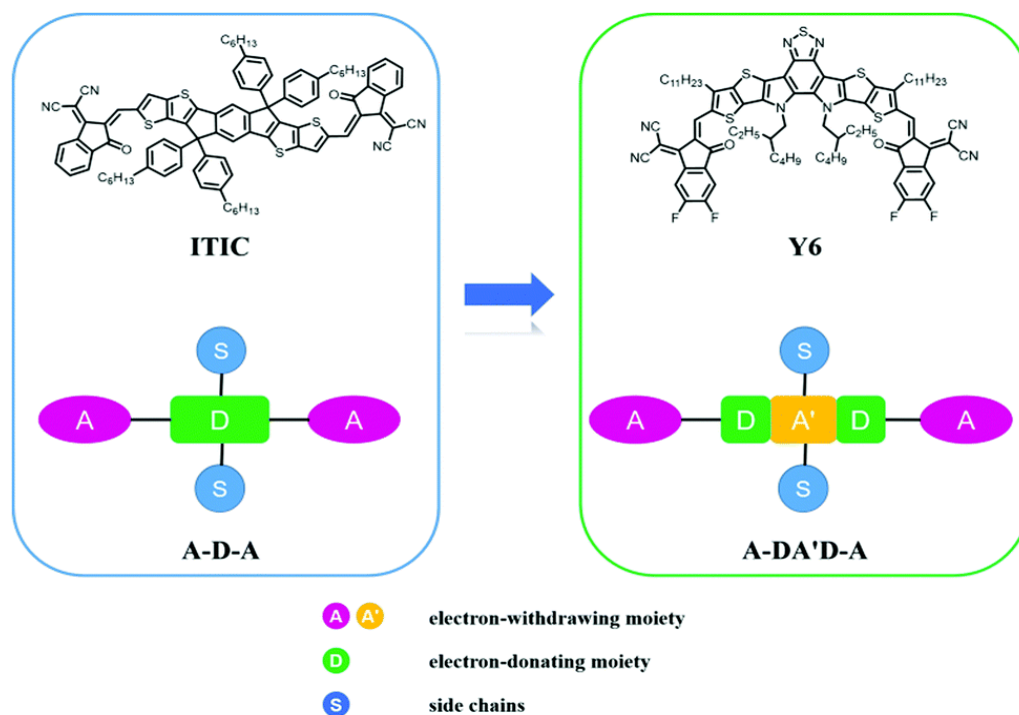


**Figure 1-10** Structures of non-fullerene acceptors ITIC and Y6 [28]

## 1.4.2 Wide-bandgap Polymer Donors

The selection of donor polymers to appropriately match with acceptors has a significant impact on the organic solar cell performance. According to their optical bandgap ($E_g^{opt}$), donor polymers are categorized into three groups: low-bandgap polymers ($E_g^{opt} < 1.6eV$), medium-bandgap polymers ($1.6eV < E_g^{opt} < 1.8eV$), and wide-bandgap polymers ($E_g^{opt} > 1.8eV$).[7] In the early stages of OSC applications, donor polymers with low-bandgap and medium-bandgap with broad absorption spectra

experienced great success, due to the fullerene acceptors have limited absorption range. However, as the rapid development of near-infrared NFAs, the wide-bandgap polymers can have a complementary light absorption range with the non-fullerene acceptors. By blending the wide-bandgap polymers and non-fullerene acceptors as active layers, the $V_{oc}$ of OSCs can be effectively increased due to the low-lying $E_{HOMO}$ of wide-bandgap polymers. Nowadays, the combination of NFAs with wide-bandgap polymers as active layers have been reported to produce the most efficient OSCs, suggesting that developing novel wide-bandgap donor polymers are of great importance for the OSC development.[7]

In the early stage, P3HT was the most representative polythiophene donor polymer with fully composed of thiophene unit backbone with alkyl substituted side chains. The PCE of 4.37% was obtained by P3HT:$PC_{61}$BM based OSCs.[29] However, the large bandgap and high HOMO level of P3HT leads to weak light harvesting and low Voc in the OSC devices. Thus, great efforts have been made to improve P3HT structure and develop novel polymer donor materials. The Donor-Acceptor copolymer structure was designed with the alternating electron-rich unit (D) and electron-withdrawing unit (A) which can effectively adjust the optoelectronic properties based on intramolecular push-pull electron effects.[30] The benzodithiophene (BDT) unit was firstly applied in donor polymer in OSCs by Hou's group in 2008, which has shown to be one of the most effective donor units in photovoltaic materials.[31] After that, BDT and polythiophene (PT) donor backbones were wildly applied in D-A copolymers. For the acceptor units in D:A copolymer, the building blocks frequently used are shown in **Figure 1-11 (a)**. Besides, side-chain engineering and halogenation method have also been applied to lower the energy levels of materials.[30] As shown in **Figure 1-11 (b)**, the fluorinated and ester substituted thiophenes are function as the "weak electron acceptor" units in the donor polymer. [32]

**(a)**
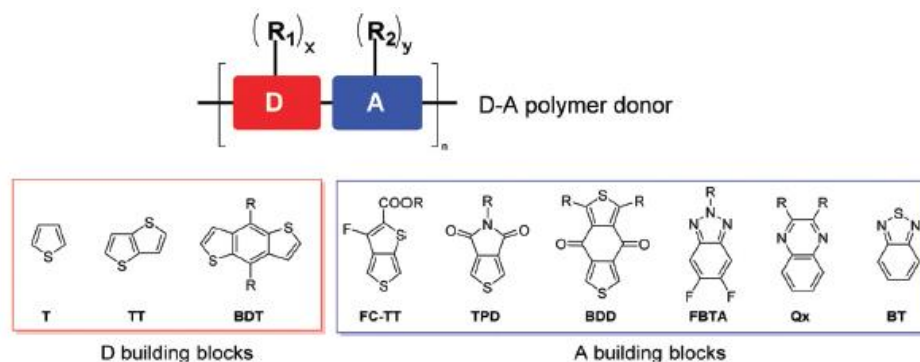
**(b)**
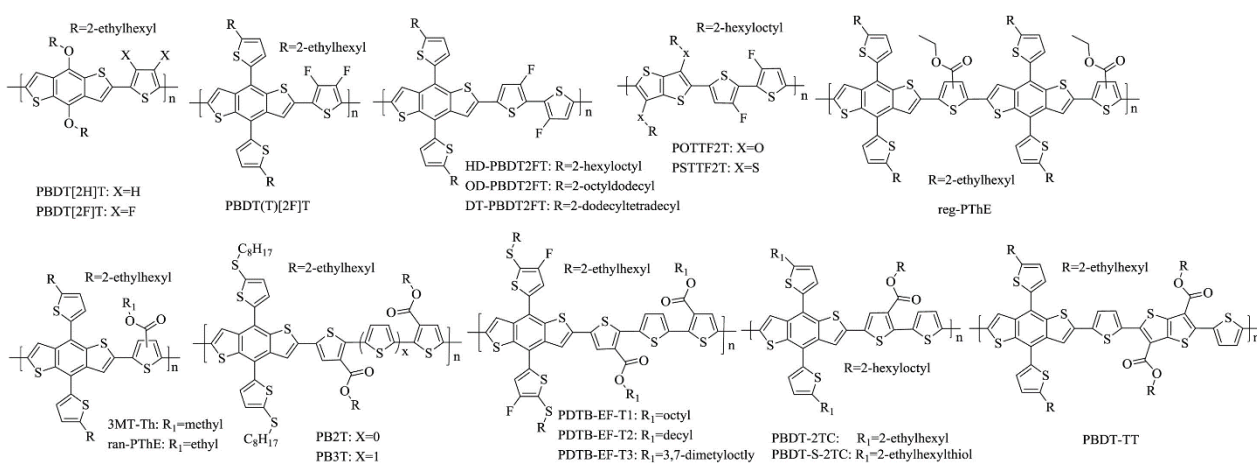
**Figure 1-11** (a) Schematic of D-A donor polymer, (b) wide-bandgap Donor polymer structures based on PT and BDT [7,32]

## 1.5 Characterization Methods of Polymers in Organic Solar Cells

Nuclear magnetic resonance (NMR) is a technique measuring the interaction of nuclear spins in strong magnetic field to determine the molecular structure of chemical materials.[33] The hydrogen nucleus $^1$H or carbon nucleus $^{13}$C possess magnetic moment will generate specific resonance frequency for different chemical environment under external magnetic field, which is recorded as chemical shift ($\delta$).[33] From the NMR figure, the composition of atomic groups and ratios can be obtained from the chemical shift and signal intensity.[33]

15

Gel permeation chromatography (GPC) is a type of size exclusion chromatography, which is a technique for investigating molecular weight distribution and dispersity of the polymers.[34] The porous beads in column is employed as stationary phase with flowing liquid as mobile phase. The separation of analytes is based on their volume, where small analytes spend more time going through the pores while the big analytes elute quickly and come out first. The molecular weight distribution with several important parameters of the polymer can be obtained after measurement, including number average molecular weight (Mn), weight average molecular weight (Mw), size average molecular weight (Mz), and dispersity. The polydispersity index (PDI) is the measurement of the heterogeneity of size of a polymer, which is calculated by **Eq. 1-3** [35]:

$$PDI = M_w / M_n \qquad\qquad \textbf{1-3}$$

Thermalgravimetric analysis (TGA) and differential scanning calorimetry (DSC) are typical techniques to characterize the thermal properties of the polymer. TGA is used to quantify the weight changes of polymers as a function of time and temperature.[36] Decomposition, oxidation, and physical processes including sublimation, evaporation, and desorption, can induce polymer weight changes.[36] A thermally stable polymer should be able to maintain their quality with little weight loss under a certain temperature range. DSC is a technique used to investigate the response of polymers to heating, by monitor the heat flow between sample and the reference. The temperature of polymer thermal transition such as glass transition ($T_g$), crystallization ($T_c$), and melting ($T_m$) can be identified from the shape of peaks in heat flow-temperature curve.[37]

Ultraviolet-visible spectroscopy (UV-vis) refers to absorption spectroscopy in the wavelength range of 200nm~1000nm as partial ultraviolet and full visible region. It measures the amount of UV-vis light transmitting the sample and calculates the absorbance using equation A= -log (T).[38] UV-vis can be utilized for qualitative manner, such as identifying functional groups or compounds, and also in a

quantitative manner, such as absorption coefficient.[39] For the donor polymer, the absorption of light

energy excites the electrons from ground state to the first singlet excited state of the molecules, which

can be used to estimate the energy levels of the materials.[38] According to the edge onset wavelength

($\lambda_{onset}$) from the spectra, the optical bandgap ($E_g^{opt}$) of the sample can be calculated from **Eq. 1-4** [38]:

$$E_g(eV) = h \times f = h \times \frac{c}{\lambda_{onset}} \approx \frac{1240}{\lambda_{onset}(nm)} \qquad \textbf{1-4}$$

Cyclic voltammetry (CV) is an electrochemical technique used to measure the current versus the

applied voltage of a redox active solution or the material on the electrode, where a cycle is formed as

the voltage switches back and forth.[40] The In organic semiconductors, the $E_{HOMO}$ is the energy necessary

to extract an electron from the molecule, which is the oxidation process, and the $E_{LUMO}$ is the energy

for injecting an electron into the molecule, which is the reduction process. By measuring the redox

potentials of the sample, the energy diagram can be estimated using the **Eq. 1-5** [40], where Ferrocene is

used as a reference $E_{HOMO}$= -4.8eV:

$$E_{HOMO}(eV) = -e\ (E_{ox}^{onset}) - 4.8\ eV$$

$$E_{LUMO}(eV) = -e\ (E_{red}^{onset}) - 4.8\ eV \qquad \textbf{1-5}$$

Photoluminescence (PL) is a spectroscopy used to measure the intensity of fluorescence of the material

which is excited by a specific wavelength. As shown in the **Figure 1-12**, comparing with the absorption,

the fluorescence is red shifted, which is called the Stokes shift. This is due to the vibrational relaxation

processes (energy loss) occurring before the fluorescence emission.[41] For the D-A blend film in OSCs,

the excitons will experience a non-radiative transition as a result of exciton dissociation occurring in

the D-A interphase, where the efficiency is called photoluminescence quenching efficiency (PLQE)

and calculated by **Eq. 1-6**, where $PL_{blend}$ is the PL intensity (counts) of D-A blend films and $PL_{neat}$ is

the PL intensity (counts) of neat films:

$$PLQE = 1 - \frac{PL_{blend}}{PL_{neat}} \qquad\qquad \textbf{1-6}$$
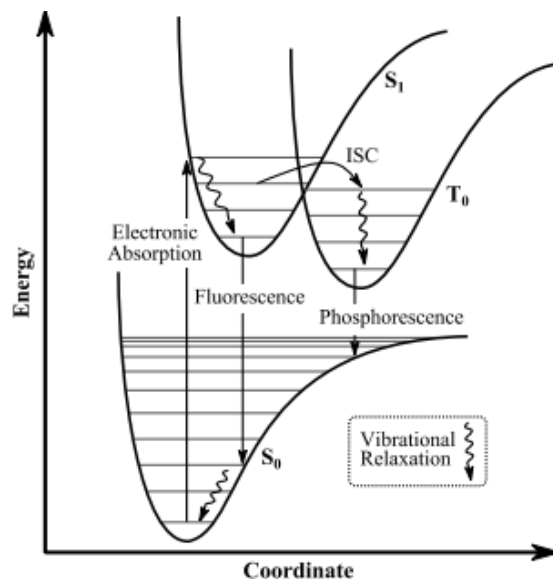


**Figure 1-12** Frank-Condon energy level diagram. $S_0$: singlet ground state, $S_1$: first singlet excited

state, $T_0$: triplet state.[41]

X-ray diffraction (XRD) is a typical technique for investigating the crystal structure of the materials.

The monochromatic beam is produced as incident rays, and it can form constructive interference after

scattering at specific angles from each set of lattice planes, which are recorded as XRD peaks.[42] The

constructive interference obey the Bragg's law **Eq. 1-7**, where $\lambda$ is the wavelength of X-ray beam, d is

the distance of lattice planes, $\theta$ is the incident angle of beam:

$$n\lambda = 2d sin\theta \qquad\qquad \textbf{1-7}$$

Atomic force microscopy (AFM) is a kind of scanning probe microscopy with high resolution in

nanometer which could detect non-conductive specimen surface and working in air or liquid media.[43]

The basic components are a cantilever with probe tip, a laser diode, mirrors, a position sensitive

photodetector, and controlling system. The AFM working schematic is shown in **Figure 1-13**. It utilizes

the cantilever which contains a sharp probe tip to scan the specified area of the sample. Meanwhile, the

18

laser diode sends photon beam to the cantilever, and mirrors reflect the beam to the position sensitive photodetector, which can monitor the cantilever's location. The controlling system records the height changes of the probe and computer draws the picture of the sample surface afterwards.[43]
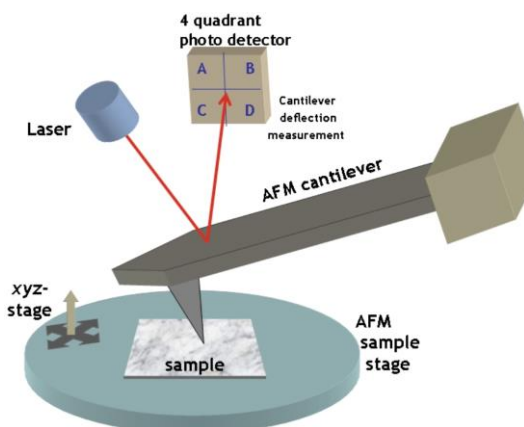


**Figure 1-13** The Schematic components of AFM with optical beam deflection system[44]

## 1.6 Objective and Structure of This Thesis

In the past years, non-fullerene small molecule acceptors (NF-SMAs) have made significant advancements, resulting in a steady rise in the PCE of non-fullerene organic solar cells. To obtain greater compatibility with the non-fullerene small molecule acceptors, the trend of molecular design of the donor polymers is toward wide bandgap, adjusted characteristics and preferably ecologic processing for OSCs fabrication.[7] The most widely studied donor polymer is poly(3-hexylthiophene) (P3HT), which is a representative organic semiconducting polymer with low cost and high hole mobility. However, the high lying $E_{HOMO}$ (-5.1eV) of P3HT limits the Voc performance of organic solar cells.[7] To solve this issue, new donor polymers with lower lying $E_{HOMO}$ have been extensively designed and investigated.

In Chapter 2, a low-cost ester-substituted vinyl (TVT-ester) unit is invented as the weak acceptor unit in donor polymer backbone, and three donor polymers based on TVT-ester are designed and

synthesized : PZBT, PZBDT, and PEBDT. The thermal, optical, and electrochemical properties of those polymers will be characterized utilizing TGA, GPC, UV-vis, and CV measurement. Among three TVT-ester based polymers, PEBDT is attempted to show a planar backbone structure due to DFT simulation. The PEBDT will be used as donor material in inverted OSCs to study its photovoltaic properties, blending with two different acceptor materials respectively: $(3PS)_2$-SiPc and Y6, as they each has their own merits for OSCs. The charge mobilities and film morphology of PEBDT: Acceptor blend films will be further investigated through SCLC, XRD and AFM techniques.

In Chapter 3, the objective of the work is to take advantage of the promising electron-withdrawing group alkyl-oxime to design and investigate new donor polymers with low-lying energy levels. As a further development of our previously reported alky-oxime based polymers, two novel donor polymers P3NOBDT and P4NOBDT will be discussed and characterized through technologies. Then two polymers are used as donor materials blending with acceptor Y6 to fabricate the inverted OSCs. Several optimizations on thickness, solvent, and ratio will be carried out to investigate the photovoltaic properties of the polymers.

Finally, in Chapter 4, the research works in this thesis will be summarized along with some future directions for improving the photovoltaic properties of the donor polymers designed in this thesis.

# Chapter 2 Synthesis and Characterization of TVT-ester Based Donor Polymers

## 2.1 Introduction

In the early stage of donor polymer research, the polythiophenes (PTs), such as P3HT, exhibits a high lying $E_{HOMO}$ which inhibits the performance of OSCs. In order to tune the energy levels of donor polymers, the donor-acceptor (D-A) copolymer structure has received much interest nowadays. The structure is based on alternating electron donating (D) and weak electron withdrawing (A) building blocks, which is very convenient to tune the energy levels and optical bandgap of the materials.[7] Thiophene (T) and benzo[1,2-b:4,5-b0]dithiophene (BDT) are mostly used electron donating building blocks in wide-bandgap polymer design, with good backbone coplanarity and chemical stability.[7] Carboxylic ester sidechain (COOR), a weak acceptor unit, has attracted much attention to be applied onto D-A polymers and afford a series of carboxylate-thiophene derivative polymers. Hou's group inserted ester-substituted thiophene into the thiophene backbone polymer, resulting in a lower $E_{HOMO}$ (-5.26eV) than P3HT (-5.1eV) and a high PCE of 7.2%.[45] After that, Choi's group introduced ester-substituted thiophene into BDT-based polymer, resulting in a much lower $E_{HOMO}$ (-5.43 eV) and a higher PCE of 9.73%.[46] Furthermore, Hou and coworkers reported a series of low-cost copolymers based on poly(thiophene-vinylene)s (PTVs) with ester-substituted thiophene, and they found that from the theoretical calculation, the ester-based side chain is more thermal stable than the alkyl side chain, and ester-substituted PTVs are more likely to develop a planar structure than alkyl-substituted ones.[47] Besides, Liu et al. pointed out with the replacement of thiophene backbone with thiophene-vinyl backbone, the PTVs showed broader absorption spectra, higher carrier mobilities, and better film morphologies comparing to single thiophene-based polymers (PTs).[47,48]

To take advantage of the positive effects of both ester-based side chain and thiophene-vinyl backbone, a novel building block methyl 2,3-bis(5-bromothiophene-2-vinyl)acrylate (TVT-ester) was designed for wide bandgap copolymers, consisting of a thiophene-vinyl-thiophene (TVT) backbone with carboxylic ester substituting on vinyl directly, shown in **Figure 2-1 (E), (Z)**.
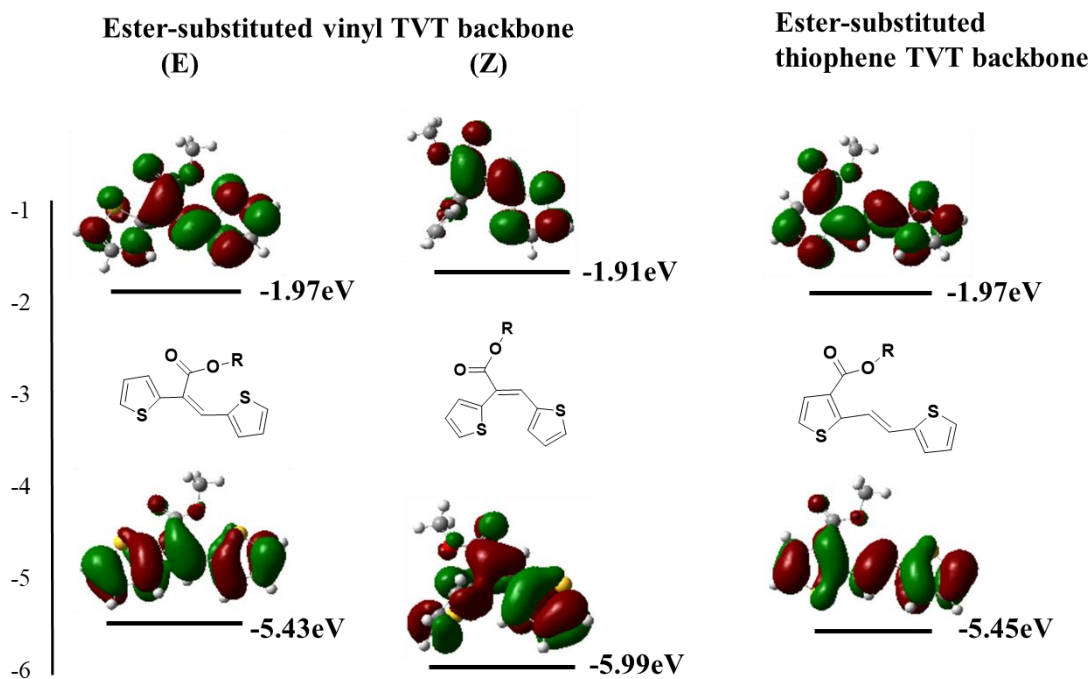


**Figure 2-1** Predicted energy levels of E-type, Z-type ester-substituted vinyl TVT unit, and ester-substituted thiophene TVT unit

In this chapter, the TVT-ester monomer was copolymerized with bithiophene (BT) or BDT to afford three D-A copolymers as donor materials in OSCs. In the early researches, the D-A copolymer designing strategy based on ester-substituted PTs or PTVs has been shown to be a successful method for achieving efficient photovoltaic performance,[48] but among those reported structures, the ester sidechains were all introduced onto the thiophene. This is the first time that an ester sidechain as a weak acceptor unit connects to the electron-rich skeleton directly, by substituting onto the vinyl group

between two thiophene. From the density functional theory (DFT) simulation, **Figure 2-1** (**E**) is E-type ester-substituted vinyl TVT backbone, which has a similar electron delocalized region for both $E_{HOMO}$ and $E_{LUMO}$ with the E-type ester-substituted thiophene TVT. **Figure 2-1** (**Z**) is Z-type ester-substituted vinyl TVT configuration, and its HOMO level is delocalized widely around ester-substituted vinyl and thiophene. The estimated low-lying and widely delocalized energy levels of TVT-COOR unit suggest that it is a potential candidate monomer for wide bandgap donor polymers.

## 2.2 Polymer Structure Design

Based on the TVT-ester unit structure, at the beginning, it was copolymerized with BT to afford a new donor polymer PZBT, which has four thiophene units with a long carbon chain connected to the vinyl backbone, as shown in **Figure 2-2**. Due to the steric hindrance between the long carbon chain and thiophene backbone, the E-type isomer cannot be formed through chemical reaction, thus, only Z-type polymer PZBT was obtained after polymerization. The polymer PZBT has poor film-forming property, which could be due to its heavily sidechain and high thiophene content in backbone structure design. The sidechain engineering plays a significant role on the chemical properties of a polymer, the length of carbon chain can modulate the solubility, planarity, and film crystallinity. Long carbon chain could interrupt π-π stacking between polymer backbones resulting in twisted polymer chain, amorphous film morphology and low carrier mobilities. Besides, the high thiophene concentration can also lead to high tendency for polymer aggregation and bad miscibility when blending with acceptor material.[49]

Consequently, in order to optimize the properties of polymer based on TVT- ester unit structure and avoid the defects of PZBT, two strategies were applied on polymer design: 1. Change the bithiophene (BT) unit to benzodithiophene (BDT), which has high planarity and proper energy levels resulting in faster charge transport; 2. Shorten the carboxylic ester sidechain for less effect on polymer conjugation and able to obtain E-type isomer. Thus, after obtaining the polymer PZBT, two novel isomer polymers

PEBDT and PZBDT were designed and synthesized, based on TVT- ester unit copolymerizing with BDT to overcome the defects of PZBT, as shown in **Figure 2-2**. Comparing with PZBT, these two polymers showed improved film-forming property, resulting from big and planar structure of BDT-T unit in the backbone.



**PZBT**　　　　　　　　　**PZBDT**　　　　　　　　　**PEBDT**
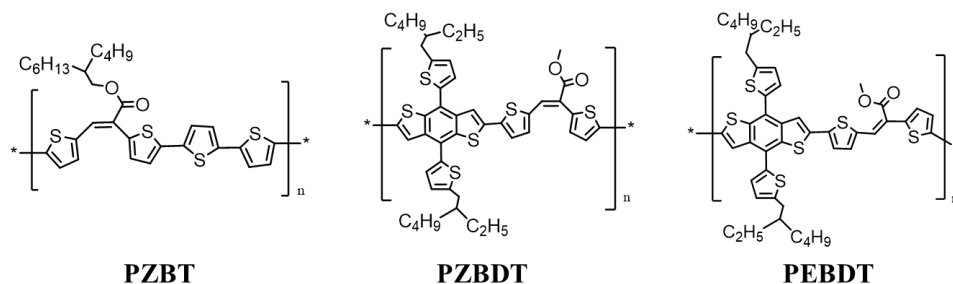
**Figure 2-2** Structure of polymers based on TVT- ester unit

### 2.2.1 Polymer Simulation by Density Functional Theory

Firstly, the density functional theory (DFT) was applied to simulate the polymers for estimating the optimized geometries and energy levels for one monomer unit, where the long alkyl-chains on BDT unit and TVT unit were replaced with methyl groups to reduce calculation time. The simulations were run under Gaussian 09 at B3LYP/6-31G(d) basis set. The optimized geometries with dihedral angle of the repeating unit of PZBT, PZBDT, and PEBDT are shown in the **Figure 2-3**. As mentioned before, the polymer PZBT has poor film-forming property and low molecular weight, due to its long alkyl sidechain and long thiophene backbone. The simulation result of the monomer unit ZBT showed large dihedral angle 61° between thiophenes, which leads to twisted backbone and bad film morphology, consisting with the defects of polymer PZBT. The LUMO levels of ZBT are only delocalized along half of the twisted backbone, indicating poor carrier transfer along the polymer. The optimized structure of ZBDT and EBDT have smaller dihedral angles than ZBT, illustrating the replacement of bithiophene with BDT unit on polymer backbone can lead to planar structure and efficient charge transfer. The

24

isomers ZBDT and EBDT showed similar charge distribution results, with most LUMO levels delocalizing around TVT- ester unit and partial on BDT, and HOMO levels delocalizing uniformly on BDT and TVT- ester. Both ZBDT and EBDT have same calculated $E_{LUMO}$= -2.21 eV. The ZBDT was simulated to achieve a low $E_{HOMO}$ of -5.06 eV, while large bandgap also indicated its poor planarity and bad molecular packing. The EBDT has a higher $E_{HOMO}$= -5.00 eV, resulting from small dihedral angle 36° and planar backbone, indicating good π-π staking of polymer.
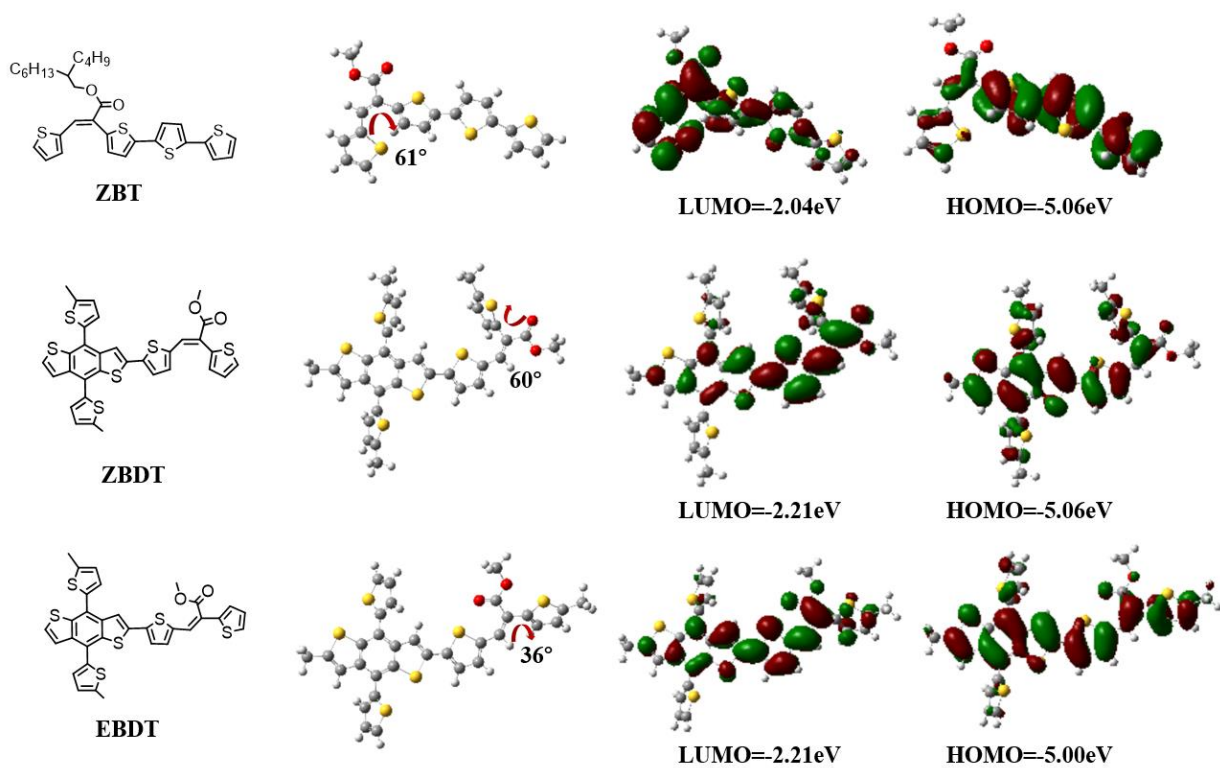


**Figure 2-3** Optimized geometries of the monomer unit of PZBT, PZBDT, and PEBDT, with estimated energy levels from DFT calculation.

### 2.2.2 Monomers and Polymers Synthesis

The polymers PZBT, PZBDT and PEBDT were synthesized by following the synthesis route shown in **Figure 2-4,** and the synthetic routes with NMR data of each step were listed in Chapter 2.6.3.

**3-Z**, **4-Z** and **4-E** are three acceptor units for polymer PZBT, PZBDT and PEBDT respectively. They were all alkylated from the two isomer **2-Z** and **2-E**. The Perkin Reaction method was applied to prepare the isomer compounds **2-Z** and **2-E** via the aldol condensation between 5-bromothiophene-2-carbaldehyde and 2-(5-bromothiophen-2-yl)acetic acid, with triethylamine as catalyst and acetic acid anhydride as solvent according to the literature.[50] The mixture of **2-Z/E** can be separated through precipitation by acidizing the aqueous solution from alkali to acid. The monomer **3-Z** was alkylated from **2-Z/E** for further copolymerizing with BT unit to obtain the polymer PZBT, with no **3-E** product existing due to the steric hindrance between the long carbon chain and the TVT backbone. Then the isomer mixture **2-Z/E** were further alkylated with one methyl group on the carboxyl group and produce the monomers **4-Z** and **4-E** for further copolymerizing with BDT unit to obtain the polymer PZBDT and PEBDT.

The three TVT- ester based polymers were synthesized via Stille coupling polymerization method with 1:1 ratio of an acceptor unit (**3-Z**, **4-Z**, or **4-E**) and a donor unit BT or BDT, utilizing $Pd_2(dba)_3$ as catalyst and $P(o\text{-tol})_3$ as the ligand with solvent chlorobenzene. After reacting overnight at 90 °C in argon atmosphere, the cooling down mixture was precipitated in methanol and it was further washed with acetone and hexane through Soxhlet extraction. Finally, the polymer was extracted by chloroform and obtained dark purple films after removing the solvent.[51] All the TVT- ester based polymers showed good solubility in chloroform at room temperature. The polymers PZBDT and PEBDT showed better film-forming property than PZBT, indicating the polymer conjugation and molecular weight were improved by replacing BT with BDT in material backbone.
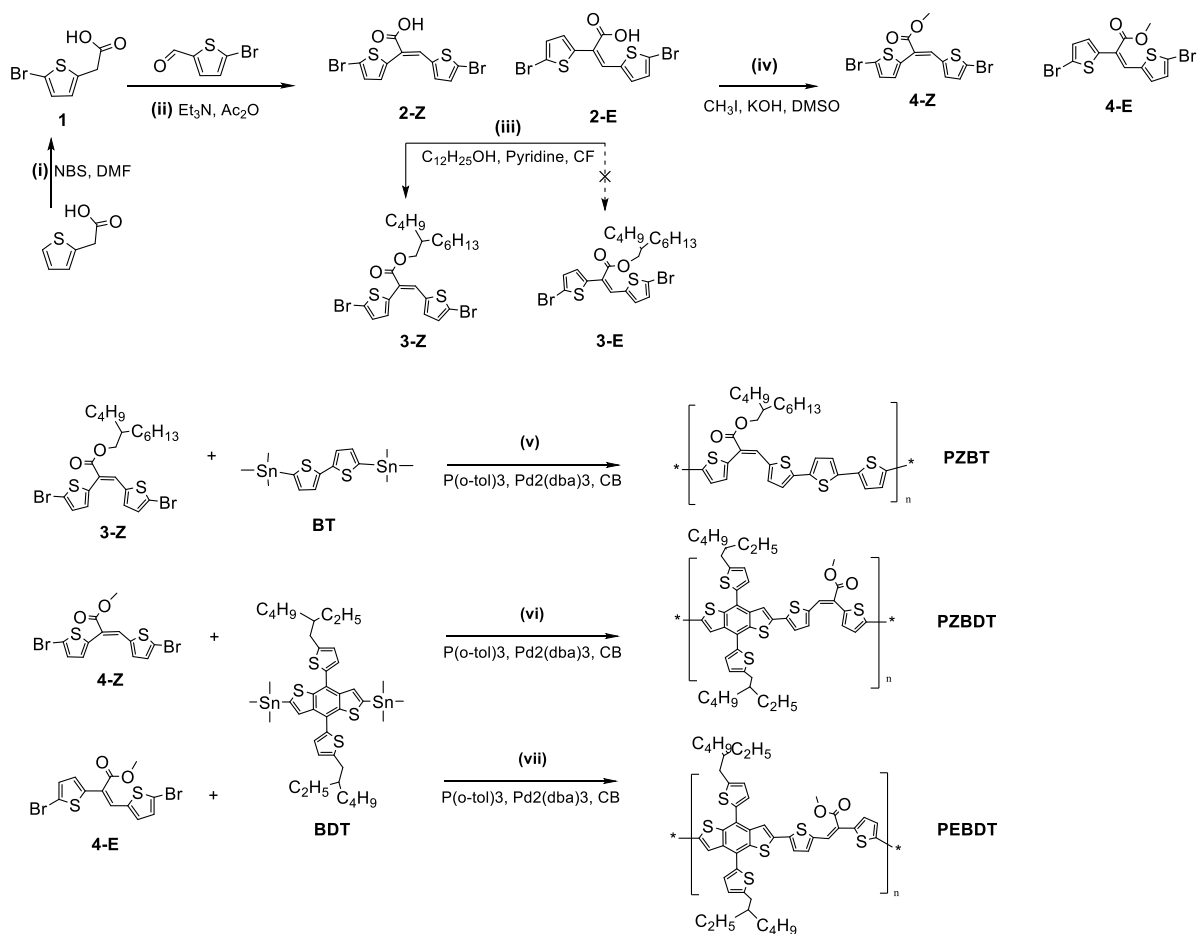
**Figure 2-4** Synthesis route of TVT- ester based monomers and polymers

## 2.3 Characterization of TVT-ester Polymers

### 2.3.1 Physical Properties (GPC,TGA, and DSC)

The molecular weight of the TVT-ester based polymers were measured by high-temperature gel permeation chromatography (HT-GPC) with 1,2,4-trichlorobenzene as eluent and polystyrene as standards at 150 °C. The number average molecular weight (Mn) of PZBT, PZBDT, and PEBDT were measured to be 12.6 kDa, 8.13 kDa, and 7.93 kDa. The polydispersity index (PDI) were determined to be 1.72, 1.88, and 1.88, respectively (**Figure 2-5**). Interestingly, although the replacement of BT with BDT improved film-forming property, the molecular weight of polymers were decreased.

27
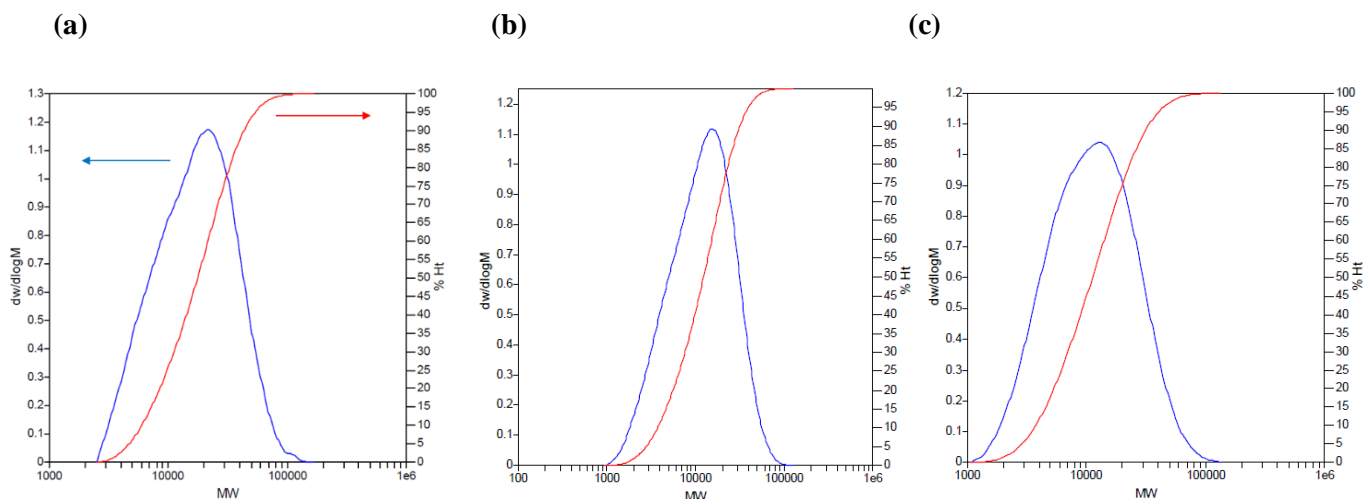
**Figure 2-5** HT-GPC molecular weight distribution of polymer **(a)** PZBT, **(b)** PZBDT, **(c)** PEBDT.

**Table 2-1** Molecular weight and thermal properties of three TVT-COOR based polymers

| Polymer | $M_n$ (kDa) | $M_w$ (kDa) | PDI | $T_d^{1st}$ (°C) | $T_g$ (°C) |
|---------|-------------|-------------|------|------------------|------------|
| PZBT    | 12.6        | 21.7        | 1.72 | 350              | 46         |
| PZBDT   | 8.13        | 15.3        | 1.88 | 380              | /          |
| PEBDT   | 7.93        | 14.9        | 1.88 | 372              | /          |

The thermal stability of three TVT- ester based polymers were investigated by thermalgravimetric analysis (TGA) and differential scanning calorimetry (DSC). As shown in the **Figure 2-6 (a)**, the polymers PZBT, PZBDT and PEBDT lost 1% weight at 246°C, 295°C and 282°C, respectively, and their first step decomposition occurred at 350°C, 380°C, and 372°C, respectively. The better thermal stability of PZBDT and PEBDT than PZBT makes them ideal for OSCs that require a high temperature tolerance. From the **Figure 2-6 (b)**, PZBT had a weak glass transition at 46°C and an exothermic transition at 135°C. No obvious glass transitions were observed of PZBDT and PEBDT, while weak

exothermic transitions were observed at 58°C and 77°C when cooling down for PZBDT and PEBDT, respectively, indicating that the TVT-ester based polymers lacks crystalline domain. The molecular weight and thermal properties for polymers were summarized in **Table 2-1**.

**(a)**



**(b)**
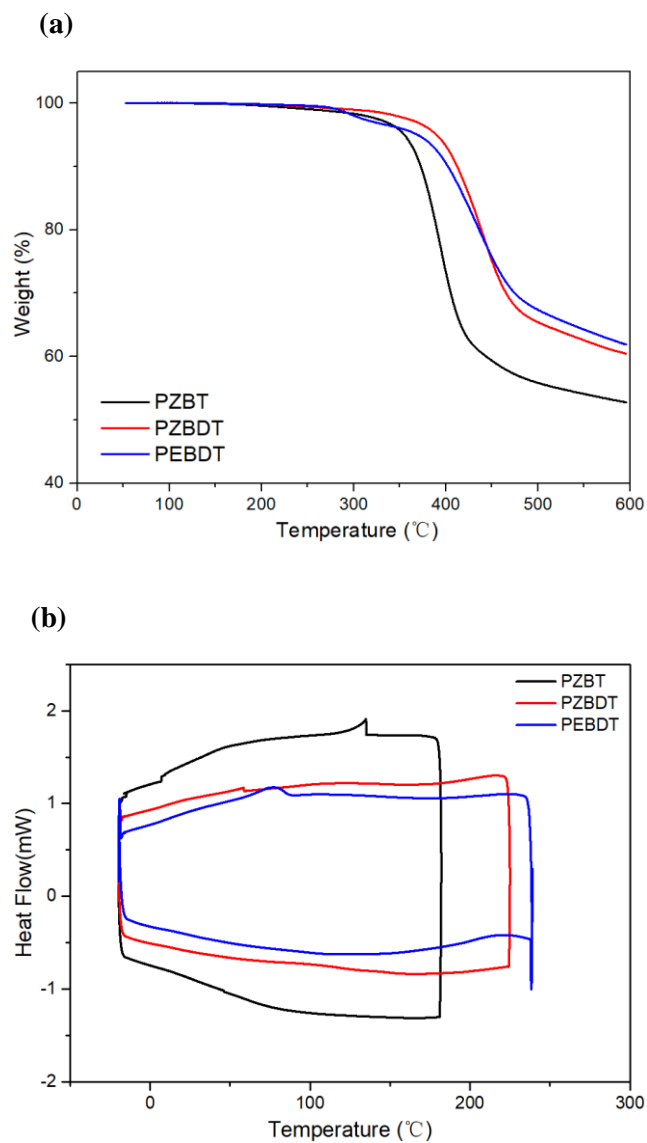


**Figure 2-6** **(a)** TGA curves and **(b)** DSC curves for PZBT, PZBDT, and PEBDT.

**2.3.2 Optical and Electrochemical Properties (UV-Vis, CV, and PL)**

The UV-vis absorption spectra of three TVT- ester based polymers were measured in both solution and thin films, shown in **Figure 2-7 (b, c, d)**. The polymer thin films were fabricated via spin-coating the 5mg/ml solution in chloroform on glass wafers. The optical properties of thin films were investigated under both room temperature and annealing of 100°C. The cyclic voltammetry (CV) was employed to study the electrochemical properties of three TVT-ester based polymers, with the polymer film on a platinum working electrode in 0.1M [n-Bu$_4$N]$^+$[PF6]$^-$ in acetonitrile solution at a scan rate of 0.1V/s,[52] shown in **Figure 2-7 (a)**. The summary of the polymer electrooptical properties are shown in **Table 2-2**.

For the Z-isomer based donor polymer PZBT and PZBDT, they showed a coincident absorption shape in the wavelength range from 450nm to 800nm, which results in similar wavelength onset and optical bandgap. PZBDT has an additional peak at 350nm, which relates to the BDT unit in the backbone structure. For the BDT based donor polymer PZBDT and PEBDT, both showed obvious red shift $\lambda_{max}$ from solution state to thin film state, and an inconspicuous shoulder peak for PZBDT around 530nm, and PEBDT around 630nm of the thin film state at room temperature, due to molecular aggregation and π-π stacking of polymer chains. Besides, both had an additional 4nm red shift $\lambda_{max}$ after annealing at 100 oC for 30 min, indicating a more ordered molecular packing. The polymer optical bandgap (Egopt) calculated from the absorption onsets of as-cast thin film state are 1.83 eV and 2.03 eV for PEBDT and PZBDT, respectively, which are consistent with the DFT simulation result that PEBDT maintained a smaller bandgap than PZBDT due to planar backbone.

The $E_{HOMO}$ of three polymers were determined by cyclic voltammetry (CV), corresponding to the onset oxidation potential with respect to ferrocene/ferrocenium (Fc/Fc$^+$).[52] The $E_{LUMO}$ was estimated by adding $E_g^{opt}$ and $E_{HOMO}$ together, since no reduction peak can be observed on CV for the three donor polymers. Comparing to the polymer PTVT-C12 developed by Hou's group, with $E_{HOMO}$=-5.31 eV and $E_{LUMO}$=-3.10 eV, containing TVT backbone with ester side chain substituted on thiophene [47], our polymer PZBT were demonstrated lower HOMO energy levels by moving ester sidechain onto vinyl. It is worth noting that PZBDT showed 0.09 eV lower $E_{HOMO}$ than PZBT, revealing the replacement of BT with BDT can effectively enhance push-pull effect in D-A copolymer structure to downshift the HOMO energy level. The $E_{LUMO}$ of PZBDT and PEBDT are similar and PZBDT had a 0.17 eV lower $E_{HOMO}$ due to its larger energy bandgap caused by poor backbone planarity. The wide bandgaps and low-lying $E_{HOMO}$ of two TVT-ester based polymers, PZBDT and PEBDT, might be promising candidates as donor materials for non-fullerene OSCs, notably the PEBDT, which holds a more planar backbone and broader absorption range than the isomer PZBDT, might give a better molecular packing and film morphology in OSC devices.

**(a)**



**(b)**



**(c)**



**(d)**
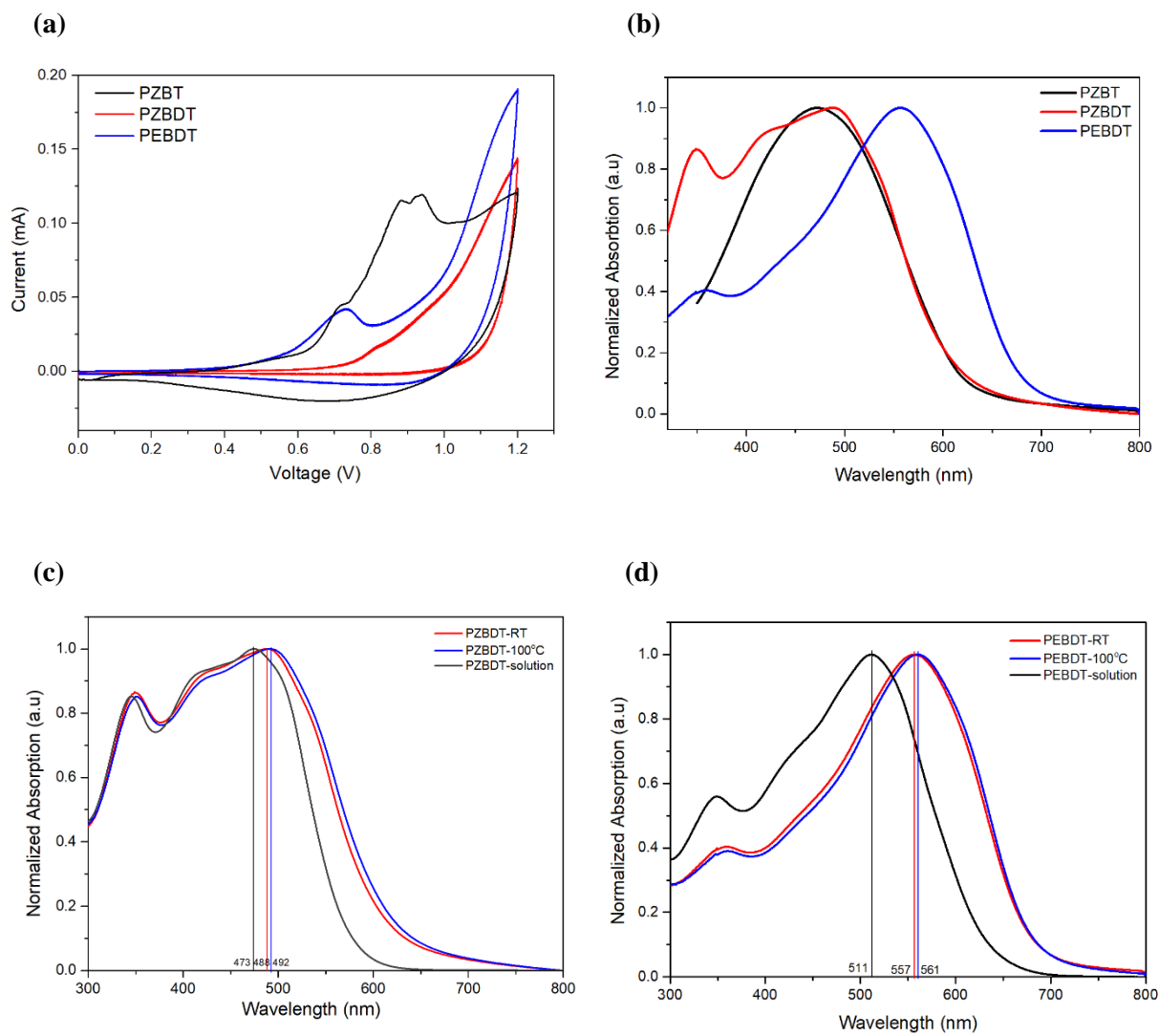


**Figure 2-7** Optical and electrical properties diagram of donor polymers PZBT, PZBDT and PEBDT, **(a)** Cyclic voltammetry profiles with 0.1M [n-Bu$_4$N]$^+$[PF6]$^-$ in acetonitrile solution as electrolyte at a scan rate of 0.1V/s, **(b)** Normalized UV-vis absorption spectra of polymer thin films at room temperature, **(c, d)** Normalized UV-vis absorption spectra of polymer solutions, polymer thin films at room temperature, and polymer thin films annealing under 100 ℃ for 30min.

32

**Table 2-2** Optical and electrical properties of TVT- ester based polymers

| Donor Polymer | $\lambda_{max,s}$ (nm) | $\lambda_{max,f}$ (nm) | $\lambda_{onset,f}$ (nm) | $E_g^{opt}$ (eV)[a] | $E_{HOMO}$ (eV)[b] | $E_{LUMO}$ (eV)[c] |
|---|---|---|---|---|---|---|
| PZBT | 458 | 472 | 623 | 1.99 | -5.41 | -3.42 |
| PZBDT | 473 | 488 | 610 | 2.03 | -5.50 | -3.47 |
| PEBDT | 511 | 557 | 677 | 1.83 | -5.33 | -3.50 |
| **Acceptor** | $\lambda_{max,s}$ (nm) | $\lambda_{max,f}$ (nm) | $\lambda_{onset,f}$ (nm) | $E_g^{opt}$ (eV)[a] | $E_{HOMO}$ (eV)[b] | $E_{LUMO}$ (eV) |
| (3PS)2-SiPc | / | 690 | 717 | 1.73 | -5.54 | -3.77[d] |
| Y6 | / | 830 | 933 | 1.33 | -5.71 | -4.10[7] |

[a] Obtained from thin-film absorption spectra.
[b] Obtained by equation $E_{HOMO} = -(4.80 + eE_{ox}^{onset})$.
[c] Obtained by equation $E_{LUMO} = E_{HOMO} + E_g^{opt}$.
[d] Obtained from CV onset reduction potential.
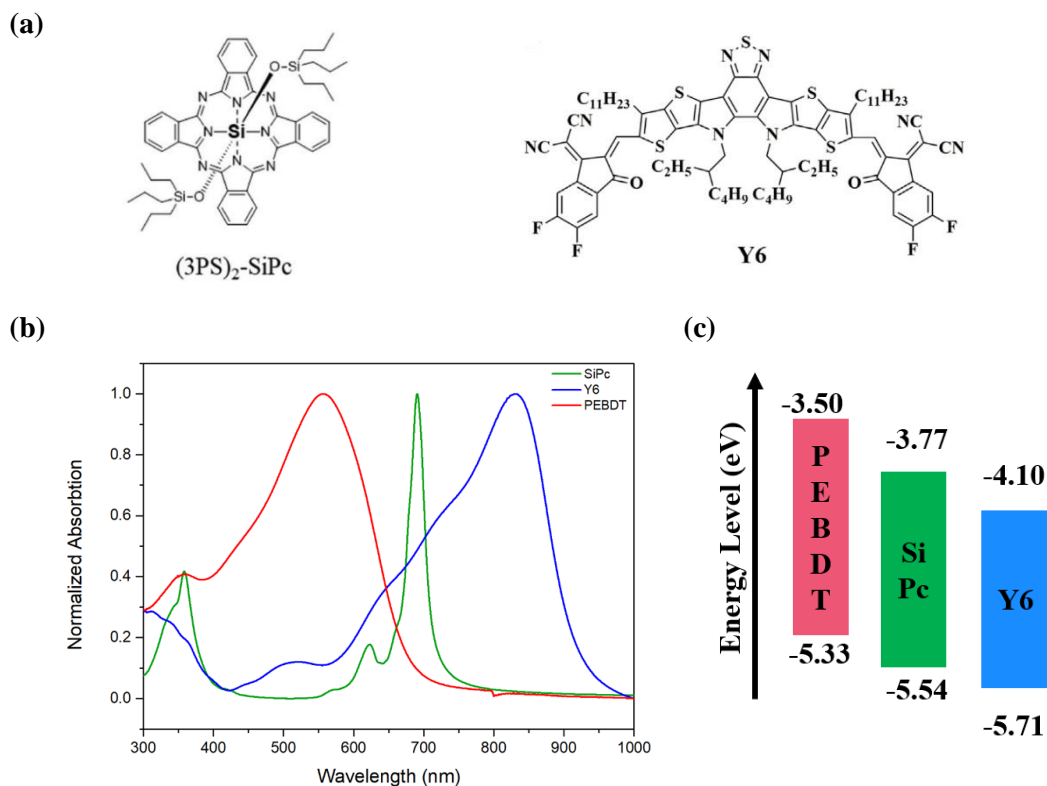


**Figure 2-8** **(a)** Chemical structures of two acceptors (3PS)2-SiPc and Y6, **(b)** UV-vis absorption spectra of PEBDT with acceptors, **(c)** Energy levels diagram of PEBDT and acceptors

The candidate non-fullerene acceptors (NFA) to match with donor material PEBDT were Y6 and (3PS)$_2$-SiPc. Y6 is a typical NFA material used in OSCs, with a low-lying $E_{HOMO}$ and a broad absorption range from 600nm to 1000nm, which can take full advantage of the near infrared light for the OSC devices to increase Jsc.[27] (3PS)$_2$-SiPc is a novel NFA based on silicon phthalocyanine derivative formed with only 1-step reaction, which has a relatively high $E_{HOMO}$ and $E_{LUMO}$, leading to a large offset between $E_{HOMO,D}$ and $E_{LUMO,A}$, and it is beneficial to enhance Voc of the OSC devices.[53] The optoelectrical properties of two acceptors were summarized in **Table 2-2** and **Figure 2-8**. The HOMO level energy offset ($\Delta E_{HOMO}$) between PEBDT and (3PS)$_2$-SiPc or Y6 are 0.21 eV and 0.38 eV, which is sufficient for exciton dissociation generating in acceptor phase. The LUMO level energy offset ($\Delta E_{LUMO}$) between PEBDT and (3PS)$_2$-SiPc or Y6 are 0.27 eV and 0.50 eV, respectively. Small energy offsets ($\Delta E_{LUMO}$, $\Delta E_{HOMO}$) are preferred for limiting the energy loss of OSC devices.[54]

The photoluminescence quenching efficiency (PLQE) technique was also carried out to investigate the exciton diffusion and dissociation performance of the donor and acceptor blend films ($W_D$: $W_A$ =1:1) before fabricating OSCs. The polymer PEBDT was excited at 550nm, where is the maximum absorption peak and meanwhile the low absorption intensity of (3PS)$_2$-SiPc and Y6, in order to get rid of photoluminescence from acceptors. After the blend film was excited at 550nm, the donor polymer PEBDT dominated emission, and the light emission should be quenched in D-A blend films due to the existence of acceptors. From the PL spectra shown in **Figure 2-9**, the PLQE of PEBDT blending with acceptors (3PS)$_2$-SiPc or Y6 were 91.3% and 92.5%, respectively. The PLQE of acceptors (3PS)$_2$-SiPc or Y6 with the introduction of PEBDT were 91.9% and 99.8%, respectively. From the results of quenching, both systems PEBDT: (3PS)$_2$-SiPc and PEBDT:Y6 showed good exciton dissociation performance.
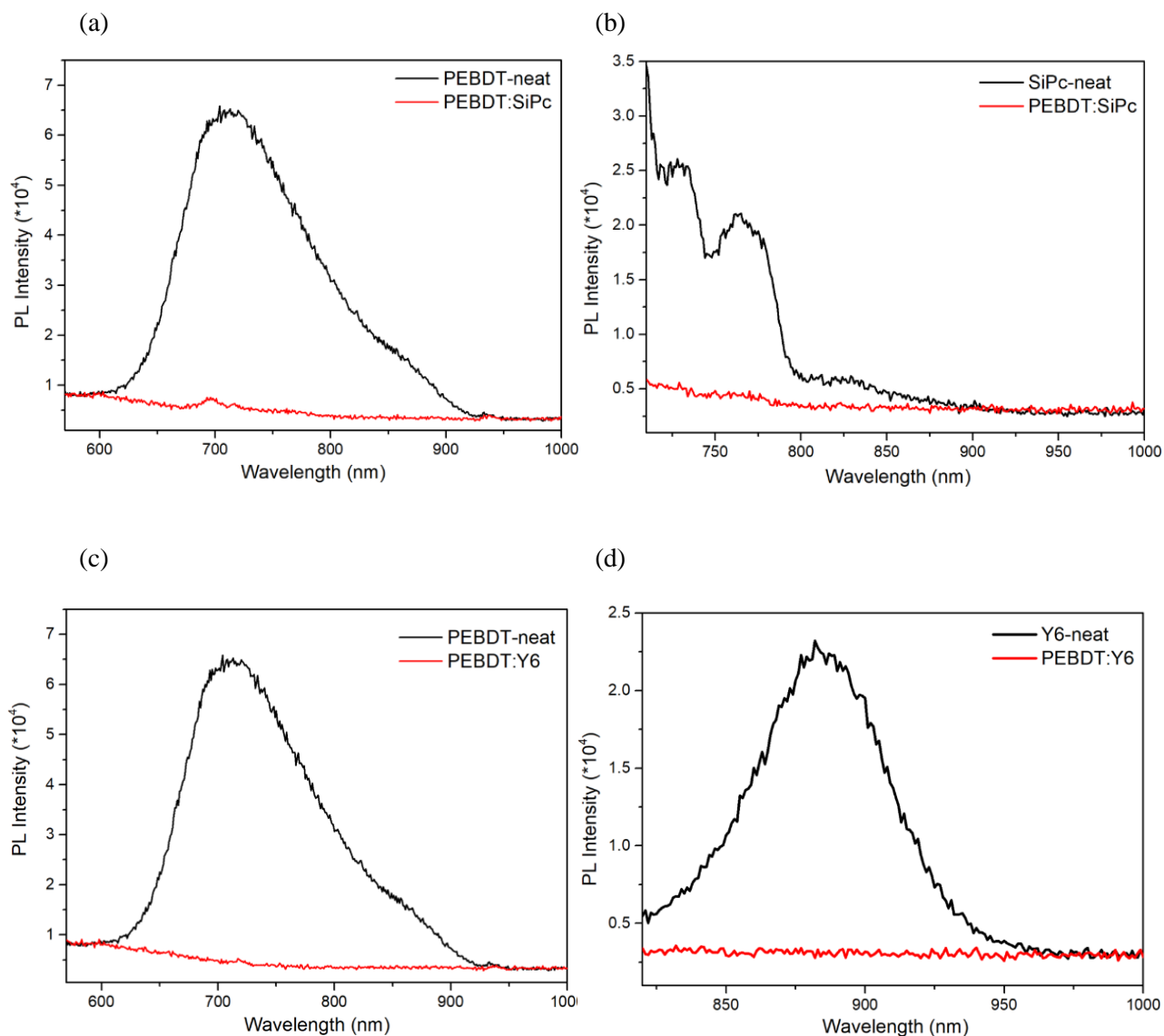
**Figure 2-9** Photoluminescence spectra of (a) PEBDT neat and PEBDT: $(3PS)_2$-SiPc blend film excited at 550nm, (b) $(3PS)_2$-SiPc neat and PEBDT: $(3PS)_2$-SiPc blend film excited at 690nm, (c) PEBDT neat and PEBDT:Y6 blend film excited at 550nm, (d) Y6 and PEBDT:Y6 blend film excited at 800nm.

The two-dimensional grazing-incidence X-ray diffraction (2D-GIXD) of the polymer neat films without annealing (RT) were shown in **Figure 2-10**. The neat film PZBT had no obvious peaks were observed in XRD patterns in-plane (IP) and out-of-plane (OOP) direction, indicating the polymer chains are amorphous and disordered due to the long alkyl side chains. The PZBDT showed weak $\pi$-$\pi$ stacking peaks (010) at $2\theta$ =22.3$^o$ (d ~ 0.4nm) in both IP and OOP directions, and a (100) diffraction peak at $2\theta$ = 4.2$^o$ in OOP direction, corresponding to the lamellar stacking of polymer backbone with a d-spacing 2.1 nm. Comparing to the PZBDT, the neat film of PEBDT presented a stronger lamellar peak at $2\theta$ = 4.3$^o$ (d~2.05nm) in OOP direction, and weaker $\pi$-$\pi$ peaks at $2\theta$ =22.0$^o$ (d ~ 0.4nm) in both IP and OOP directions. Thus, PZBDT and PEBDT formed an edge-on orientation with lamellar packing of the polymer backbone.
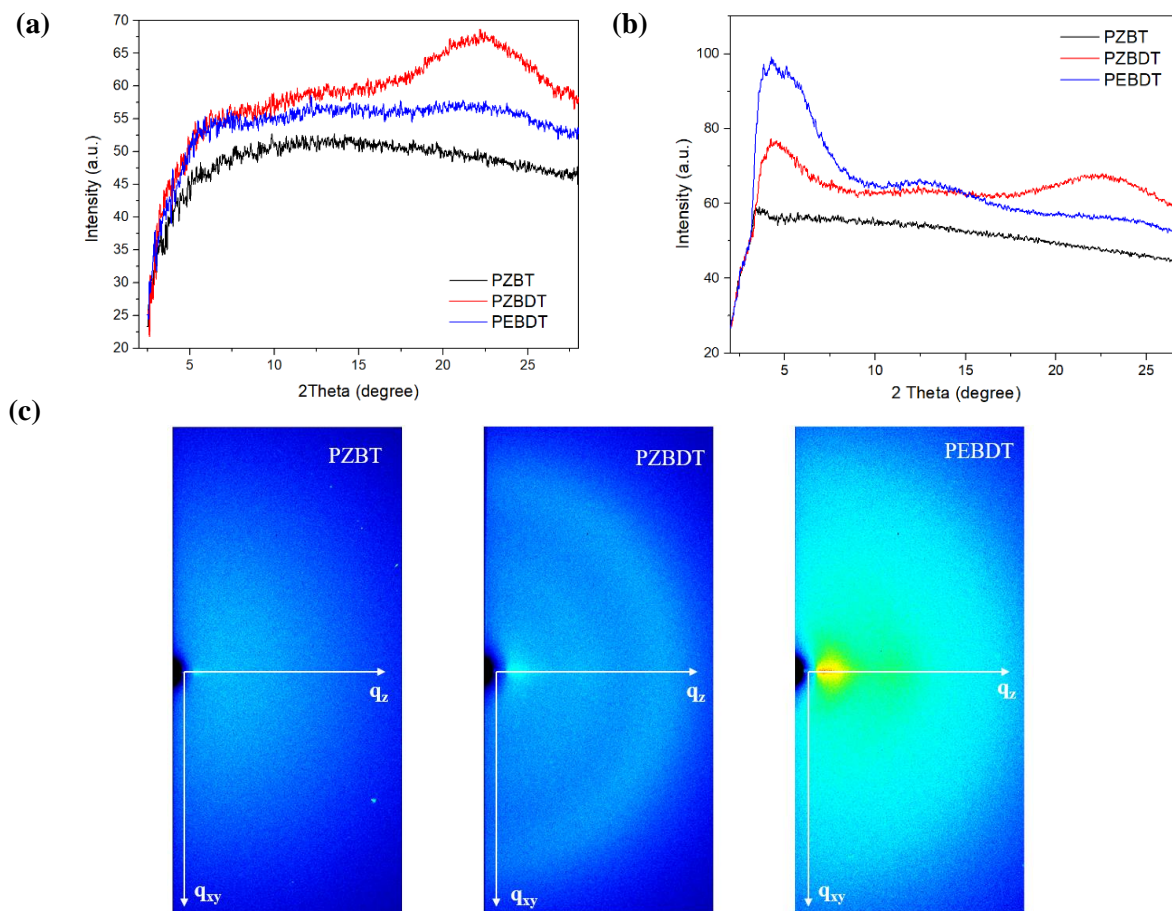
**Figure 2-10** GIXD patterns of TVT- ester based polymer neat films in room temperature **(a)** In-plane **(b)** Out-of-plane line cuts **(c)** 2D images.

## 2.4 Organic Solar Cell Performance of TVT-Ester Donor Polymers

The BHJ organic solar cells were fabricated using inverted configuration ITO/ZnO/Active layer/MoO$_3$/Ag, based on PEBDT: (3PS)$_2$-SiPc and PEBDT:Y6 as active layers. The device structure was shown in **Figure 2-11** and the details of device fabrication process were written in Chapter 2.6.2. The OSC devices were processed in nitrogen glove box under room temperature, and characterized under the illumination of AM 1.5G (100 mWcm$^{-2}$). The active layer D:A blend film was made from D:A=1:1 weight ratio mixture solution by spin-coating technique.
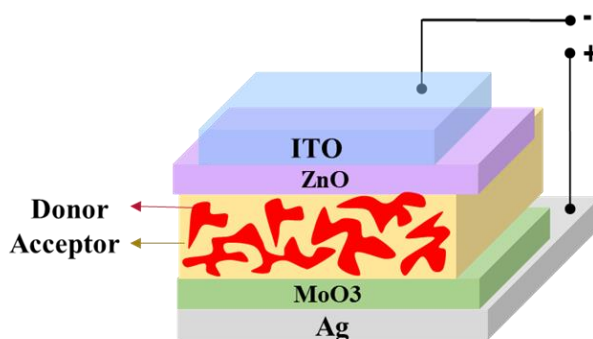


**Figure 2-11** Schematic of inverted configuration OSC device
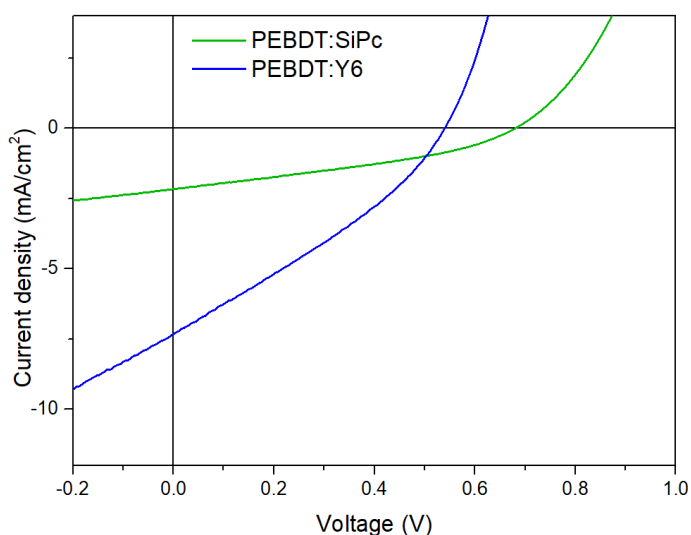
**Figure 2-12** Current density- Voltage (J-V) curves of OSCs based on PEBDT: $(3PS)_2$-SiPc and PEBDT:Y6 active layers. The active layer was made from D:A=1:1 weight ratio in 16 mg/mL chloroform solution spin-coating.

**Table 2-3** Summary of OSCs performance of PEBDT:SiPc and PEBDT:Y6

| Active layer (CF) | Thickness (nm) | Jsc (mA/cm$^2$) | Voc (V) | FF | PCE (%) | Rs (ohm/cm$^2$) | Rsh (ohm/cm$^2$) |
|---|---|---|---|---|---|---|---|
| PEBDT: $(3PS)_2$-SiPc | 90 | 2.16 | 0.68 | 0.35 | 0.52 | 22.42 | 463.98 |
| PEBDT:Y6 | 102 | 7.32 | 0.54 | 0.31 | 1.23 | 7.07 | 93.15 |

The organic solar cells based on PEBDT: (3PS)2-SiPc and PEBDT: Y6 blend films were fabricated, the device performance was shown in **Figure 2-12** and **Table 2-3**. For the comparative study, both systems were controlled under same manufacture process with same condition of buffer layers and electrodes. From **Table 2-3**, the optimized OSC for PEBDT:SiPc under room temperature showed the PCE value of 0.52% (Jsc=2.16 mA/cm$^2$, Voc=0.68 mA/cm$^2$, FF= 35%), and for the OSC based on PEBDT:Y6 blend film under room temperature had achieved the PCE value of 1.23% (Jsc=7.32 mA/cm2, Voc=0.54V, FF=31%).

For the photovoltaic performance of OSCs based on PEBDT: (3PS)2-SiPc blend film, comparing with the OSCs based on P3HT: (3PS)2-SiPc blend film in same inverted configuration reported by Grant (PCE= 4.3%, Jsc= 8.9 mA/cm$^2$, Voc=0.79, FF=0.61) [53], PEBDT: (3PS)2-SiPc system showed a lower PCE with small Jsc and FF. One possible reason of low Jsc is the thin film absorption coefficient of PEBDT ($\sim 4\times10^4$ cm$^{-1}$) is much lower than that of P3HT ($\sim 2\times10^5$cm$^{-1}$) [55], resulting in deficient light absorption and charge generation. By introducing the small molecule Y6 as acceptor in blend film, the light absorption range was broadened to near-infrared region and the Jsc was improved from 2.16

mA/cm$^2$ to 7.32 mA/cm$^2$. However, the Voc of both systems were low due to large voltage loss, which was calculated by the difference between charge-transfer state and open-circuit voltage (V$_{loss}$= (E$_{LUMO,A}$ – E$_{HOMO,D}$) -eVoc).[13] The V$_{loss}$ value of OSCs based on PEBDT: (3PS)2-SiPc and PEBDT:Y6 are 0.88 eV and 0.69 eV, respectively, which are larger than the average V$_{loss}$ value 0.5 eV[13]. This phenomenon might be mainly caused by non-radiative charge recombination at D:A interface, through structural defects and energetic traps, which relates to the aggregation and domain purity and results in low FF.

To further understand the photovoltaic properties of the polymer PEBDT, it is important to investigate the charge transport properties in the blend films. Thus, the vertical electron/hole mobilities of PEBDT:Y6 were measured by space-charge-limited current technique (SCLC). As shown in **Figure 2-13 (a, b)**, the hole-only device consists of ITO/ PEDOT:PSS/ active layer/MoO$_3$/Ag, and the electron-only device consists of ITO/ZnO/ active layer/LiF/Al. The devices were measured under applied voltage (0V~6V) to obtain J-V curve in dark (no light condition). The carrier mobilities $\mu$ can be calculated by fitting the J-V curves in near quadratic region according to the Mott-Gurney equation **Eq. 2-1** [56] :

$$J = \frac{9}{8}\mu\varepsilon\varepsilon_0\frac{V^2}{L^3}$$
$$\text{2-1}$$

where $J$ is the current density, $V$ is the voltage, $L$ is the thickness of active layer, $\varepsilon_0$ is the vacuum dielectric constant (8.85E-12 F/m), and $\varepsilon$ is the dielectric constant of the material. The value $\varepsilon$ can be calculated through **Eq. 2-2** [57], where the capacitance $C$ of electron-only or hole-only device is measured under $10^5$ Hz frequency. Parameter $d$ is the film thickness same as $L$ in **Eq. 2-1**, $\varepsilon_0$ is the vacuum dielectric constant (8.85E-12 F/m), and $A$ is the device area (0.0574 cm$^2$) :

$$C = \frac{\varepsilon\varepsilon_0 A}{d}$$
$$\text{2-2}$$

The electron mobility ($\mu_e$) and hole mobility ($\mu_h$) of PEBDT:Y6 blend films were calculated to be 0.84×10$^{-6}$ and 1.37×10$^{-6}$ respectively, and the $\mu_e$ /$\mu_h$ ratio was 0.61. It is known that the empirical value

of carrier mobilities from literature reported, which are usually above $1.0 \times 10^{-5}$ $cm^2V^{-1}s^{-1}$, and a balanced hole/electron ratio is preferred for a high performance device.[7] As a result, the low and unbalanced electron/hole carrier mobilities in PEBDT:Y6 blend film limit the Jsc and FF, which influence the performance of OSCs.[7]

**(a)**                                                                 **(b)**



**(c)**
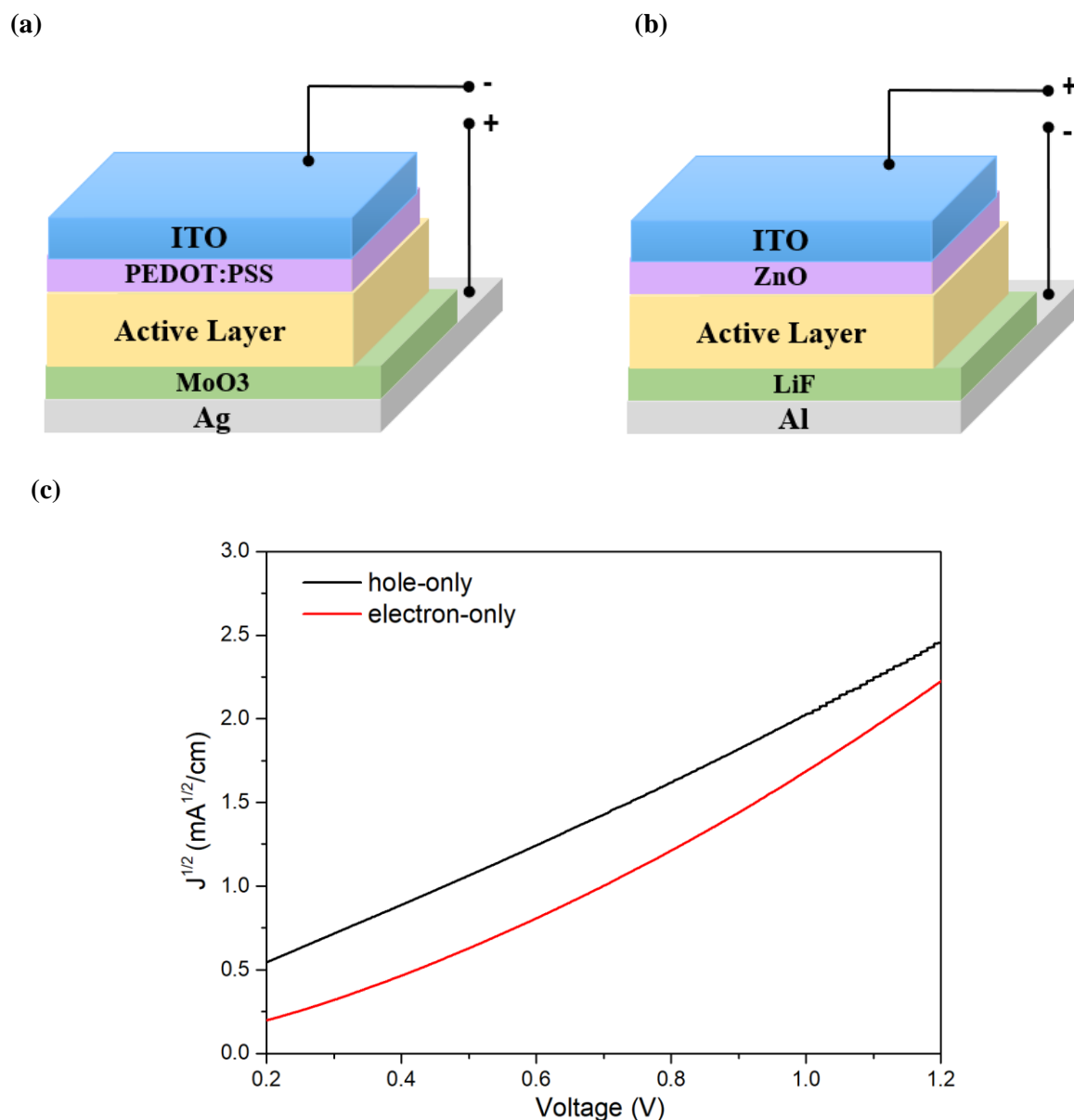


**Figure 2-13** Configuration of SCLC devices **(a)** hole-only **(b)** electron-only. **(c)** $J^{1/2}$-V curves of the hole-only and electron-only devices based on PEBDT:Y6.

To further understand the reason of low carrier mobilities and low FF, the thin film morphology of the PEBDT:(3PS)$_2$-SiPc and PEBDT:Y6 active layers were studied through atomic force microscopy (AFM), as shown in **Figure 2-14**. From the AFM height image of PEBDT:(3PS)$_2$-SiPc, a significantly large domains and rough surface with the root-mean-square (RMS) roughness of 15.77nm were observed, which may due to the highly crystalline property of (3PS)$_2$-SiPc.[53] Large domains were unfavorable for exciton dissociation and collection in the active layer resulting in low Jsc, and large roughness increased the contact resistance of the interface resulting in high Rs and low FF. The PEBDT:Y6 blend film showed better miscibility with the RMS of 1.26nm, and small grains can be observed. The high miscibility could lead to high PLQE (as shown in **Figure 2-9**), but also limit the charge collection process by lowering the carrier mobilities, which is consist with SCLC results. Although PEBDT:Y6 blend film had a smoother surface, the OSCs showed a lower FF than the device based on PEBDT:(3PS)$_2$-SiPc with a decreasing of Rsh, this may relate to the traps and defects inside the blend film, which will cause short circuit and lower the Voc.

**(a)**                                                  **(b)**
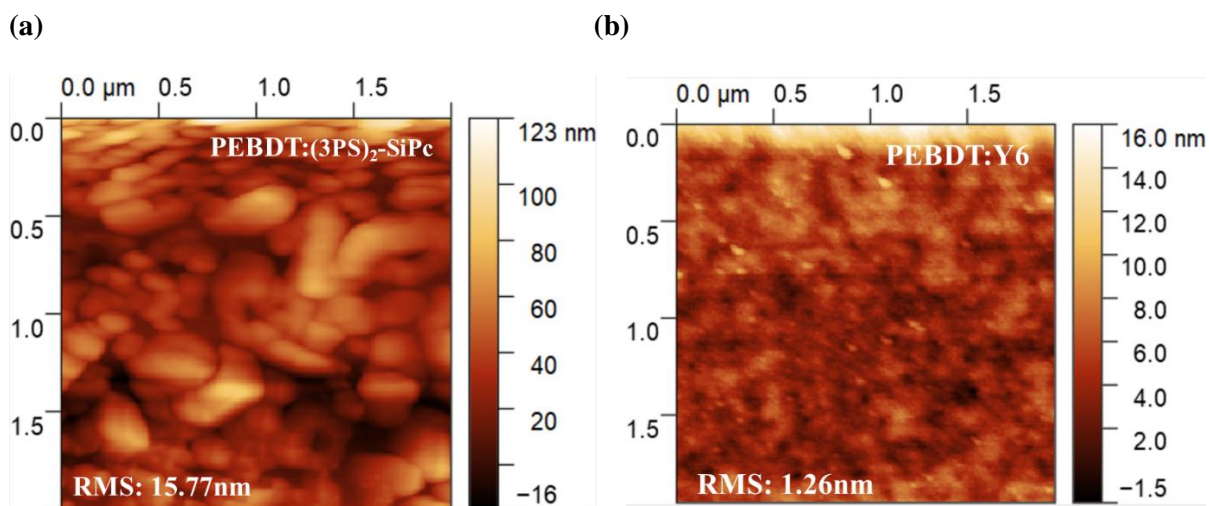


**Figure 2-14** AFM height images (2 μm × 2 μm) of blend film **(a)** PEBDT:(3PS)$_2$-SiPc and **(b)** PEBDT:Y6.

## 2.5 Summary and Future Directions

In summary, the novel ester-substituted vinyl backbone (TVT- ester) as a weak acceptor unit in donor polymer was designed, and TVT-ester based donor polymers PZBT, PZBDT, and PEBDT were synthesized through a few steps of synthetic routes which indicating the low cost of these materials. PZBDT and PEBDT are isomer polymers based on BDT donor unit, which are designed to improve the backbone planarity and film formability of polymer PZBT. Among them, the polymer PEBDT showed a relatively planar backbone structure and good film-forming property, which is favored in OSC film morphology. Then the optical and electrochemical properties were carried out through several techniques. The polymer PEBDT was demonstrated wide optical bandgaps, broad absorption range, and good quenching efficiency with two acceptors $(3PS)_2$-SiPc and Y6, indicating that it might be a promising candidate for OSCs. When the PEBDT applied to the OSCs as a donor material, a PCE of 0.52% based on PEBDT: $(3PS)_2$-SiPc blend film and a PCE of 1.23% based on PEBDT:Y6 blend film were obtained. Although the Jsc was improved from 2.16 mA/cm$^2$ to 7.32 mA/cm$^2$ by introducing Y6 to the blend film, both systems showed low Jsc, large $V_{loss}$ and low FF. The AFM suggested large domain size of the PEBDT: $(3PS)_2$-SiPc blend film and relatively smooth surface of PEBDT:Y6. The XRD showed weak diffraction peaks and low crystallinity of PEBDT, suggesting that disordered polymer chains arrangement in the thin film. The poor film morphology resulted in low charge transport property, which was revealed by SCLC measurement.

For the future work, the low Jsc, large $V_{loss}$, and low FF of PEBDT based OSCs were found to be limiting further photovoltaic performance improvement, which could be ascribed to poor film morphology with incontinuous network. The amorphous property and low carrier mobility of PEBDT could relate to its disordered sidechain packing, so it might be helpful to increase the planarity and rigidity of the backbone structure to achieve a more ordered molecule packing and enhanced charge carrier mobility. Besides, the $E_{HOMO}$ of PEBDT is relatively high in wide-bandgap donor polymers and

not matched with the acceptor Y6. From Wang's group study, one strategy is changing TVT backbone to ethenylene fused TVT which can effectively downshift the HOMO energy level, increase the absorption coefficient, and improve the backbone planarity.[58] As shown in **Figure 2-15**, the vinylene was connected to the adjacent thiophene with double bond (C=C) to form the fused ring structure **4-F**, and polymer **1** is obtained after copolymerization of BDT unit and **4-F**. The dihedral angle between fused ring and backbone was calculated by DFT simulation. Additionally, by changing the substituted position of ester sidechain, the dihedral angle could be effectively reduced, as shown on polymer **2** and **3**. However, the fused ring structures of polymer **2** and **3** are difficult in synthesis, which will increase the cost of organic solar cell devices. Thus, the new designed structures **2** and **3** were not further synthesized, but the strategies based on fused ring formation and sidechain position adjustment of polymer are useful for optimizing structure in the future.
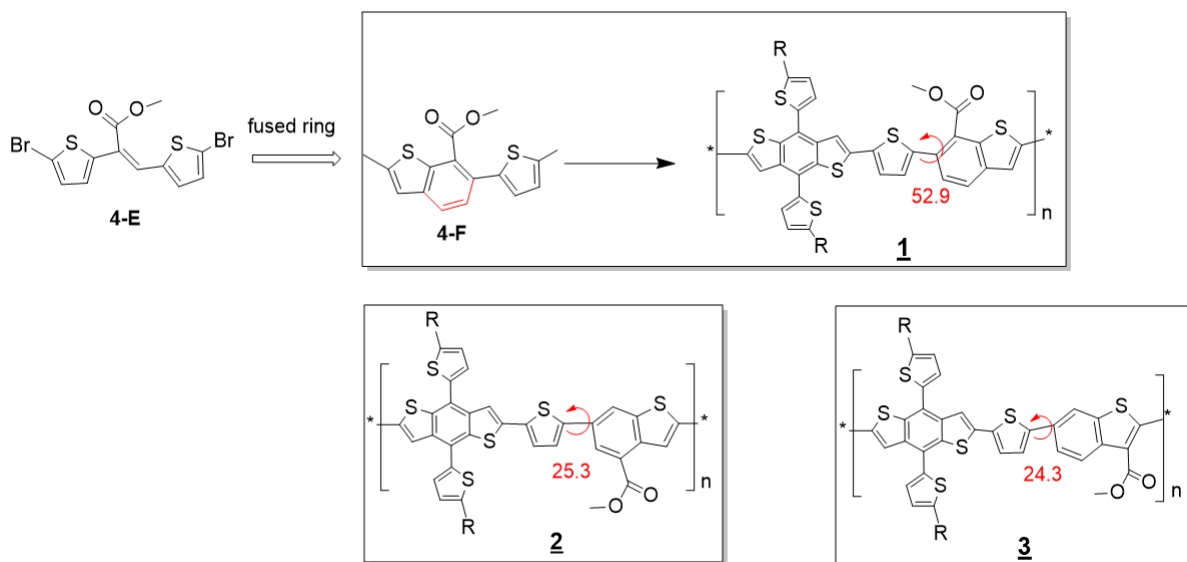


**Figure 2-15**  Chemical structures of TVT molecule **4-E**, ethenylene fused TVT molecule **4-F**, and ethenylene fused TVT polymers **1**, **2**, **3**.

## 2.6 Experimental Section

### 2.6.1 Materials Characterization

All the solvents and chemical materials were obtained commercially and utilized without further purification. The density function theory (DFT) simulations were calculated by Gaussian 09 software with basis set B3LYP/6-31G (d). The High-temperature GPC was measured with Agilent PL-GPC220 using 1,2,4-triclorobenzene as eluent and polystyrene as standard at 150 $^{\circ}$C. The thermogravimetric analyses (TGA) and differential scanning calorimetry (DSC) were measured using TA Instruments SDT 2960 at scan rate of 10 $^{\circ}$C min$^{-1}$ under nitrogen. Cyclic Voltammetry (CV) was measured on a CHI600E electrochemical analyzer using Ag/AgCl as reference electrode, two Pt disk electrodes as working electrode and counter electrode, in 0.1M tetrabutylammonium hexafluorophosphate solution in acetonitrile at a scan rate of 100 mV/s. Ferrocene was function as reference system with $E_{HOMO}$= -4.8 eV. The Pt working electrode was coated with polymer film. The UV-Vis spectra was obtained by Cary 7000 Universal Measurement Spectrophotometer. The PL spectra was obtained by Horiba PTI QuantaMasterTM 8000 Series Fluorimeter. The NMR data was recorded using a Bruker DPX 300 MHz spectrometer with chemical shifts relative to tetramethyl silane (TMS, 0 ppm). Two-dimensional grazing-incidence X-ray diffraction (2D-GIXD) patterns were carried out on a Bruker D8 Discover power diffractometer with Cu Ra (Rigaku) X-ray source ($\lambda = 0.15418$ nm) in standard Bragg-Bretano geometry. Atomic force microscopy (AFM) images were measured by Dimension 3100 Scanning Probe microscope on the blend film.

### 2.6.2 OSC Devices Fabrication and Characterization

The BHJ organic solar cells with inverted configuration were fabricated in ITO/ZnO/Active layer/MoO$_3$/Ag layer by layer. The ITO electrode is cathode and Ag electrode is anode. The ITO glass substrates were washed and sonicated in DI water, acetone, and iso-propanol for 20 min, respectively.

After washing, the ITO glass substrates were dried under nitrogen flow and treated under oxygen plasma cleaning for 10 min. Then ZnO layer (~40nm)  was spin-coated on ITO substrate and remove the ZnO on edge by Q-tips with acetone to expose the electrode. The ZnO layers were annealed on hot plate at 200°C for 1h in air. The substrates were transferred into nitrogen glovebox for further active layer coating. The D:A mixture solution was prepared ahead and stirred overnight. The D:A mixture solution was filtered in glovebox with 0.45μm PTFE. Control the spin-coating speed to obtain the preferred active layer thickness. Put the substrates on hot plate for 10min if the thermal annealing treatment is needed. Finally, a 10nm $MoO_3$ and 100nm Ag electrode were deposited on the substrates under vacuum of $1x10^{-6}$ torr. The J-V curve was measured using Agilent B2912A semiconductor Analyzer with Science Tech SLB300-A Solar Simulator. Each solar cell active area is 0.0574 $cm^2$. The light source was A 450W xenon lamp with an air mass (AM) 1.5 filter.

### 2.6.3 Synthesis Routes

**Synthesis of 2-(5-bromothiophen-2-yl)acetic acid (1)**
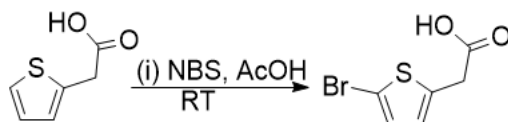


2-thiopheneacetic acid (3.5 g, 24.6 mmol), NBS (4.82g, 27.1mmol), and acetic acid (15 mL) were added to a two-neck flask and stirred at room temperature under $N_2$ overnight. After 20h reaction, test TLC using ethyl acetate : Hexane =2:1, starting material was consumed and the product has higher polarity than the starting material (Fig.1b). The reaction solution was concentrated under vacuum to remove acetic acid. Then pour the residue into DI water and stir for 1h. The black solid was obtained by filtration. (Yield: 3.17g, 58%) 1H NMR (300 MHz, CDCl₃, δ/ppm): 6.93 (d, 1H), 6.74 (d, 1H), 3.84 (s, 2H).

**Synthesis of (Z/E)-2,3-bis(5-bromothiophen-2-yl)acrylic acid (2-Z, 2-E)**
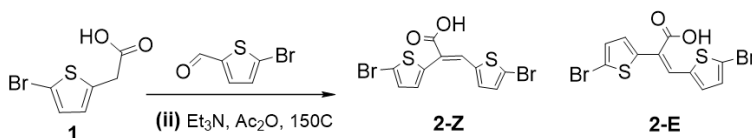


2-(5-bromothiophen-2-yl)acetic acid (**1**) (1.4g, 6.33mmol), 5-bromothiophene-2-carbaldehyde (1.2g, 6.33 mmol), triethylamine (2.6 ml) and acetic anhydride (2.6 mL) were added into flask and stirred at 150 °C for 1 hour. The resulting dark brown reaction mixture was cooled down to room temperature, poured into a stirred 10% HCl (200ml) solution which offered a black precipitate that was extracted with diethyl ether. The ether phase is black, with much floccule in both ether and HCl phase. Dump the light yellow HCl phase and use 10% NaOH to extract the ether phase and black precipitate. After adding 100ml 10% NaOH and shaking, the black precipitate was filtered and dried the solid in vacuum oven (**2-Z**). The 10% NaOH solution resulted in a yellow aqueous phase, was carefully acidified to pH 5 by addition of acetic acid while stirring, offering very little black solid. Continue acidified to pH 1 with concentrated HCl, offering a little yellow solid. Filter the yellow solid off and dry in vacuum oven (**2-E**). (Yield: 1.01g, 40.4%) 1H NMR (300 MHz, DMSO, δ/ppm) **2-E**: 7.39 (s, 1H), 7.32 (d, 1H), 7.26 (d, 1H), 7.20 (d, 1H), 7.12 (d, 1H). **2-E**: 8.06 (s, 1H), 7.47 (d, 1H), 7.30-7.27 (m, 2H), 6.95 (d, 1H).

**Synthesis of 2-butyloctyl (Z)-2,3-bis(5-bromothiophen-2-yl)acrylate (3-Z)**
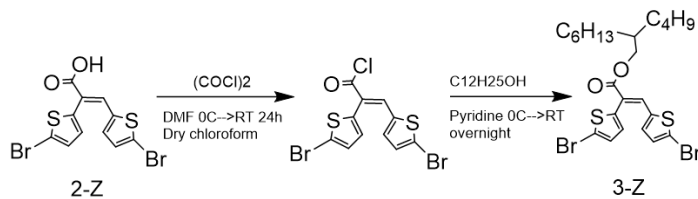


**2-Z** (0.3g, 0.76mmol) was added to the 2-neck round bottom flask along with anhydrous chloroform (3mL). The flask was cooled to 0°C using an ice bath and oxalyl chloride (0.145g, 1.14mmol) was added slowly with one drop of DMF (0.1mL). After addition of oxalyl chloride, the reaction was warmed to room temperature stirring overnight. After 24h, a glass vacuum trap in an ice bath was used

46

to remove the solution volume for 4h. Then, dry chloroform (3mL) was added, and the reaction was again cooled to 0°C and $C_{12}H_{25}OH$ (0.20mL) was added slowly. Adding pyridine (0.08ml) slowly after that. Then the reaction was stirred under room temperature overnight. The product was extracted with DI water and DCM, then the organic layer was further purified by column chromatography using eluent DCM: Hexane from 1:7 to 1:1. (Yield: 0.22g, 51%) 1H NMR (300 MHz, CDCl₃, δ/ppm): 7.94 (s, 1H), 7.06-7.02 (m, 2H), 6.96 (d, 1H), 6.74 (d, 1H), 4.07 (d, 2H), 1.60 (s, 1H), 1.26-1.22 (m, 16H), 0.86 (t, 6H).

**Synthesis of methyl (Z/E)-2,3-bis(5-bromothiophen-2-yl)acrylate (4-Z, 4-E)**
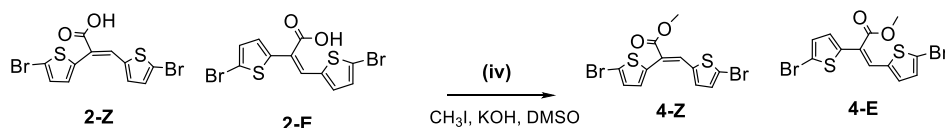


The mixture of **2-Z** and **2-E** (0.20g,1eq.), KOH (0.04g, 1.4eq) were dissolved in DMSO (3.0ml) in a 25 mL flask and stirred for 1h. Iodomethane (0.108g, 1.5eq.) was added to the solution, and the reaction mixture was continuing stirred under room temperature. After 1.5h reaction, adding 10ml water to stop the reaction. The product was extracted with DI water and DCM. Dry the organic phase with $Na_2SO_4$. The crude product contains some large polarity side products, which was further purified by column chromatography using Ethyl acetate: hexane from 1:7. First spot was obtained as **4-E** and second spot as **4-Z** in yellow liquid. (Yield: 0.198 mg, 95.6%) 1H NMR (300 MHz, CDCl₃, δ/ppm) **4-E**: 7.11 (s, 1H), 7.03-6.98 (m, 3H), 6.90 (d, 1H), 3.96 (s, 3H). **4-Z**: 8.01 (s, 1H), 7.12 (d, 1H), 7.08 (d, 1H), 7.00 (d, 1H), 6.80 (d, 1H), 3.81 (s, 3H).

47

## Synthesis of Polymer PZBT
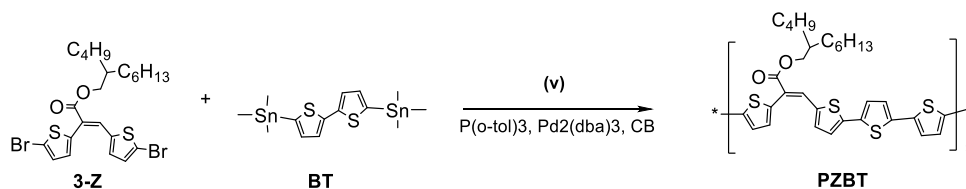


Monomer **3-Z** (0.1g, 0.1778 mmol, 1.0 eq), **BT** (0.087g, 0.177 mmol, 1.0eq), p(o-tol)3 (0.0043g, 0.08 eq),  Pd$_2$(dba)$_3$ (0.0032g, 0.02 eq), and  anhydrous chlorobenzene (3.6ml) were added into a 25ml flask. The reaction device was deoxygenated with argon for three times and then the mixture reacted at 90°C overnight under argon. After 18h reaction, dark purple mixture was formed. After cooling down to room temperature, methanol was added to wash the mixture and then vacuum filtration. Red solid and yellow solution were formed and filtered. Soxhlet extraction was applied using acetone, hexane, and chloroform. After washing with chloroform, obtained  purple pieces polymer. (Yield: 53mg, 52.6%)

## Synthesis of Polymer PZBDT
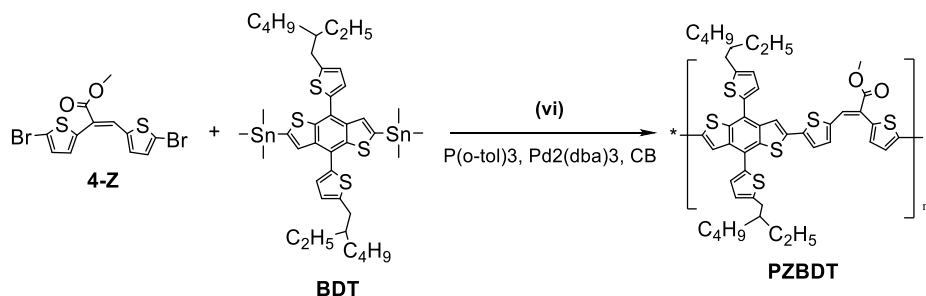


Monomer **4-Z** (0.057g, 0.14mmol, 1.0eq), **BDT** (0.126g, 0.14mmol, 1.0eq), p(o-tol)$_3$ (3.4mg, 0.08eq), Pd$_2$(dba)$_3$ (2.56mg, 0.02eq), and  anhydrous chlorobenzene (4ml) were added into a two-necked round bottom flask. The reaction device was deoxygenated with nitrogen for three times and then the mixture reacted at 90°C under argon. After 40h reaction, the solution become purple and viscous. Red solid precipitated out 100ml methanol after cooling down to room temperature. Using Soxhlet extraction to

48

purify the red solid, the solvents were acetone, hexane, and chloroform, respectively. After washing

with chloroform, purple pieces polymer was obtained. (Yield: 86mg, 75%)


**Synthesis of Polymer PEBDT**
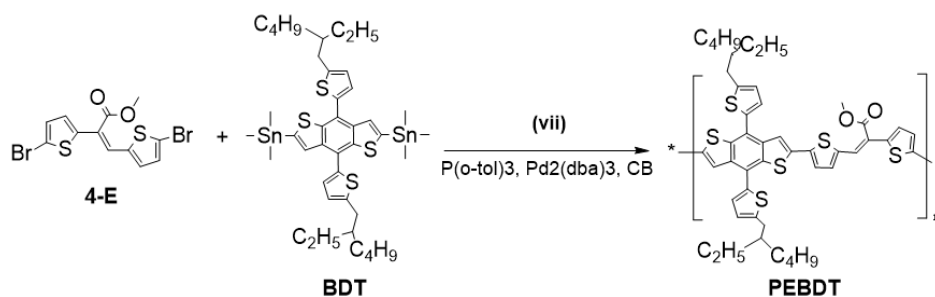


Monomer **4-E** (0.04g, 0.098mmol, 1.0eq), BDT (0.089g, 0.098mmol, 1.0eq), p(o-tol)$_3$ (2.38mg, 0.08eq),

Pd$_2$(dba)$_3$ (1.79mg, 0.02eq), and anhydrous chlorobenzene (4ml) were added in a 25nl two-necked flask.

The reaction device was deoxygenated with nitrogen for three times and then the mixture reacted at

90°C under nitrogen. After 40h reaction, the mixture became viscous and purple. The crude product

was washed with 100ml methanol and filtered. Soxhlet extraction was applied to further purity the

polymer, with the solvents of acetone, hexane, and chloroform, respectively. Obtained purple pieces

polymer from chloroform. (Yield: 73mg, 90%)

# Chapter 3  Synthesis and Characterization of Thiophene-Alkyloxime (TO) Based Donor Polymers

## 3.1 Introduction

The Bulk heterojunction (BHJ) organic solar cells (OSCs) utilize the blend film containing polymer donor and small molecule acceptor as the core part. In the past years, non-fullerene small molecule acceptors (NFAs) have made significant progress, resulting in a continuous rise in PCE of OSCs.[49] Among the various of NFAs, Y6 and its derivatives have been widely used with low-lying $E_{HOMO}$ and strong absorption in NIR, which has led to PCEs over 18% when combined with polymer donors.[27,59] To provide greater compatibility with the NFAs, the trend of donor polymer structure design is toward wide bandgap, low-lying $E_{HOMO}$, and low-cost processability.[49] The donor-acceptor (D-A) copolymer structure in donor polymer design has received much interest nowadays. The structure is based on alternating electron donating unit (D) and weak electron withdrawing unit (A) which can tailor the energy levels effectively. In chapter 2, the ester-substituted vinyl backbone was introduced, which function as a weak acceptor unit in donor polymer to tune the energy level, and three wide-bandgap polymer was synthesized and characterized.

In this chapter, another novel weak acceptor unit in wide-bandgap donor polymer will be discussed, based on alkyloxime sidechain substituted thiophene unit (TO), for obtaining wide-bandgap and low-lying HOMO level donor polymers. Recently, our group has reported two donor polymers namely PTOBT and PBDTTO, utilizing BT or BDT unit as donor backbone and electron-withdrawing group alkyloxime as weak acceptor sidechain, with deep HOMO level of -5.43 eV and -5.60 eV, respectively.[54,60] Both alkyloxime based polymers had very low synthetic complexity and achieved high PCE of 9.04% and 13.29% based on PTOBT:ITIC and PBDTTO:Y6 blend films.[54,60]
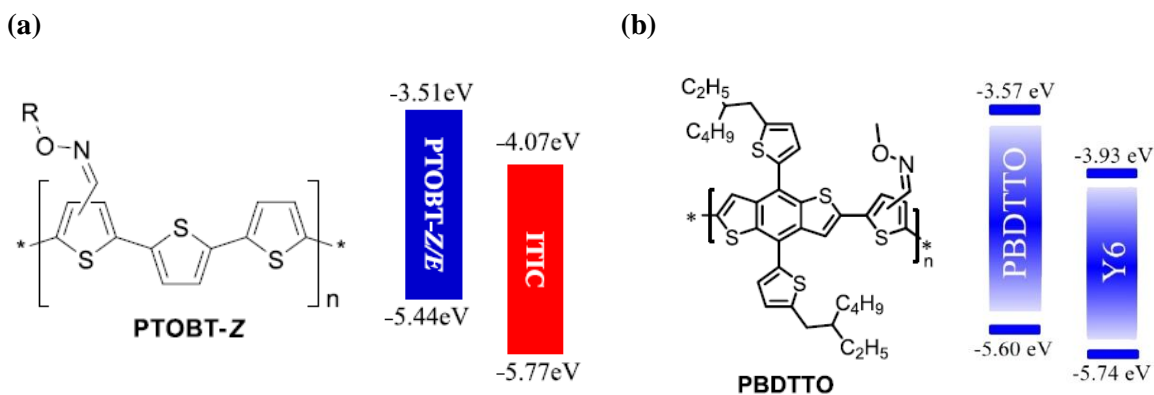
**Figure 3-1** Structures and energy levels alignment of **(a)** PTOBT and acceptor ITIC, **(b)** PBDTTO and acceptor Y6. [54,60]

The structure of two thiophene-alkyloxime based donor polymers reported by He et.al were shown in **Figure 3-1**.[54,60] The alkyloxime side chain (-C=N-OR) function as an electron-withdrawing group due to the existence of the strong electronegative atoms N and O. According to He's research, the alkyloxime sidechain (-C=N-OR) can be easily synthesized through two methods: one is using condensation reaction between an aldehyde (or ketone) and an alkoxyamine ($R-O-NH_2$); another is substitution the oxime (-C=N-OH) with an alkylhalide (R-X) [54]. From the synthesis route, the thiophene-alkyloxime based polymers are dementated to be low-cost, high-yield, and stable in air.

## 3.2 Polymer Structure Design

From the two previously reported thiophene-alkyloxime (TO) based polymers, by replacing BT with BDT donor unit in the backbone, the HOMO energy level was down-shifted, and SCLC hole mobility was increased, while less crystalline structure and disordered polymer chains were observed through XRD. Thus, there are still spaces of improvement on the polymer structure design to achieve better photovoltaic properties.[60] As a further development of TO based polymers, two novel polymers with alkyloxime side chains were designed by combining the advantages of BDT-based polymer PBDTTO and BT-based polymer PTOBT in the backbone structures: P3TOBDT and P4TOBDT (**Figure 3-2**).

51
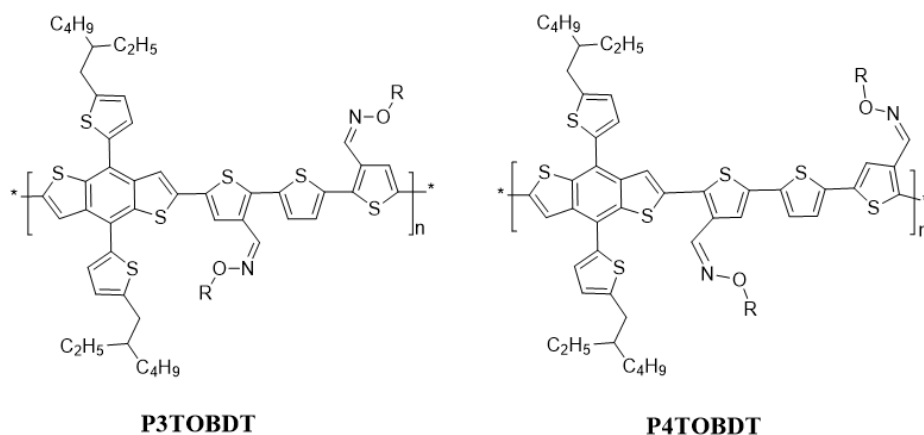
**Figure 3-2** Structures of two novel designed thiophene-alkyloxime (TO) based polymers

As shown in **Figure 3-2**, the structural isometric polymers P3TOBDT and P4TOBDT possess the same donor backbone structure consisting of one BDT unit with three thiophene units, which were designed based on the benefits of BDT for high hole mobility and BT for ordered polymer packing. Two Z-type alkyloxime side chains as weak electron withdrawing group were substituted on spaced thiophenes for downshifting the HOMO energy level, avoiding steric effect, and guaranteeing backbone planarity. The carbon chain on each alkyloxime unit was methyl heptane, which was the optimizing length for proper polymer solubility in chloroform. Both P3TOBDT and P4TOBDT were copolymerized by BDT and the terthiophene unit via Stille-coupling method. The axisymmetric alkyloxime substituted terthiophene unit avoids regiorandom backbone, leading to certain linking models between BDT and terthiophene, which contributes to π-π stacking between polymer chains.

52

### 3.2.1 Polymer Simulation by Density Functional Theory

Firstly, the Density Functional Theory (DFT) was applied to simulate the monomer units of two donor polymers, 3TOBDT and 4TOBDT, to foresee their frontier energy levels and optimized geometries. The simulations were run under Gaussian 09 at B3LYP/6-31G(d) basis set. The optimized geometries with dihedral angle of the repeating unit of P3TOBDT and P4TOBDT are shown in the **Figure 3-3.** For the monomer unit of two polymers, the dihedral angles between BDT unit and thiophene units in the backbone are 9°, 37°, and 38° for 3TOBDT, 37°, 23°, and 19° for 4TOBDT. The monomer 3TOBDT showed a slightly more planar backbone than the 4TOBDT with less steric effect between BDT unit and adjacent alkyloxime sidechains. Meanwhile, the distance between the O atom on alkyloxime sidechain and the H atom on the local thiophene in 3TOBDT and 4TOBDT are both 2.26 Å, which is smaller than the van der Waals radii between H and O (2.72 Å), suggesting that a hydrogen bond was formed inside the thiophene-alkyloxime unit when the alkyloxime chain in Z-type.[60]

The simulated energy levels and charge distribution of two monomer units were also shown in the **Figure 3-3**. The calculated energy level of 3TOBDT were $E_{LUMO}$= -2.14 eV and $E_{HOMO}$= -5.07eV, while 4TOBDT had a slightly higher of $E_{LUMO}$= -2.04 eV and $E_{HOMO}$= -5.06 eV. The 3TOBDT had most LUMO levels delocalizing around TO unit and partial on BDT, and HOMO levels delocalizing most on BDT and partial TO unit. In contrast, the 4TOBDT showed a highly delocalized charge distribution with both HOMO and LUMO along the backbone. The difference of charge distribution between two monomer units suggesting that 3TOBDT should be a little bit more electron-deficient than 4TOBDT.
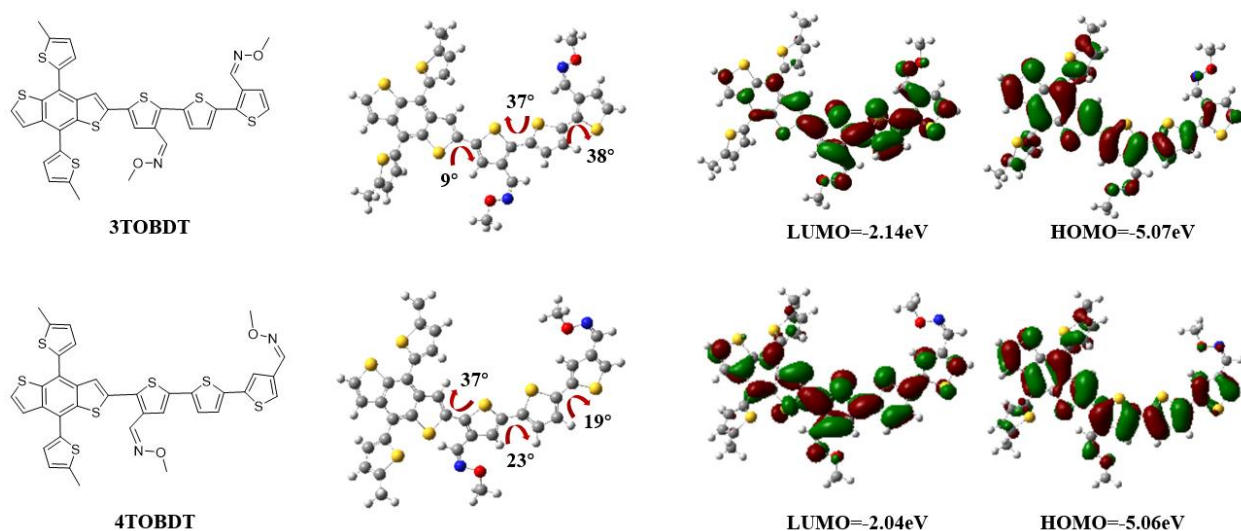
**Figure 3-3** Optimized geometries and predicted energy levels of P3TOBDT and P4TOBDT.

### 3.2.2 Monomers and Polymers Synthesis

The polymers P3TOBDT, P4TOBDT and their monomers M3, M4 were synthesized by following the synthesis route shown in **Figure 3-4,** and the detail synthetic routes with NMR data were listed in **Chapter 3.6.3**. Both polymers were starting with bromothiophene-carbaldehyde chemicals (**1a,1b**), followed by Knoevenagel condensation with hydroxylamine to obtain **2a** and **2b** in a high yield of 95%. Then the alkylation of **2a** and **2b** with 2-ethylhexane bromide forming the chemicals **3a** and **3b** with Z-type side chains in a yield around 50% after column chromatography.[54] Next, 2 equiv **3a** and **3b** were coupled with 1 equiv thiophene unit under Stille coupling conditions using $Pd_2(dba)_3/P(o\text{-}tol)_3$ as a catalyst in toluene at 100 °C for 20h to form **4a** and **4b**, respectively. After purifying through column chromatography, **4a** and **4b** were brominated with 2 equiv NBS to afford the monomers **M3** and **M4**. Finally, two novel alkyloxime based polymers were synthesized via Stille coupling polymerization of **M3** or **M4** with BDT unit using $Pd_2(dba)_3/P(o\text{-}tol)_3$ as a catalyst in chlorobenzene.[54,60] After reacting for 24h at 90 °C in argon atmosphere, the cooling down mixture was precipitated in methanol and it

54

was further washed with acetone and hexane through Soxhlet extraction. Finally, the polymer was extracted by chloroform and obtained shiny red-purple films after removing the solvent.[51]
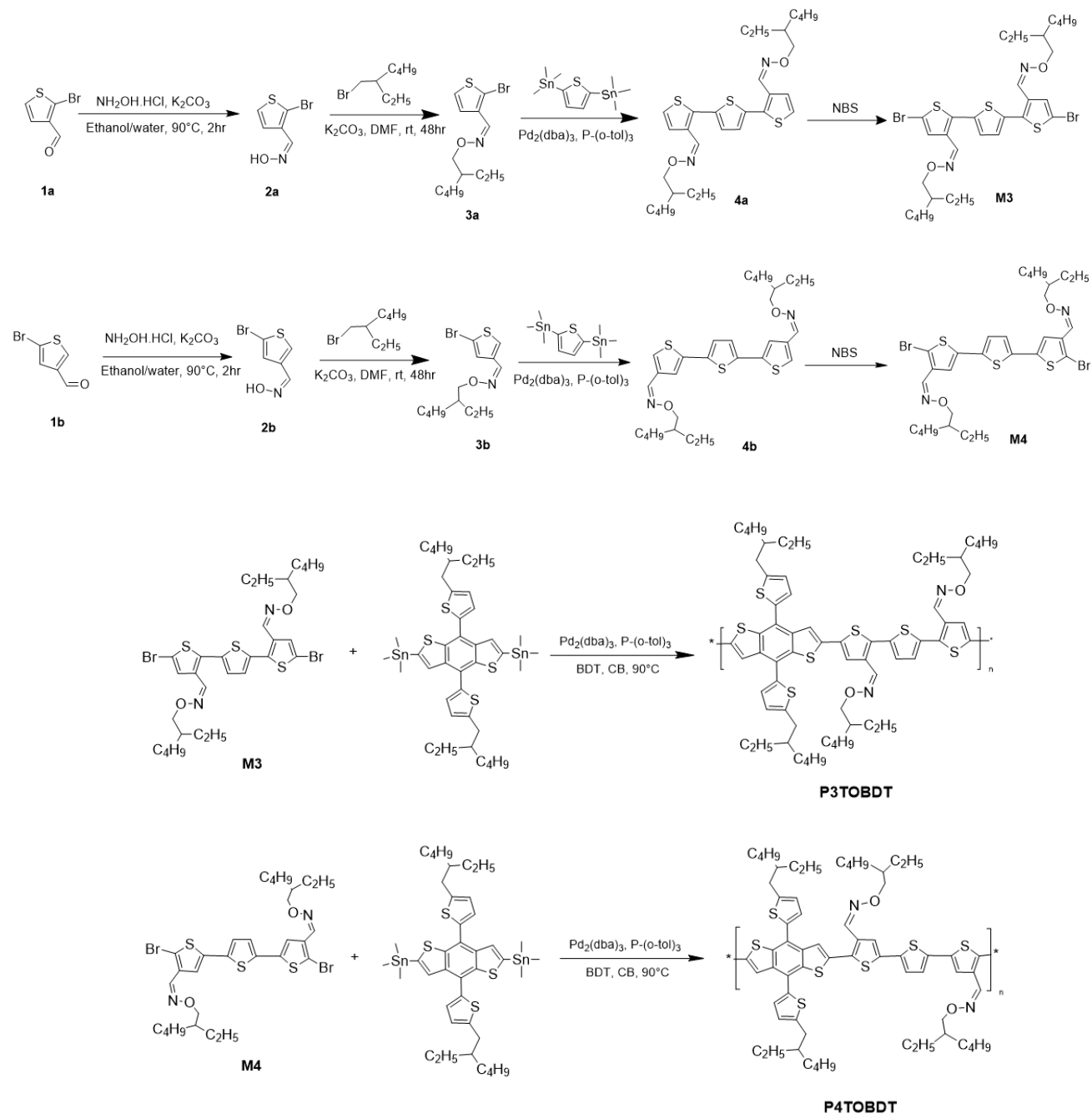


**Figure 3-4** Synthesis route towards monomers and polymers of P3TOBDT and P4TOBDT

## 3.3 Characterization of Thiophene-Alkyloxime Based Polymers

### 3.3.1 Physical Properties (GPC, TGA, and DSC)

The molecular weight of the TO based polymers were measured by high-temperature gel permeation chromatography (HT-GPC) with 1,2,4-trichlorobenzene as eluent and polystyrene as standards at 110 °C. The number average molecular weight (Mn) of P3TOBDT and P4TOBDT were measured to be 60.6 kDa and 18.7 kDa, and the polydispersity index (PDI) were determined to be 2.77 and 1.85, respectively. P3TOBDT showed a much higher molecular weight than P4TOBDT, the reason could be that the more ordered backbone packing of P3TOBDT is beneficial for polymerization to obtain longer chains.

The thermal stability of polymer P3TOBDT and P4TOBDT were investigated by thermalgravimetric analysis (TGA) and differential scanning calorimetry (DSC). As shown in the **Figure 3-5 (a)**, TGA was measured with heating rate of 10°C min$^{-1}$ under nitrogen. P3TOBDT showed 1% weight loss at 263°C and its first step decomposition at 307°C, second step decomposition at 411°C. P4TOBDT lost its 1% weight at 236°C. and its first step decomposition at 284°C, second step decomposition at 431°C. Both polymers exhibited good thermal tolerance making them ideal for OSCs that require a high temperature tolerance. DSC measurement was obtained with a scanning rate of 10°C min$^{-1}$ under nitrogen, as shown in **Figure 3-5 (b)**, no obvious phase transition was observed in the whole temperature range, indicating that their melting points are higher than the decomposition temperatures or they are in low crystallinity.[60]

**(a)** **(b)**
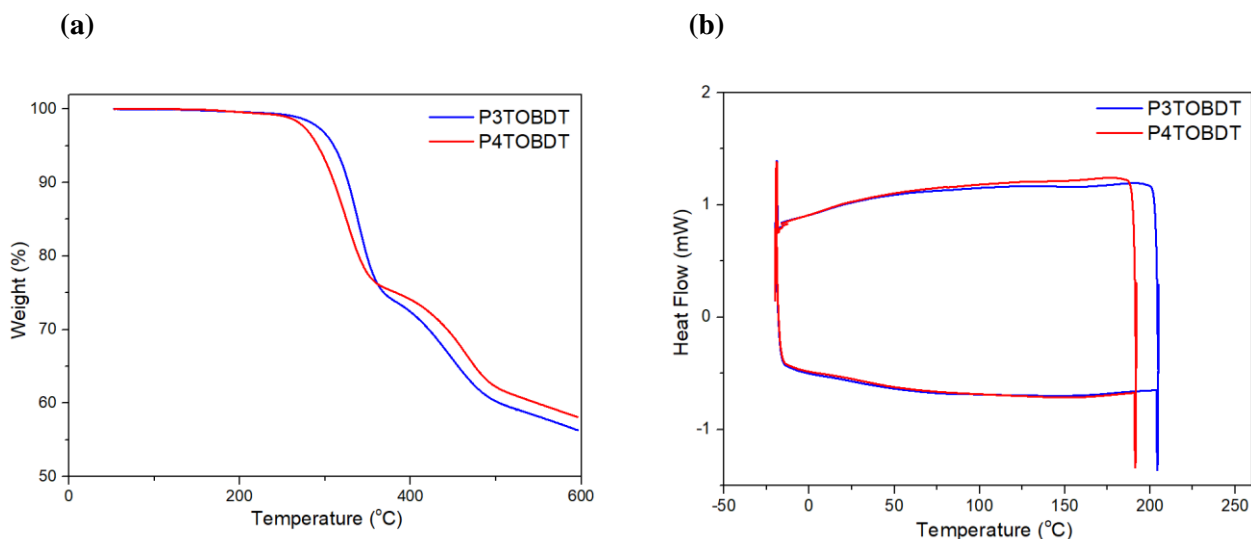
**Figure 3-5 (a)** TGA curve and **(b)** DSC curve of P3TOBDT and P4TOBDT

### 3.3.2 Optical and Electrochemical Properties (UV-vis, CV, and PL)

The UV-vis spectroscopy was carried out to characterize the optical properties of polymers in both solution and thin film conditions, shown in **Figure 3-6**. For the solution of polymers in chloroform (green line), P3TOBDT had the absorption maximum wavelength ($\lambda_{max,s}$) at 495 nm, and the value for P4TOBDT was at 489 nm. Both polymers showed ~30 nm red shift of $\lambda_{max}$ from solution to thin film, indicating more ordered packing of the polymer chain in solid state. In the thin film state, as-cast P3TOBDT film had $\lambda_{max,f}$ at 530 nm, and P4TOBDT had $\lambda_{max,f}$ at 528 nm. Both polymers red-shifted 4nm after annealing on hot plate at 200 ºC for 30min. Moreover, as-cast P4TOBDT film showed an obvious shoulder peak at 557 nm, which was enhanced and red-shifted after thermal annealing, while there were no obvious shoulder observed in P3TOBDT. The longer $\lambda_{max,f}$ and broader shoulder peak of P4TOBDT implied it has improved the planarity and extended conjugation backbone after thermal annealing, and obtained a more ordered chain packing than P3TOBDT.

57
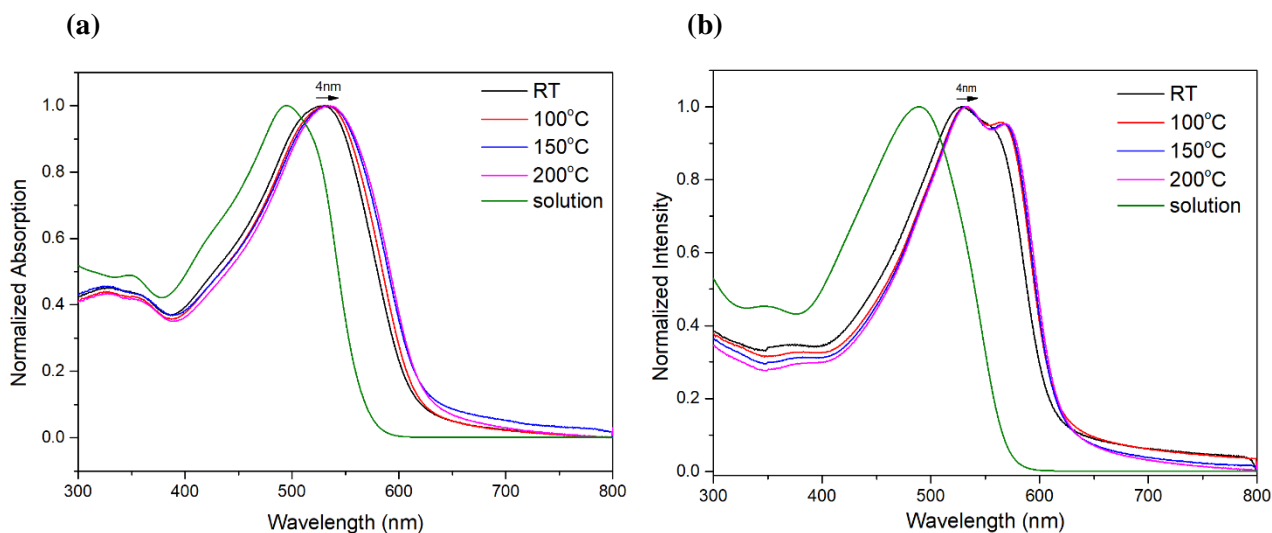
**Figure 3-6** UV-vis absorption spectra of chloroform solution, as-cast thin film, and annealed thin film for polymers **(a)** P3TOBDT and **(b)** P4TOBDT.

The polymer optical bandgap ($E_g^{opt}$) was calculated from as-cast thin film absorption onset wavelength. Two polymers showed same $E_g^{opt}$ of 2.02 eV, which is very close to that of the reported alkyloxime based polymer PBDTTO ($E_g^{opt}$ = 2.03 eV).[60] Thus, P3TOBDT and P4TOBDT exhibit wide bandgap and broad light absorption range which can obtain complementary light absorption with the NFA material Y6 in the 300nm to 900nm solar spectrum, as shown in **Figure 3-7 (a)**.
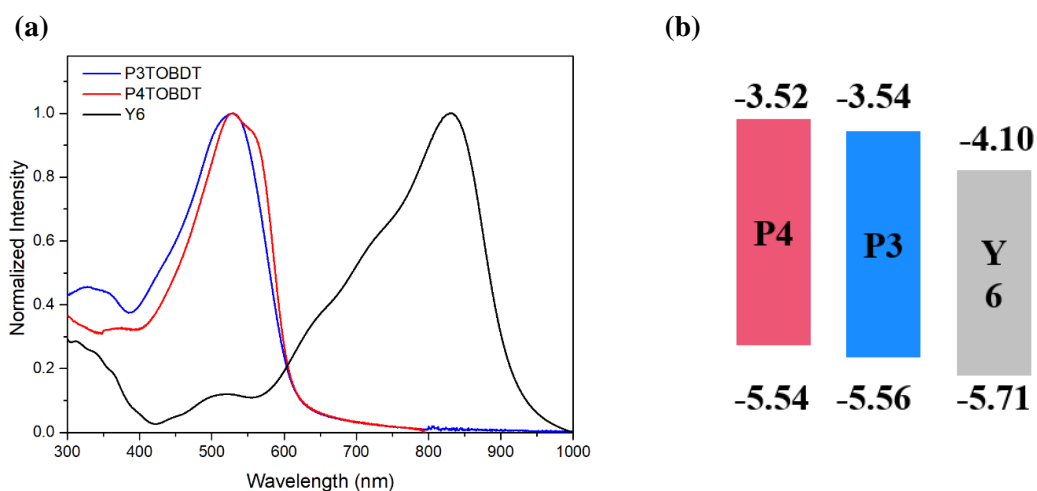


**Figure 3-7 (a)** UV-vis spectra of as-cast thin film P3TOBDT, P4TOBDT, and Y6. **(b)** Energy level alignment of P3TOBDT, P4TOBDT, and Y6.

58

Cyclic voltammetry (CV) was carried out to study the electrochemical properties of the polymers, as shown in **Figure 3-8**. The calculated energy levels along with optical properties of two polymers were summarized in **Table 3-1**. CV was measured with 0.1M [n-Bu4N]+[PF6]- in acetonitrile solution as electrolyte and Ag/AgCl as the reference electrode, at a scan rate of 100 mV/s. The $E_{HOMO}$ of the polymer corresponding to the onset oxidation potential with respect to ferrocene/ferrocenium (Fc/Fc$^+$).[52] The $E_{LUMO}$ was estimated by adding $E_g^{opt}$ and $E_{HOMO}$ together, since no reduction peak can be observed on CV for the three donor polymers. The HOMO and LUMO levels of P3TOBDT were calculated to be -5.56 eV and -3.54 eV. P4TOBDT had a slightly higher HOMO level of -5.54 eV with a LUMO level of -3.52 eV. The energy level differences between two polymers also agreed with DFT simulation results. Compared with the HOMO level of reported alkyloxime based polymers PTOBT ($E_{HOMO}$ = -5.43eV) and PBDTTO ($E_{HOMO}$ = -5.60eV),[54,60] the $E_{HOMO}$ of our polymer P3/4TOBDT lies between them, revealing the structure-property relationship in polymer backbone design. From the energy level alignment of donor polymers and Y6 in **Figure 3-7 (b)**, HOMO energy offset between P3/4TOBDT and Y6 are 0.15 eV and 0.17 eV, respectively. The small $\Delta E_{HOMO}$ between donor polymers and Y6 has been proved to be effective for exciton dissociation and beneficial for reducing the energy loss, which is the special advantage of Y6 while for fullerene acceptors $\Delta E_{HOMO}$ > 0.3eV is required for exciton dissociation.[7] From the **Eq. 1-2** for estimating Voc from energy offsets, larger difference between $E_{HOMO,D}$ and $E_{LUMO,A}$ were helpful to obtain a higher Voc in OSCs. The difference between $E_{HOMO,D}$ and $E_{LUMO,A}$ were 1.46 eV and 1.44 eV for P3TOBDT and P4TOBDT respectively, which would be beneficial to guarantee a high Voc when blending with Y6.
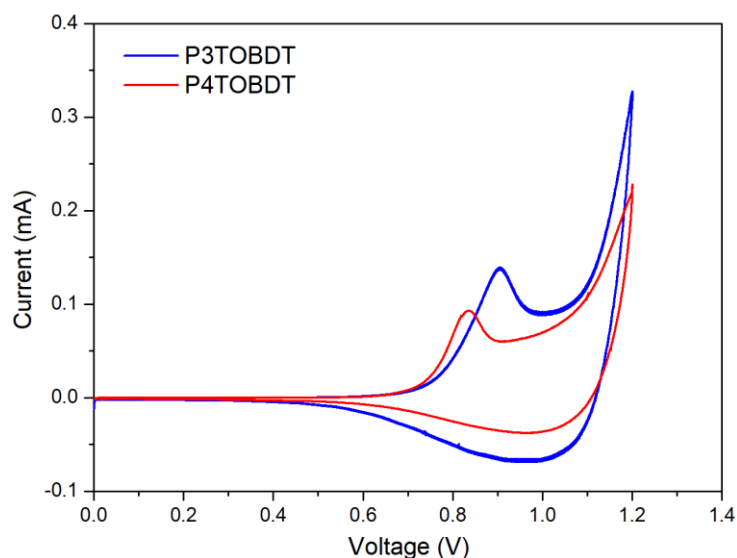
**Figure 3-8** Cyclic voltammetry of polymer films P3TOBDT and P4TOBDT.

**Table 3-1** Optical and electrochemical properties of P3TOBDT and P4TOBDT

| Polymer | $\lambda_{max,s}$ (nm) | $\lambda_{max,f}$ (nm) | $\lambda_{onset}$ (nm) | $E_g{}^{opt}$ (eV) | $E_{HOMO}$ (eV) | $E_{LUMO}$ (eV) |
|---|---|---|---|---|---|---|
| **P3NOBDT** | 495 | 530 | 613 | 2.02 | -5.56 | -3.54 |
| **P4NOBDT** | 489 | 528 | 613 | 2.02 | -5.54 | -3.52 |

The photoluminescence quenching efficiency (PLQE) technique was also carried out to investigate the exciton diffusion and dissociation performance of the donor and acceptor blend films ($W_D$: $W_A$ =1:1) before fabricating OSCs. As shown in **Figure 3-9**, the wavelength 530 nm and 560 nm were used to selectively excited P3TOBDT and P4TOBDT, and Y6 was excited at 800 nm. From the **Figure 3-9 (a, b)**, the PLQE of blend films P3TOBDT:Y6 are 94.9% and 60.5% when comparing to the light emission of neat film P3TOBDT and Y6 respectively. It is obvious that when the dominated absorption raised from donor polymer P3TOBDT, the electron transfer from donor to acceptor is efficient and the emission was quenched, while when the dominated absorption raised from Y6, the hole transfer from acceptor to donor was limited and strong emission peak was detected from the blend film, which could

60

be due to the poor phase separation in the blend film and leading to low Jsc in OSC devices. From the **Figure 3-9 (c, d),** the PLQE of blend film P4TOBDT:Y6 are 97.4% and 97.0% when comparing to the light emission of neat film P4TOBDT and Y6, respectively. The high quenching efficiency of P4TOBDT:Y6 demonstrated efficient exciton diffusion and dissociation in the D-A interphase, and better phase separation than P3TOBDT:Y6 blend film.

**(a)**

**(b)**

**(c)**

**(d)**
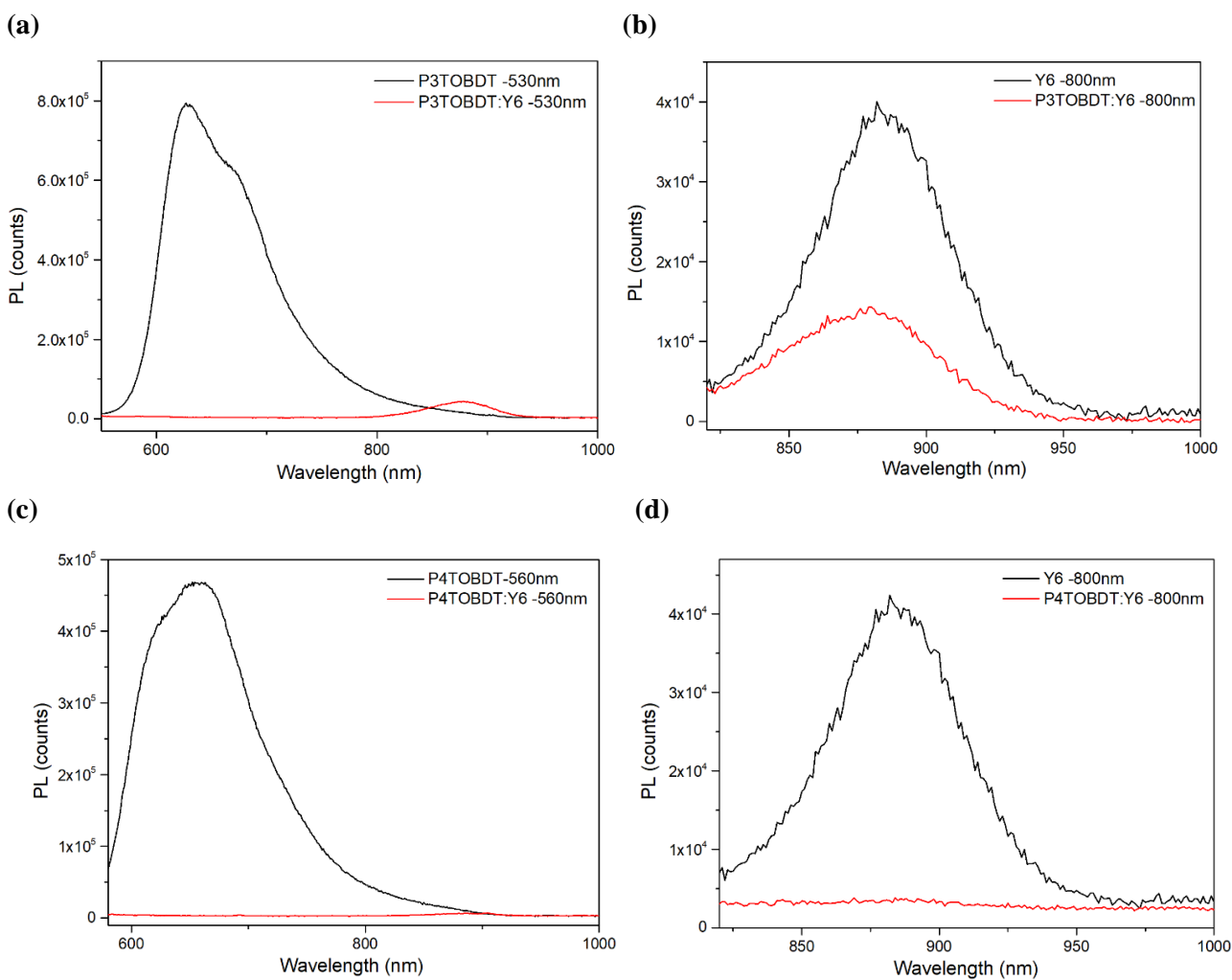
**Figure 3-9** Photoluminescence spectra of **(a)** P3TOBDT neat film and P3TOBDT:Y6 blend film excited at 530 nm, **(b)** Y6 neat film and P3TOBDT:Y6 blend film excited at 800 nm, **(c)** P4TOBDT neat film and P4TOBDT:Y6 blend film excited at 560 nm, **(d)** Y6 neat film and P4TOBDT:Y6 blend film excited at 800 nm.

The molecular orientation of polymer P3TOBDT and P4TOBDT neat films before and after thermal annealing at 150°C were characterized by 2D grazing-incidence X-ray diffraction (2D-GIXD), as shown in **Figure 3-10**. The as-cast P3TOBDT film was amorphous before thermal annealing, no obvious diffraction peaks can be observed. After thermal annealing at 150°C in 10 min, a weak lamellar (100) peak was located at $2\theta = 4.7°$ (d=1.88nm) and a $\pi$–$\pi$ stacking (010) peak was at $2\theta = 20.8°$ (d= 0.43nm) in IP direction, while from OOP direction, a stronger $\pi$–$\pi$ stacking (010) peak was located at $2\theta = 21.8°$ (d= 0.41nm), suggesting that the thermal annealing increased the crystallinity of P3TOBDT forming a preferential face-on orientation. Interestingly, the polymer P4TOBDT exhibited a broad lamellar peak under room temperature at $2\theta = 4.7°$ (d= 1.88nm) in OOP direction but no diffraction peaks after annealing in either IP or OOP direction, indicating the side chain rearrangement after annealing has evanished the edge-on orientation of polymer chains.
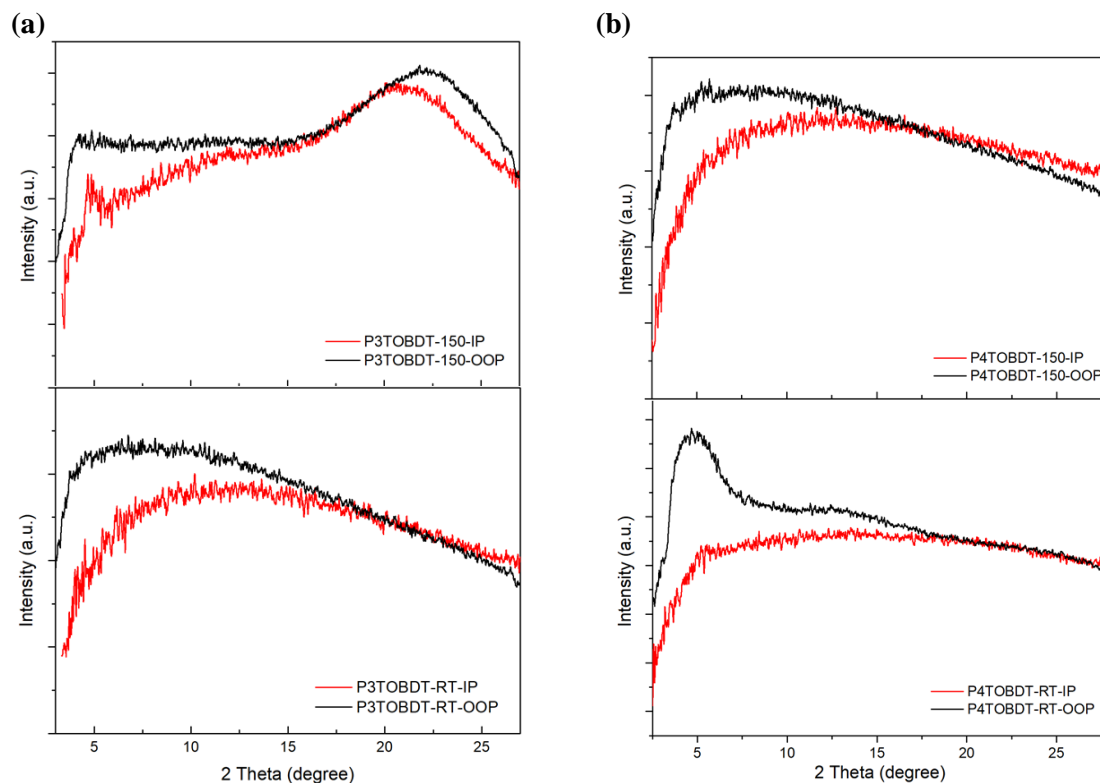


**Figure 3-10** 2D-GIXD spectra of polymer neat films in room temperature and 150°C annealed (a) P3TOBDT (b) P4TOBDT

## 3.4 Organic Solar Cell Performance of Thiophene-Alkyloxime Based Polymers

The two thiophene-alkyloxime based polymers P3TOBDT and P4TOBDT with wide bandgaps and low-lying energy levels are promising donor polymer candidates for OSC devices. The small molecule Y6 as the non-fullerene acceptor was introduced to match with them in NFA OSCs. To investigate the photovoltaic properties of the donor polymers, the inverted configuration of BHJ OSC was applied to fabricate devices, as shown in **Figure 2-11**, with the scheme of ITO/ ZnO/ Active layer/ MoO$_3$/Ag. The details of device fabrication process were written in **Chapter 3.6.2**.

Firstly, the D:A weight ratio 1:1 in chloroform as the active layer solution was applied to both polymers for spin-coating active layer under room temperature without thermal annealing process, and the active layer thickness was optimized to ~105nm by tuning RPM. Then the as-cast active layers P3TOBDT:Y6 and P4TOBDT:Y6 were fabricated to OSCs under same condition for photovoltaic performance comparison between two polymers. P4TOBDT:Y6 showed a much higher PCE of 7.53% (Jsc=18.15mA/cm$^2$, Voc=0.91V, FF=0.45) than P3TOBDT:Y6 with a PCE of 4.27% (Jsc=14.45mA/cm$^2$, Voc=0.89V, FF=0.33). The lower Jsc and FF results of P3TOBDT:Y6 were consist with low quenching efficiency and poor phase separation as mentioned in **Figure 3-9 (b)**. Then the optimization to both blend films were carried out, especially on P4TOBDT:Y6, to achieve the best photovoltaic performance. The photovoltaic results were summarized in **Table 3-2** and **Table 3-3** for P3TOBDT and P4TOBDT respectively.

After optimized with solvent and thermal annealing process, the P3TOBDT:Y6 system has achieved the highest PCE of 5.28% (Jsc= 17.29 mA/cm$^2$, Voc= 0.85 V, FF= 0.36) with chlorobenzene as processing solvent and 150 °C annealing for 10min. It is notably that the FF was significantly increased by changing the processing solvent from chloroform to chlorobenzene, indicating better miscibility of donor and acceptor in blend film. Moreover, as the J-V curve shown in **Figure 3-11**, annealing the

blend film results in an increase of Jsc and decrease of Voc, which demonstrated a more ordered molecular packing of donor polymer with smaller bandgap and enhanced carrier mobility.

**Table 3-2** Summary of OSCs performance based on P3TOBDT:Y6 blend film

| Active layer | Solvent | Temp (°C) | Jsc (mA/cm$^2$) | Voc (V) | FF | PCE (%) | Rs (ohm/cm$^2$) | Rsh (ohm/cm$^2$) |
|---|---|---|---|---|---|---|---|---|
| P3TOBDT:Y6 | CF | RT | 14.45 | 0.89 | 0.33 | 4.27 | 25.92 | 104.59 |
| P3TOBDT:Y6 | CB | RT | 12.85 | 0.92 | 0.36 | 4.31 | 16.53 | 130.53 |
| P3TOBDT:Y6 | CB | 100 | 14.13 | 0.90 | 0.35 | 4.52 | 20.97 | 112.62 |
| P3TOBDT:Y6 | CB | 150 | 17.29 | 0.85 | 0.36 | 5.28 | 20.28 | 104.13 |
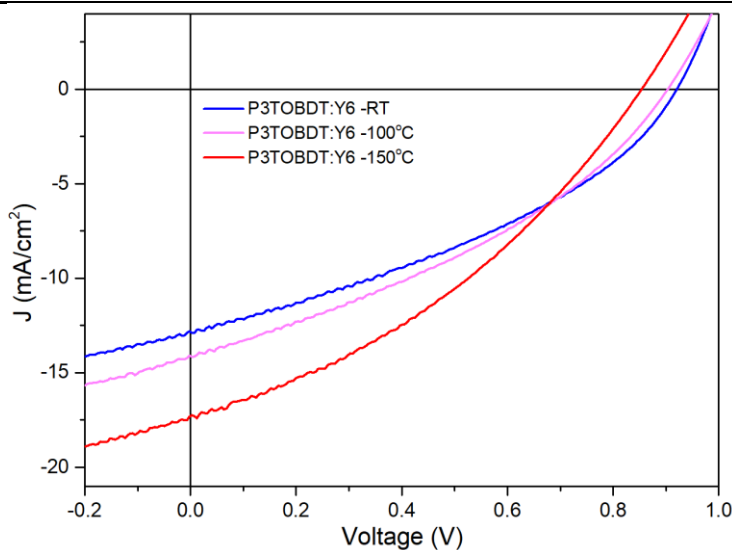


**Figure 3-11** The J-V curve of optimized OSCs based on P3TOBDT:Y6 at different thermal annealing process

For the OSC device based on P4TOBDT:Y6 blend film, it was firstly optimized the D:A weight ratio in the range from 1.2:1, 1:1, to 1:1.2 (**Table 3-3-1**). After the optimum D:A weight ratio was found (1:1), it was carried out to fabricate OSCs for further film morphology improvement due to the low FF in device performance. **Table 3-3-2** showed the influence of processing solvent, annealing temperature,

64

and DIO additive on OSCs performance. The best performance device based on P4TOBDT:Y6 was found to have a PCE of 10.17% (Jsc= 25.95 mA/cm$^2$, Voc= 0.78V, FF= 0.50) under 150 $^o$C thermal annealing and processed with chloroform condition. Comparing to the OSCs based on P3TOBDT:Y6, the P4TOBDT:Y6 showed a higher Jsc and FF due to better quenching efficiency and a more homogeneous morphology in the blend film which will be discussed later. After thermal annealing the blend film from room temperature up to 150 $^o$C, Jsc and FF had significant improvement while Voc dropped 0.13 eV, resulting from the rearrangement of donor and acceptor in the blend film for a more crystalline structure. It is notable that after adding 2.0% DIO as the additive into the P4TOBDT:Y6 blend film solution, the FF had a sharp increase from 0.50 to 0.63, which was obvious on the J-V curve shown in the **Figure 3-12**, the curve became squarer. 1,8-diiodooctance (DIO) is a solvent additive with higher boiling point and lower vapor pressure than chloroform (CF) and chlorobenzene (CB), which has been proved for efficiently controlling the film morphology by extending its drying times and enhancing the crystallinity of polymer donors and NFAs.[61] However, the Voc was decreased after adding 2.0% DIO in blend film, due to DIO will slightly reduce the optical bandgaps of materials and effect voltage loss.[61]

**Table 3-3** Summary of OSCs performance based on P4TOBDT:Y6 blend film

**Table 3-3-1** Donor/Acceptor ratio optimization

| Active layer | D:A Ratio | Solvent | Temp (°C) | Jsc (mA/cm$^2$) | Voc (V) | FF | PCE (%) | Rs (ohm/cm$^2$) | Rsh (ohm/cm$^2$) |
|---|---|---|---|---|---|---|---|---|---|
| **P4TOBDT:Y6** | 1.2:1 | CF | 100 | 18.03 | 0.78 | 0.42 | 5.82 | 10.66 | 144.19 |
| **P4TOBDT:Y6** | 1:1.2 | CF | 100 | 21.68 | 0.84 | 0.44 | 7.96 | 9.18 | 136.30 |
| **P4TOBDT:Y6** | 1:1 | CF | 100 | 21.96 | 0.87 | 0.46 | 8.84 | 7.70 | 142.43 |

**Table 3-3-2** Film morphology optimization (solvent, thermal annealing, additive)

| Active layer | Solvent | Temp (°C) | Jsc (mA/cm²) | Voc (V) | FF (%) | PCE (%) | Rs (ohm/cm²) | Rsh (ohm/cm²) |
|---|---|---|---|---|---|---|---|---|
| P4TOBDT:Y6 | CB | RT | 14.98 | 0.76 | 0.57 | 6.46 | 2.00 | 251.80 |
| P4TOBDT:Y6 | CB | 100 | 16.87 | 0.76 | 0.56 | 7.12 | 2.41 | 228.34 |
| P4TOBDT:Y6 | CF | RT | 18.15 | 0.91 | 0.45 | 7.53 | 8.48 | 149.16 |
| P4TOBDT:Y6 | CF | 100 | 21.96 | 0.87 | 0.46 | 8.84 | 7.70 | 142.43 |
| **P4TOBDT:Y6** | **CF** | **150** | **25.95** | **0.78** | **0.50** | **10.17** | **5.05** | **181.51** |
| P4TOBDT:Y6 | CF | 200 | 22.88 | 0.52 | 0.45 | 5.36 | 5.61 | 108.18 |
| P4TOBDT:Y6-2.0% DIO | CF | 150 | 22.03 | 0.70 | 0.63 | 9.75 | 1.69 | 293.84 |
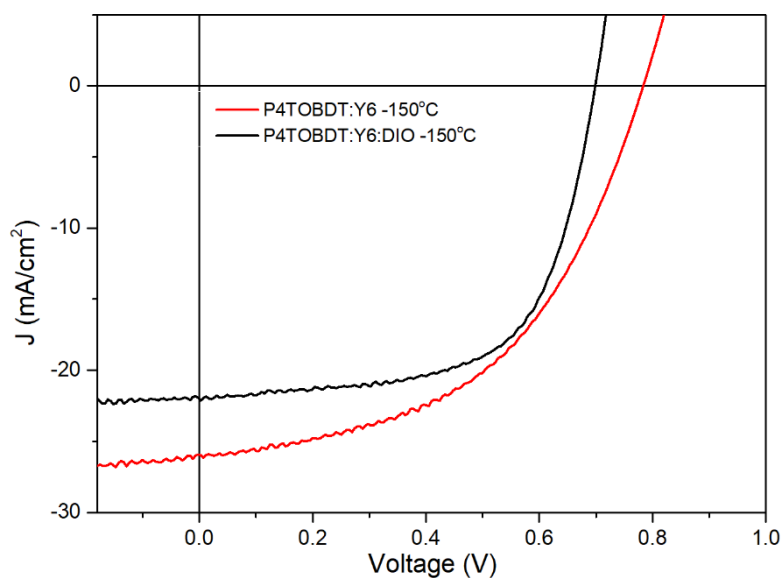


**Figure 3-12** J-V curve of optimized OSCs based on P4TOBDT:Y6 with/without DIO additive under 150 ºC annealing

AFM was applied to the optimized active layers to further investigate the relationship between photovoltaic performance and surface morphology. The height images and phase images of the blend films P3TOBDT:Y6 and P4TOBDT:Y6 from the optimized OSCs were shown in **Figure 3-13**. Both blend films were obtained by spin-coated active layer with processing solvent and thermal annealing under 150°C for 10 min. The processing solvent for P3TOBDT:Y6 is chlorobenzene, and for P4TOBDT:Y6 is chloroform. From the images, the P3TOBDT:Y6 (RMS=1.13) had a smoother and more homogenous surface than P4TOBDT:Y6 (RMS=1.45), which could be due to the better miscibility of P3TOBDT and Y6 in the processing solvent chlorobenzene. The P4TOBDT:Y6 showed a relatively rougher surface with bigger domains comparing to P3TOBDT:Y6. Due to the higher FF and higher SCLC hole mobilities of the P4TOBDT:Y6 devices, the relatively bigger domain size and better continuous interpenetrating networks of P4TOBDT:Y6 blend films are favorable for charge carrier separation and transport. Besides, the RMS of blend film P4TOBDT:Y6-2.0%DIO was also tested as 5.38 nm, indicating that the DIO treatment can significantly improve crystallinity and enlarge phase domains, which is beneficial for increasing FF in OSC performance.
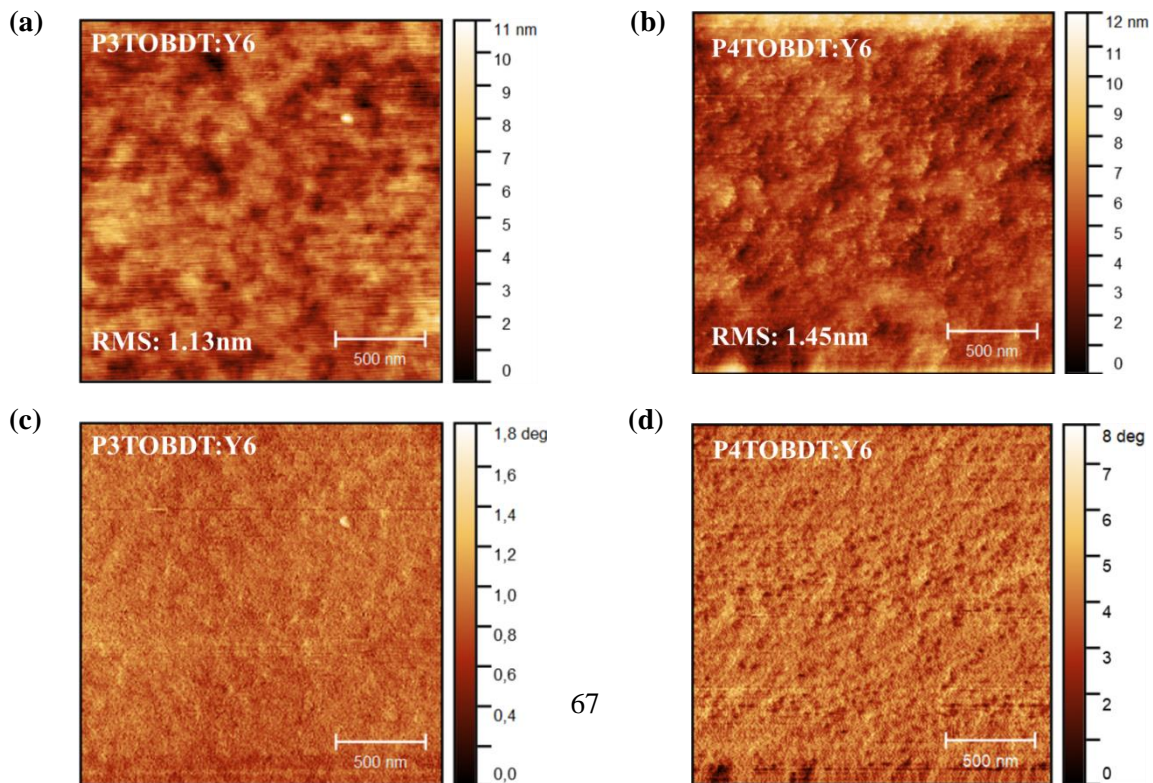
**Figure 3-13** AFM height images of optimized blend films of **(a)** P3TOBDT:Y6, **(b)** P4TOBDT:Y6, and phase images of **(c)** P3TOBDT:Y6, **(d)** P4TOBDT:Y6.

The 2D-GIXD was also employed to investigate the crystallization of blend films P3TOBDT:Y6 and P4TOBDT:Y6 after thermal annealing 150ºC for 10 min (**Figure 3-14**). Interestingly, although high PCE was achieved by P4TOBDT:Y6 based OSCs, no obvious diffraction peaks were observed in IP or OOP direction, indicating that both polymers were packing disordered when blending with Y6 even after thermal annealing.
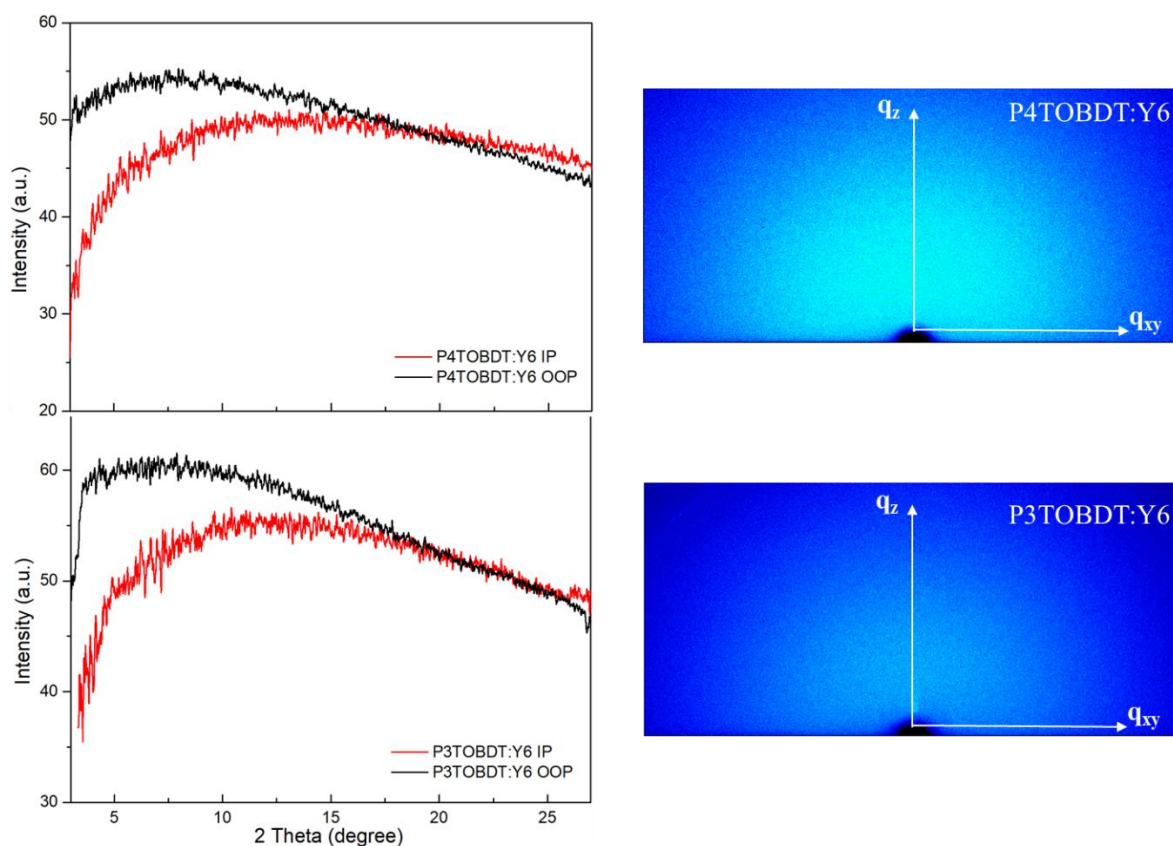


**Figure 3-14** GIXD plots and images of blend films P3TOBDT:Y6 and P4TOBDT:Y6 after thermal annealing 150 ºC

SCLC measurement were carried out for understanding the charge transport in polymer neat films and D:A blend films using the similar calculation method mentioned in Chapter 2.4. The hole-only device was fabricated in the configuration of ITO/ PEDOT:PSS/ active layer/MoO$_3$/Ag, and the electron-only device consists of ITO/ZnO/ active layer/LiF/Al. The SCLC mobilities were summarized in **Table 3-4**, and J$^{1/2}$-V curves of hole-only and electron-only devices were shown in **Figure 3-15**. The hole mobilities of P3TOBDT and P4TOBDT neat films are 1.97 ×10$^{-4}$ cm$^2$V$^{-1}$s$^{-1}$ and 1.08 ×10$^{-4}$ cm$^2$V$^{-1}$s$^{-1}$, respectively. The higher SCLC hole mobility of P3TOBDT than P4TOBDT is consisting with 2D-GIXD results, which showed an enhanced crystallinity and face-on orientation tendency of P3TOBDT neat film after 150$^o$C annealing. Besides, a high molecular weight of P3TOBDT ($M_n$ = 60.6 kDa) may also contribute to high hole mobility in polymer. [60]

After blending with Y6, the hole mobilities of two blend films changed greatly comparing to the value of their neat films: the P3TOBDT:Y6 had a decreased $\mu_h$ of 0.57×10$^{-4}$ cm$^2$V$^{-1}$s$^{-1}$, which should be due to high miscibility of D:A blend film leading to unconnected network of domains, while P4TOBDT:Y6 has an increased $\mu_h$ of 1.15×10$^{-4}$ cm$^2$V$^{-1}$s$^{-1}$, which means it has a better donor phase separation, consisting with AFM phase image. However, both systems showed extremely low electron mobilities with one order of magnitude lower than their hole mobilities, leading to unbalanced $\mu_h/\mu_e$ ratio and which could be the main reason of low FF in the OSCs. The reported electron mobilities of Y6 neat film were 2.35×10$^{-4}$ cm$^2$V$^{-1}$s$^{-1}$ under room temperature and 1.48×10$^{-3}$ cm$^2$V$^{-1}$s$^{-1}$ after annealing under 150$^o$C.[27] The low $\mu_e$ and low crystallinity of blend film suggesting that phase of acceptor Y6 may be too small to form a interconnecting network in the blend films, especially in P3TOBDT:Y6, which may due to their good solubility in chlorobenzene processing solvent. Thus, the further improvement can be focus on film morphology through improving the crystallinity and domain size of acceptor in the blend film by increasing the acceptor weight ratio to enlarge the acceptor phase and balance the $\mu_h/\mu_e$.

**Table 3-4** SCLC mobilities of donor neat films and D:A blend films

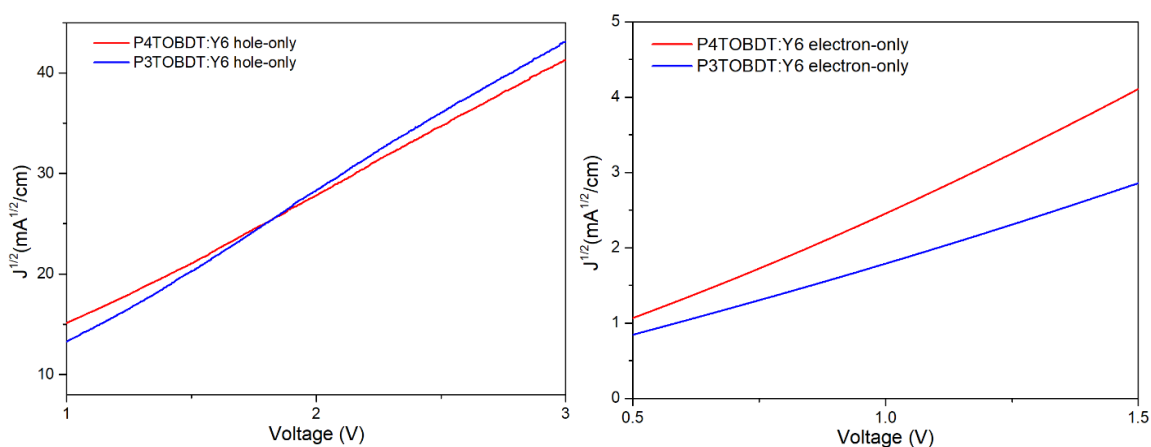| Active layer | P3TOBDT | P4TOBDT | P3TOBDT:Y6 | P4TOBDT:Y6 |
|---|---|---|---|---|
| $\mu_h$ ($\times 10^{-4}$ cm$^2$V$^{-1}$s$^{-1}$) | 1.97 | 1.08 | 0.57 | 1.15 |
| $\mu_e$ ($\times 10^{-5}$ cm$^2$V$^{-1}$s$^{-1}$) | / | / | 0.14 | 0.30 |



**Figure 3-15** $J^{1/2}$-V curves of hole-only and electron-only devices based on P3TOBDT:Y6 and P4TOBDT:Y6
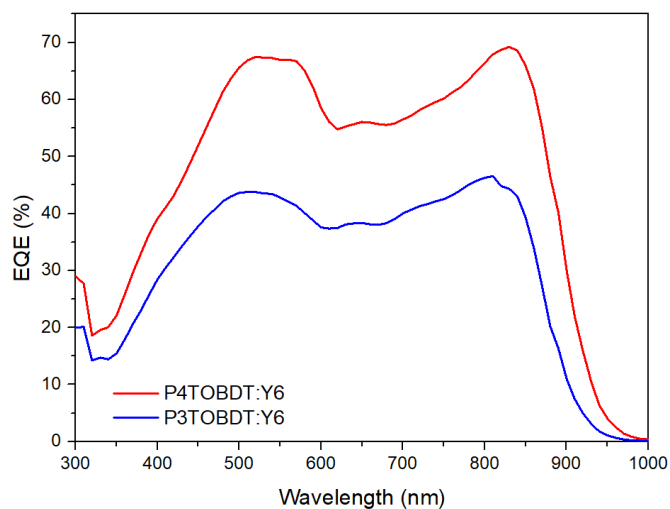


**Figure 3-16** External quantum efficiency (EQE) curves of optimized OSCs based on P3TOBDT:Y6 and P4TOBDT:Y6

70

The external quantum efficiencies (EQE) the ratio of the number of charge carriers generated in solar cell to the number of photons shining on the solar cell, which is applied to study the photocurrent generation efficiency under different wavelength. The EQE spectrum for two best OSCs based on P3TOBDT:Y6 and P4TOBDT:Y6 were shown in **Figure 3-16**. P3TOBDT:Y6 exhibited low EQE with the highest value of 46% at the wavelength of 810 nm, which could be attributed to excessive miscible blend film morphology. P4TOBDT:Y6 exhibited higher EQE values above 55% in the wavelength range of 460 nm to 860 nm, with the highest value of 69% at 803nm which is the $\lambda_{max}$ of Y6. Comparing to the previous reported system PBDTTO:Y6 who owns the highest EQE up to 85%, the blend films P3/4TOBDT:Y6 showed relatively low EQE, due to the imbalanced charge carrier mobility.

### 3.5 Summary and Future Directions

In summary, two novel donor polymers based on BDT-terthiophene backbone with alkyloxime side chains substituted on spacing thiophenes were designed and synthesized. Both polymers demonstrated wide optical bandgaps and low-lying HOMO energy levels, which can obtain the complementary light absorption spectra and large Voc when blending with acceptor material Y6. The P3TOBDT:Y6 based OSC has achieved the PCE of 5.28%, and P4TOBDT:Y6 based device reached a PCE of 10.17% with the best Jsc of 25.95 mA/cm$^2$. According to the two alkyloxime based polymers reported by our group PTOBT and PBDTTO, the P3/4TOBDT structures were designed for a balanced crystallinity in between, to achieve efficient charge transport in both vertical and horizontal direction on substrate. After 150°C thermal annealing of polymer neat film, both polymers showed high SCLC hole mobility up to $10^{-4}$ cm$^2$V$^{-1}$s$^{-1}$, and P3TOBDT exhibited a face-on orientation with higher $\mu_h$ than P4TOBDT, indicating P3TOBDT had higher crystallinity. After blending with Y6, both blend films were amorphous with no obvious diffraction peaks. The P3TOBDT:Y6 blend film showed a homogenous surface and small domain size, with a reduced SCLC hole mobility and one order of magnitude lower

electron mobility, which could be caused by the excessive high solubility of materials in chlorobenzene processing solvent. The P4TOBDT:Y6 system exhibited rougher surface with bigger domain size, with a high SCLC high hole mobility and low electron mobility, indicating the interconnected domains of polymer but unconnected domains of Y6 in blend film.

For future direction, the film morphology of the D:A blend films should be further improved by increasing the crystallinity and domain size of acceptor. It might be helpful to adjust the D:A weight ratio from 1:1 to 1:2 to enlarge the acceptor phase and increase the electron mobility. Also, looking for other NFA acceptors for better matching with two polymers. Additionally, donor polymer structure design is another direction to explore better polymer matching with Y6. It is reported that the introduction of fluorinated benzodithiophene (BDT-F) on the donor polymer can not only decrease the polymer $E_{HOMO}$, but also increase the carrier mobilities, stronger the crystallinity, and smooth the surface.[30,62] Besides, shorten the long alkyl side chain can reduce steric effect, resulting in better planarity and higher carrier mobilities.[63] Thus, a new alkyloxime based polymer structure can be designed by replacing the BDT backbone with BDT-F on P3/4TOBDT and shorten the alkyl side chain from eight carbon atoms to six carbon atoms. This novel polymer with lower $E_{HOMO}$ and higher crystallinity might be effective for improving the blend film morphology and achieving better FF and PCE.

## 3.6 Experimental Section

### 3.6.1 Materials and Characterization

All the solvents and chemical materials were obtained commercially and utilized without further purification. The DFT simulation, TGA and DSC measurement, UV-vis and PL spectra, cyclic voltammetry, and NMR data were obtained using the same conditions as illustrate in Chapter 2.6.1.

### 3.6.2 OSC and SCLC Devices Fabrication and Characterization

The fabrication and characterization of OSCs and SCLC were same as the procedures in Chapter 2.6.2.

### 3.6.3 Synthesis Routes

**Synthesis of 2-bromothiophene-3-carbaldehyde (1a)**
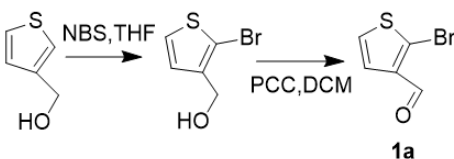


Step1: Thiophen-3-ylmethanol (1.79g,1eq.) were dissolved in THF (25mL), add NBS (2.79g, 1eq.) at 0°C in H2O (5ml), then stirred under room temperature overnight. Stop reaction and remove the solvents, then extract the mixture with brine and ethyl acetate. The crude product was purified by column chromatography using the eluent of ethyl acetate: hexane =1:8→1:2. (2-bromothiophen-3-yl)methanol was obtained as orange oil. (Yield: 1.50g, 50%) 1H NMR (300 MHz, CDCl3, $\delta$/ppm): 7.29 (d, J=6Hz, 1H), 7.06 (d, J=6Hz, 1H), 4.67 (d, J=6Hz, 2H).

Step2: (2-bromothiophen-3-yl)methanol (0.617g, 1eq.) and DCM (13mL) were added into a flask under room temperature. Stirring and adding Pyridinium chlorochromate (0.826g, 1.2eq.) in one portion. After room temperature reacting overnight, the reaction was quenched with DI water and filtered to get rid of insoluble black solid. Then the mixture was extracted with DCM and DI water and the organic

phase was dried with Na2SO4. Crude product was dark brown oil, which was purified by column chromatography using ethyl acetate: hexane= 1:7→1:3 to obtain the first spot as orange oil. (Yield: 0.56g, 92%) 1H NMR (300 MHz, CDCl3, δ/ppm): 9.97 (s, 1H), 7.40 (d, J=6Hz, 1H), 7.32 (m, J=6Hz, 1H)

**Synthesis of 5-bromothiophene-3-carbaldehyde (1b)**



**1b**
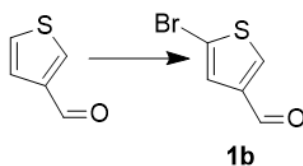
Thiophene-3-carbaldehyde (1.5g, 1.0eq.) was dissolved in dry DCM (25mL) in a flask, add AlCl3 (2.5eq.) at 0 °C and stir for 10min. Then the solution of Br2 (0.8ml, 1.1eq.) in DCM (25mL) was added dropwise at 0°C over 30min.[64] The mixture was heated to 40°C and stirred for 2h. Room temperature reaction overnight. The mixture was transparent and orange. After 20h reaction, the reaction was quenched by ice water and extracted with DCM. The crude product was further purified by column chromatography to obtain the 3rd spot as orange oil. (Yield: 1.65g, 65%) 1H NMR (300 MHz, CDCl3, δ/ppm): 9.79 (s, 1H), 8.02 (d, J=3Hz, 1H), 7.53 (d, J=3Hz, 1H).

**Synthesis of (Z)-2-bromothiophene-3-carbaldehyde oxime (2a)**



**2a**
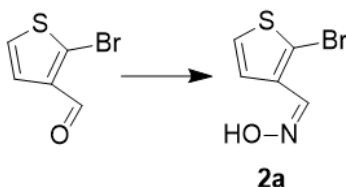
2-bromothiophene-3-carbaldehyde (0.51g, 1.0eq.), K2CO3 (2.58g, 7.0eq.) and EtOH/H2O (14ml) were added to a flask, stirring for 15min under 50°C. Then NH2OH-HCl (1.59g, 8.6eq.) was added in several portions. Heating to 90°C and stirring for 2h. The mixture was extracted with DCM/H2O after cooling down to room temperature and the organic phase was dried with Na2SO4. The product was obtained

74

after removing the solvent as yellow solid. (Yield: 0.53g, 98%) 1H NMR (300 MHz, DMSO, δ/ppm): 11.47 (s, 1H), 8.01 (s, 1H), 7.76 (d, J=6Hz, 1H), 7.25 (d, J=6Hz, 1H).

**Synthesis of (Z)-5-bromothiophene-3-carbaldehyde oxime (2b)**



**2b**
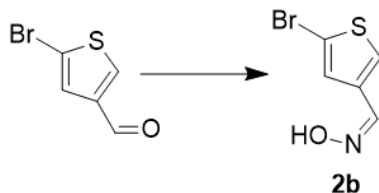
5-bromothiophene-3-carbaldehyde (1.0g, 1.0eq.), $K_2CO_3$ (5.06g, 7.0eq.) and EtOH/H2O were added to a flask, stirring for 15min under 50°C. Then $NH_2OH$-HCl (3.13g, 8.6eq.) was added in several portions. Heating to 90°C and stirring for 2h. The mixture was extracted with DCM/H2O after cooling down to room temperature and the organic phase was dried with Na2SO4. The product was obtained after removing the solvent as white solid. (Yield: 1.03g, 95.5%) 1H NMR (300 MHz, CDCl3, δ/ppm): 8.06 (s, 1H), 7.38 (d, J=1.2Hz, 1H), 7.34 (d, J=1.2Hz, 1H), 7.08 (s, 1H).

**Synthesis of (Z)-2-bromothiophene-3-carbaldehyde O-(2-ethylhexyl) oxime (3a)**



**2a**          **3a**
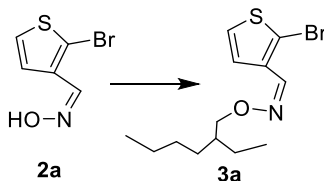
(Z)-2-bromothiophene-3-carbaldehyde oxime (0.53g,1.0eq.), C8H17Br (0.596g, 1.2eq.) and DMF (27ml) were added into a flask under room temperature. Stirring and obtaining transparent yellow solution. Then K2CO3 (0.71g, 2.0eq.) was added in one portion. The reaction was stirred overnight under room temperature. After 48h, the reaction was quenched with DI water, and extracted with DCM. Then the organic phase was dried with $Na_2SO_4$, and solvent was removed under vacuum. The crude product was further purified by column chromatography using ethyl acetate: hexane= 0:1→1:8 to obtain the expected product. (Yield: 0.44g, 53.3%) 1H NMR (300 MHz, CDCl3, δ/ppm): 8.14 (s, 1H),

7.32 (d, J=6Hz, 1H), 7.26 (d, J=6Hz, 1H), 4.10 (d, J=6Hz, 2H), 1.70 (m, 1H), 1.44 (m, 8H), 0.96 (m, 6H).

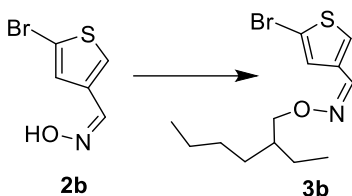**Synthesis of (Z)-5-bromothiophene-3-carbaldehyde O-(2-ethylhexyl) oxime (3b)**



(Z)-5-bromothiophene-3-carbaldehyde oxime (0.5g,1.0eq.), $C_8H_{17}Br$ (0.56g, 1.2eq.) and DMF (27ml) were added into a flask under room temperature. Stirring and obtaining transparent yellow solution. Then $K_2CO_3$ (0.67g, 2.0eq.) was added in one portion. The reaction was stirred overnight under room temperature. After 72h, the reaction was quenched with saturated $NaHCO_3$, and extracted with DCM and DI water. Then the organic phase was dried with Na2SO4, and solvent was removed under vacuum. The crude product was further purified by column chromatography using ethyl acetate: hexane= 1:8→1:4 to obtain the expected product (containing 12% E-type isomer). (Yield: 0.261g, 34%) 1H NMR (300 MHz, CDCl3, δ/ppm): 7.98 (s, 1H), 7.39 (d, J=3Hz, 1H), 7.25 (d, J=3Hz, 1H), 4.04 (d, J=6Hz, 2H), 1.70 (m, 1H), 1.44 (m, 8H), 0.96 (m, 6H).

**Synthesis of (1Z,1'Z)-[2,2':5',2''-terthiophene]-3,3''-dicarbaldehyde O,O-dioctyl dioxime (4a)**
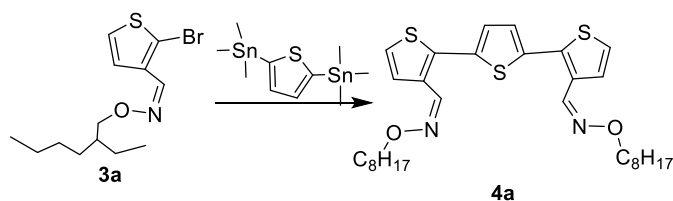


**3a** (0.34g, 2.1eq.), 2,5-bis(trimethylstannyl)thiophene (0.208g, 1.0eq.), tri(o-tolyl)phosphine (P(o-tol)₃) (12.4mg, 0.08eq.), and tris(dibenzylideneacetone)dipalladium (Pd₂(dba)₃) (9.3mg, 0.02eq.), and anhydrous toluene (9ml) were added to a two-necked round bottom flask. The reaction device was deoxygenated with argon for three times and then the mixture reacted at 100°C under argon. After 24h

reaction at 100°C, the solution is transparent and yellow. After cooling down to room temperature, the reaction was quenched with DI water, and extracted with DCM and H2O. T Then the organic phase was dried with Na2SO4, and solvent was removed under vacuum. The crude product was further purified by column chromatography using DCM: hexane= 1:8→1:1 to obtain the expected product as orange oil. (Yield: 0.22g, 77%) 1H NMR (300 MHz, CDCl3, δ/ppm): 8.35 (s, 2H), 7.50 (d, J=6Hz, 2H), 7.26 (d, J=3Hz, 2H), 7.12 (s, 2H), 4.10 (d, J=6Hz, 4H), 1.71 (m, 2H), 1.34 (m, 16H), 0.94 (m, 12H).
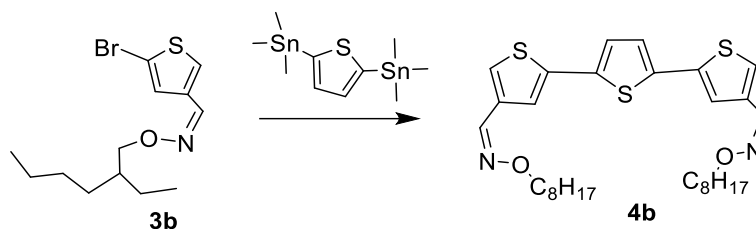
**Synthesis of (1Z,1'Z)-[2,2':5',2''-terthiophene]-4,4''-dicarbaldehyde O,O-dioctyl dioxime (4b)**



**3b** (0.203g, 2.1eq.), 2,5-bis(trimethylstannyl)thiophene (0.124g, 1.0eq.), tri(o-tolyl)phosphine (P(o-tol)$_3$) (7.37mg, 0.08eq.), and tris(dibenzylideneacetone)dipalladium (Pd$_2$(dba)$_3$) (5.54mg, 0.02eq.), and anhydrous toluene (7ml) were added to a two-necked round bottom flask. The reaction device was deoxygenated with argon for three times and then the mixture reacted at 100°C under argon. After 24h reaction at 100°C, the solution is transparent and yellow. After cooling down to room temperature, the reaction was quenched with DI water, and extracted with DCM and H2O. T Then the organic phase was dried with Na2SO4, and solvent was removed under vacuum. The crude product was further purified by column chromatography using DCM: hexane= 1:8→1:1 to obtain the expected product as orange oil. (Yield: 0.12g, 71%) 1H NMR (300 MHz, CDCl3, δ/ppm): 8.07 (s, 2H), 7.52 (d, J=6Hz, 2H), 7.30 (d, J=3Hz, 2H), 7.13 (m, 2H), 4.10 (d, J=6Hz, 4H), 1.72 (m, 2H), 1.35 (m, 16H), 0.95 (m, 12H).

**Synthesis of (1Z,1'Z)-5,5''-dibromo-[2,2':5',2''-terthiophene]-3,3''-dicarbaldehyde O,O-dioctyl dioxime (M3)**
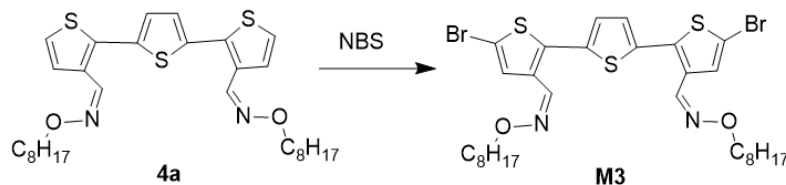


**4a** (0.22g, 1.0eq.) was dissolved in dry DMF (10ml) in a flask, then NBS (0.147g, 2.1eq.) was added drop wisely under 0°C. The reaction mixture was kept stirred overnight in the dark at room temperature. After 24h reaction, the solution changed color from yellow to orange. The mixture was extracted with DCM and DI water, and the organic phase was dried with anhydrous Na2SO4. The crude product was purified by column chromatography with eluent of DCM: Hex=1:8→1:4, obtaining the 2nd spot as the expected product, which is yellow oil. (Yield: 220mg, 78%) 1H NMR (300 MHz, CDCl3, δ/ppm): 8.28 (s, 2H), 7.47 (s, 2H), 7.08 (s, 2H), 4.09 (d, J=6Hz, 4H), 1.69 (m, 2H), 1.33 (m, 16H), 0.93 (m, 12H).

**Synthesis of (1Z,1'Z)-5,5''-dibromo-[2,2':5',2''-terthiophene]-4,4''-dicarbaldehyde O,O-dioctyl dioxime (M4)**
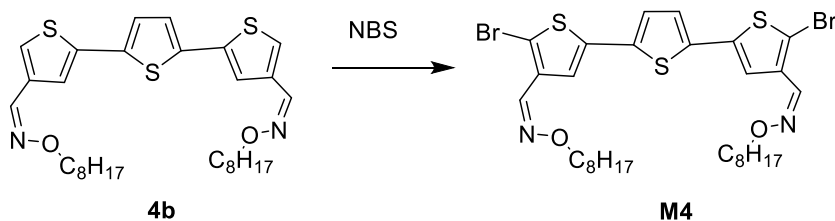


**4b** (0.114g, 1.0eq.) was dissolved in dry DMF (10ml) in a flask, then NBS (0.076g, 2.1eq.) was added drop wisely under 0°C. The reaction mixture was kept stirred overnight in the dark at room temperature. After 24h reaction, the solution changed color from yellow to orange. The mixture was extracted with DCM and DI water, and the organic phase was dried with anhydrous Na2SO4. The crude product was purified by column chromatography with eluent of DCM: Hex=1:10→1:2, obtaining the 2nd spot as the expected product, which is yellow oil. (Yield: 80mg, 55%) 1H NMR (300 MHz, CDCl3, δ/ppm):

8.10 (s, 2H), 7.36 (s, 2H), 7.07 (s, 2H), 4.12 (d, J=6Hz, 4H), 1.72 (m, 2H), 1.36 (m, 16H), 0.95 (m, 12H).

**Synthesis of polymer P3TOBDT**
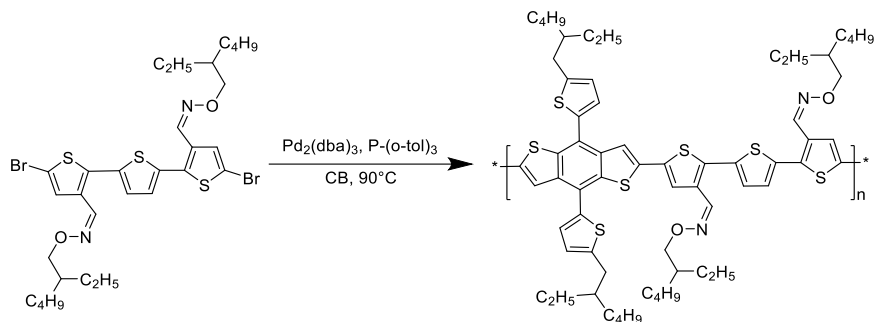


The monomer M3 (0.063g,1.0eq), BDT (0.079g, 1.0eq), P(o-tol)3 (2.13mg, 0.08eq),  Pd2(dba)3 (1.60mg, 0.02eq), and  anhydrous chlorobenzene (3.70ml) were added to a two-necked round bottom flask. The reaction device was deoxygenated with argon for three times and then the mixture reacted overnight at 90°C under nitrogen. After 20h reaction, add 0.3mL DMF into the flask and increase the temperature to 120°C. After another 20h reaction, the solution was viscous and red. The reaction was cooled down to room temperature and poured into 100mL methanol. The red solid precipitate was filtered and purified via Soxhlet extraction with acetone, hexane, and chloroform, respectively. The red-purple films was obtained after removing the chloroform solvent. (Yield: 105mg, 100%)

**Synthesis of polymer P4TOBDT**



79
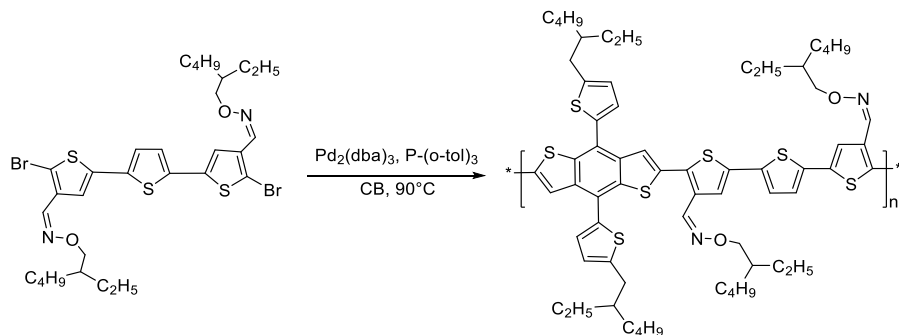
The monomer M4 (0.057g,1.0eq), BDT (0.072g, 1.0eq), P(o-tol)3 (1.94mg, 0.08eq),  Pd2(dba)3 (1.46mg, 0.02eq), and  anhydrous chlorobenzene (3.35ml) were added to a two-necked round bottom flask. The reaction device was deoxygenated with argon for three times and then the mixture reacted overnight at 90°C under nitrogen. After 20h reaction, add 0.3mL DMF into the flask and increase the temperature to 120°C. After another 20h reaction, the solution was viscous and red. The reaction was cooled down to room temperature and poured into 100mL methanol. The red solid precipitate was filtered and purified via Soxhlet extraction with acetone, hexane, and chloroform, respectively. The red-purple films was obtained after removing the chloroform solvent. (Yield: 92.2mg, 100%)

# Chapter 4  Summary and Future Direction

In conclusion, this thesis presents the design and synthesis of a serious BDT based wide bandgap polymers, with ester sidechain or alkyloxime sidechain substituted, function as the electron withdrawing group.  After measuring the optical and electronical properties, the wide bandgap polymers were applied in BHJ organic solar cells as the donor materials blending with non-fullerene acceptors. The devices performance and blend film morphology were also characterized and analyzed.

In Chapter 2, three novel ester-substituted vinyl (TVT-COOR) based donor polymers were designed and synthesized, and among them the polymer PEBDT were demonstrated with planar backbone, suitable energy levels, and high quenching efficiency matching with two NFAs: $(3PS)_2$-SiPc and Y6. For the OSCs results, a PCE of 0.52% based on PEBDT: $(3PS)_2$-SiPc blend film and a PCE of 1.23% based on PEBDT:Y6 blend film were obtained. Although the Jsc was improved from 2.16 mA/cm$^2$ to 7.32 mA/cm$^2$ by introducing Y6 to the blend film, both systems showed low Jsc, large voltage loss and low FF, which was ascribed to poor film morphology with incontinuous network of the blend films. The amorphous property and low carrier mobility of PEBDT could relate to its disordered sidechain packing, so it might be helpful to increase the planarity and rigidity of the backbone structure to achieve a more ordered molecule packing and enhanced charge carrier mobility. Thus, the future work will focus on new polymer structure design by changing the TVT to the fused ring structure, for planar backbone and higher crystallinity.

In Chapter 3, another efficient electron-withdrawing group alkyloxime side chain was introduced, and two novel thiophene-alkyloxime based wide-bandgap donor polymers P3TOBDT and P4TOBDT were designed and synthesized. Both polymers showed low-lying $E_{HOMO}$, broad absorption range, and improved crystallinity comparing to the BDT-alkyloxime based polymer reported before. The P3TOBDT:Y6 based OSC has achieved the PCE of 5.28%, and P4TOBDT:Y6 based device reached a

PCE of 10.17% with the highest Jsc of 25.95 mA/cm$^2$. However, it is found that the electron mobility was much lower than the hole mobility in the blend films, resulting in unbalanced μh/μe ratio and low FF, which was attributed to the excessive high solubility of Y6 in the D:A blend solution and poor interconnecting network of Y6 in the blend film. For the future direction, the film morphology of D:A blend films should be further improved by increasing the crystallinity of Y6, such as adjusting the D:A weight ratio from 1:1 to 1:2 to enlarge the acceptor phase and increase the electron mobility. Additionally, novel polymer structure design based on previous polymers is another strategy to optimize polymer to match with Y6. Replacing the BDT backbone with BDT-F on P3/4TOBDT with shorter alkyl sidechain can lower the $E_{HOMO}$ and increase crystallinity, which might be effective for improving the blend film morphology and achieving better FF and PCE in OSC devices.

# Bibliography

(1)  Extance, A. The Reality behind Solar Power's next Star Material. *Nature* **2019**, *570* (7762), 429–432. https://doi.org/10.1038/d41586-019-01985-y.

(2)  How do solar cells work? http://www.explainthatstuff.com/solarcells.html (accessed 2021 -05 -30).

(3)  The Promise of Organic Solar Cells: Flexible, Cheap, and Printable. *Science in the News*, 2012.

(4)  Best Research-Cell Efficiency Chart https://www.nrel.gov/pv/cell-efficiency.html (accessed 2021 -05 -30).

(5)  Shockley, W.; Queisser, H. J. Detailed Balance Limit of Efficiency of P-n Junction Solar Cells. *Journal of Applied Physics* **1961**, *32* (3), 510–519. https://doi.org/10.1063/1.1736034.

(6)  Dyer-Smith, C.; Nelson, J.; Li, Y. Chapter I-5-B - Organic Solar Cells. In *McEvoy's Handbook of Photovoltaics (Third Edition)*; Kalogirou, S. A., Ed.; Academic Press, 2018; pp 567–597. https://doi.org/10.1016/B978-0-12-809921-6.00015-X.

(7)  He, K.; Kumar, P.; Yuan, Y.; Li, Y. Wide Bandgap Polymer Donors for High Efficiency Non-Fullerene Acceptor Based Organic Solar Cells. *Mater. Adv.* **2021**, *2* (1), 115–145. https://doi.org/10.1039/D0MA00790K.

(8)  Weinberger, B. R.; Akhtar, M.; Gau, S. C. Polyacetylene Photovoltaic Devices. *Synthetic Metals* **1982**, *4* (3), 187–197. https://doi.org/10.1016/0379-6779(82)90012-1.

(9)  Tang, C. W. Two-layer Organic Photovoltaic Cell. *Appl. Phys. Lett.* **1986**, *48* (2), 183–185. https://doi.org/10.1063/1.96937.

(10) Cheng, P.; Li, G.; Zhan, X.; Yang, Y. Next-Generation Organic Photovoltaics Based on Non-Fullerene Acceptors. *Nature Photon* **2018**, *12* (3), 131–142. https://doi.org/10.1038/s41566-018-0104-9.

(11) Mikhnenko, O. V.; Blom, P. W. M.; Nguyen, T.-Q. Exciton Diffusion in Organic Semiconductors. *Energy Environ. Sci.* **2015**, *8* (7), 1867–1888. https://doi.org/10.1039/C5EE00925A.

(12) Lan, Z.-A.; Zhang, G.; Chen, X.; Zhang, Y.; Zhang, K. A. I.; Wang, X. Reducing the Exciton Binding Energy of Donor–Acceptor-Based Conjugated Polymers to Promote Charge-Induced Reactions. *Angewandte Chemie International Edition* **2019**, *58* (30), 10236–10240. https://doi.org/10.1002/anie.201904904.

(13) Menke, S. M.; Ran, N. A.; Bazan, G. C.; Friend, R. H. Understanding Energy Loss in Organic Solar Cells: Toward a New Efficiency Regime. *Joule* **2018**, *2* (1), 25–35. https://doi.org/10.1016/j.joule.2017.09.020.

(14) Qi, B.; Wang, J. Fill Factor in Organic Solar Cells. *Phys. Chem. Chem. Phys.* **2013**, *15* (23), 8972–8982. https://doi.org/10.1039/C3CP51383A.

(15) Mehdizadeh Rad, H.; Zhu, F.; Singh, J. Profiling Exciton Generation and Recombination in Conventional and Inverted Bulk Heterojunction Organic Solar Cells. *Journal of Applied Physics* **2018**, *124* (8), 083103. https://doi.org/10.1063/1.5031062.

(16) Gusain, A.; Faria, R. M.; Miranda, P. B. Polymer Solar Cells—Interfacial Processes Related to Performance Issues. *Frontiers in Chemistry* **2019**, *7*, 61. https://doi.org/10.3389/fchem.2019.00061.

(17) Chen, Z.; Li, W.; Li, R.; Zhang, Y.; Xu, G.; Cheng, H. Fabrication of Highly Transparent and Conductive Indium–Tin Oxide Thin Films with a High Figure of Merit via Solution Processing. *Langmuir* **2013**, *29* (45), 13836–13842. https://doi.org/10.1021/la4033282.

(18) Park, Y.; Berger, J.; Tang, Z.; Müller-Meskamp, L.; Lasagni, A. F.; Vandewal, K.; Leo, K. Flexible, Light Trapping Substrates for Organic Photovoltaics. *Appl. Phys. Lett.* **2016**, *109* (9), 093301. https://doi.org/10.1063/1.4962206.

(19) Xu, H.; Yuan, F.; Zhou, D.; Liao, X.; Chen, L.; Chen, Y. Hole Transport Layers for Organic Solar Cells: Recent Progress and Prospects. *J. Mater. Chem. A* **2020**, *8* (23), 11478–11492. https://doi.org/10.1039/D0TA03511D.

(20) Zheng, S.; Wang, G.; Liu, T.; Lou, L.; Xiao, S.; Yang, S. Materials and Structures for the Electron Transport Layer of Efficient and Stable Perovskite Solar Cells. *Sci. China Chem.* **2019**, *62* (7), 800–809. https://doi.org/10.1007/s11426-019-9469-1.

(21) Liu, X.; Guo, L. J.; Zheng, Y. 5-Nm LiF as an Efficient Cathode Buffer Layer in Polymer Solar Cells Through Simply Introducing a C60 Interlayer. *Nanoscale Research Letters* **2017**, *12* (1), 543. https://doi.org/10.1186/s11671-017-2299-y.

(22) Speller, E. M.; Clarke, A. J.; Luke, J.; Lee, H. K. H.; Durrant, J. R.; Li, N.; Wang, T.; Wong, H. C.; Kim, J.-S.; Tsoi, W. C.; Li, Z. From Fullerene Acceptors to Non-Fullerene Acceptors: Prospects and Challenges in the Stability of Organic Solar Cells. *J. Mater. Chem. A* **2019**, *7* (41), 23361–23377. https://doi.org/10.1039/C9TA05235F.

(23) Ganesamoorthy, R.; Sathiyan, G.; Sakthivel, P. Review: Fullerene Based Acceptors for Efficient Bulk Heterojunction Organic Solar Cell Applications. *Solar Energy Materials and Solar Cells* **2017**, *161*, 102–148. https://doi.org/10.1016/j.solmat.2016.11.024.

(24) Bernardo, G.; Melle-Franco, M.; Washington, A. L.; Dalgliesh, R. M.; Li, F.; Mendes, A.; Parnell, S. R. Different Agglomeration Properties of PC61BM and PC71BM in Photovoltaic Inks – a Spin-Echo SANS Study. *RSC Adv.* **2020**, *10* (8), 4512–4520. https://doi.org/10.1039/C9RA08019H.

(25) Lin, Y.; Wang, J.; Zhang, Z.-G.; Bai, H.; Li, Y.; Zhu, D.; Zhan, X. An Electron Acceptor Challenging Fullerenes for Efficient Polymer Solar Cells. *Advanced Materials* **2015**, *27* (7), 1170–1174. https://doi.org/10.1002/adma.201404317.

(26) Xu, W.; Gao, F. The Progress and Prospects of Non-Fullerene Acceptors in Ternary Blend Organic Solar Cells. *Materials Horizons* **2018**, *5* (2), 206–221. https://doi.org/10.1039/C7MH00958E.

(27) Yuan, J.; Zhang, Y.; Zhou, L.; Zhang, G.; Yip, H.-L.; Lau, T.-K.; Lu, X.; Zhu, C.; Peng, H.; Johnson, P. A.; Leclerc, M.; Cao, Y.; Ulanski, J.; Li, Y.; Zou, Y. Single-Junction Organic Solar Cell with over 15% Efficiency Using Fused-Ring Acceptor with Electron-Deficient Core. *Joule* **2019**, *3* (4), 1140–1151. https://doi.org/10.1016/j.joule.2019.01.004.

(28) Zhao, J.; Yao, C.; Ali, M. U.; Miao, J.; Meng, H. Recent Advances in High-Performance Organic Solar Cells Enabled by Acceptor–Donor–Acceptor–Donor–Acceptor (A–DA′D–A) Type Acceptors. *Mater. Chem. Front.* **2020**, *4* (12), 3487–3504. https://doi.org/10.1039/D0QM00305K.

(29) Li, G.; Shrotriya, V.; Huang, J.; Yao, Y.; Moriarty, T.; Emery, K.; Yang, Y. High-Efficiency Solution Processable Polymer Photovoltaic Cells by Self-Organization of Polymer Blends. *Nature Mater* **2005**, *4* (11), 864–868. https://doi.org/10.1038/nmat1500.

(30) Qiu, D.; Adil, M. A.; Lu, K.; Wei, Z. The Crystallinity Control of Polymer Donor Materials for High-Performance Organic Solar Cells. *Frontiers in Chemistry* **2020**, *8*, 1044. https://doi.org/10.3389/fchem.2020.603134.

(31) Hou, J.; Park, M.-H.; Zhang, S.; Yao, Y.; Chen, L.-M.; Li, J.-H.; Yang, Y. Bandgap and Molecular Energy Level Control of Conjugated Polymer Photovoltaic Materials Based on Benzo[1,2-b:4,5-B′]Dithiophene. *Macromolecules* **2008**, *41* (16), 6012–6018. https://doi.org/10.1021/ma800820r.

(32) Xu, X.; Zhang, G.; Li, Y.; Peng, Q. The Recent Progress of Wide Bandgap Donor Polymers towards Non-Fullerene Organic Solar Cells. *Chinese Chemical Letters* **2019**, *30* (4), 809–825. https://doi.org/10.1016/j.cclet.2019.02.030.

(33) NMR basic knowledge | Nuclear Magnetic Resonance Spectrometer (NMR) | Products | JEOL https://www.jeol.co.jp/en/products/nmr/basics.html (accessed 2021 -08 -08).

(34) Lathe, G. H.; Ruthven, C. R. The Separation of Substances on the Basis of Their Molecular Weights, Using Columns of Starch and Water. *Biochem J* **1955**, *60* (4), xxxiv.

(35) Stepto, R. F. T. Dispersity in Polymer Science (IUPAC Recommendations 2009). *Pure and Applied Chemistry* **2009**, *81* (2), 351–353. https://doi.org/10.1351/PAC-REC-08-05-02.

(36) Ng, H. M.; Saidi, N. M.; Omar, F. S.; Ramesh, K.; Ramesh, S.; Bashir, S. Thermogravimetric Analysis of Polymers. In *Encyclopedia of Polymer Science and Technology*; American Cancer Society, 2018; pp 1–29. https://doi.org/10.1002/0471440264.pst667.

(37) Frederick, W. J.; Mentzer, C. C. Determination of Heats of Volatilization for Polymers by Differential Scanning Calorimetry. *Journal of Applied Polymer Science* **1975**, *19* (7), 1799–1804. https://doi.org/10.1002/app.1975.070190702.

(38) Costa, J. C. S.; Taveira, R. J. S.; Lima, C. F. R. A. C.; Mendes, A.; Santos, L. M. N. B. F. Optical Band Gaps of Organic Semiconductor Materials. *Optical Materials* **2016**, *58*, 51–60. https://doi.org/10.1016/j.optmat.2016.03.041.

(39) Ultraviolet-Visible (UV-Vis) Spectroscopy | Protocol https://www.jove.com/v/10204/ultraviolet-visible-uv-vis-spectroscopy (accessed 2021 -08 -08).

(40) Leonat, L.; Beatrice Gabriela, S.; Brañzoi, I. V. Cyclic Voltammetry for Energy Levels Estimation of Organic Materials. *UPB Scientific Bulletin, Series B: Chemistry and Materials Science* **2013**, *75*, 111–118.

(41) Camacho, R. Polarization Portraits of Light-Harvesting Antennas: From Single Molecule Spectroscopy to Imaging, 2014. https://doi.org/10.13140/2.1.4852.5607.

(42) Chapter 3 - Methods for Assessing Surface Cleanliness. In *Developments in Surface Contamination and Cleaning, Volume 12*; Kohli, R., Mittal, K. L., Eds.; Elsevier, 2019; pp 23–105. https://doi.org/10.1016/B978-0-12-816081-7.00003-6.

(43) Parot, P.; Dufrêne, Y. F.; Hinterdorfer, P.; Le Grimellec, C.; Navajas, D.; Pellequer, J.-L.; Scheuring, S. Past, Present and Future of Atomic Force Microscopy in Life Sciences and Medicine. *J Mol Recognit* **2007**, *20* (6), 418–431. https://doi.org/10.1002/jmr.857.

(44) Nanotechnology - Wikibooks, open books for an open world https://en.wikibooks.org/wiki/Nanotechnology (accessed 2021 -08 -06).

(45) Zhang, M.; Guo, X.; Ma, W.; Ade, H.; Hou, J. A Polythiophene Derivative with Superior Properties for Practical Application in Polymer Solar Cells. *Advanced Materials* **2014**, *26* (33), 5880–5885. https://doi.org/10.1002/adma.201401494.

(46) Park, G. E.; Choi, S.; Park, S. Y.; Lee, D. H.; Cho, M. J.; Choi, D. H. Eco-Friendly Solvent-Processed Fullerene-Free Polymer Solar Cells with over 9.7% Efficiency and Long-Term Performance Stability. *Advanced Energy Materials* **2017**, *7* (19), 1700566. https://doi.org/10.1002/aenm.201700566.

(47) Bi, P.; Ren, J.; Zhang, S.; Wang, J.; Hou, J. PTV-Based p-Type Organic Semiconductors: Candidates for Low-Cost Photovoltaic Donors with Simple Synthetic Routes. *Polymer* **2020**, *209*, 122900. https://doi.org/10.1016/j.polymer.2020.122900.

(48) Yang, Z.; Bao, C.; Zhang, G.; Liu, Z.; Zhu, W.; Cui, S.; Peng, Q.; Liu, Y. Low-Cost Donors Based on a Dicarboxylic Ester Side-Chain Substituted Thieno[3,2b]Thiophene Unit for Efficient Polymer Solar Cells. *Dyes and Pigments* **2020**, *182*, 108698. https://doi.org/10.1016/j.dyepig.2020.108698.

(49) Tang, Y.; Sun, H.; Wu, Z.; Zhang, Y.; Zhang, G.; Su, M.; Zhou, X.; Wu, X.; Sun, W.; Zhang, X.; Liu, B.; Chen, W.; Liao, Q.; Woo, H. Y.; Guo, X. A New Wide Bandgap Donor Polymer for

Efficient Nonfullerene Organic Solar Cells with a Large Open-Circuit Voltage. *Advanced Science* **2019**, *6* (21), 1901773. https://doi.org/10.1002/advs.201901773.

(50) Pavličić, D.; Koružnjak, J. D.; Banić-Tomišić, Z.; Karminski-Zamola, G. Synthesis of Some New Bis-(p-Fluorophenyl)Amides of the Thieno[3,2-b]Thiophene, Thieno[3,2-b]Furan and 1,2-Bis{5-[2-(2-Thienyl)Ethenyl]2-Thienyl}ethene Series. *Molecules* **2002**, *7* (12), 871–884. https://doi.org/10.3390/71200871.

(51) Chen, J.; Wang, L.; Yang, J.; Yang, K.; Uddin, M. A.; Tang, Y.; Zhou, X.; Liao, Q.; Yu, J.; Liu, B.; Woo, H. Y.; Guo, X. Backbone Conformation Tuning of Carboxylate-Functionalized Wide Band Gap Polymers for Efficient Non-Fullerene Organic Solar Cells. *Macromolecules* **2019**, *52* (1), 341–353. https://doi.org/10.1021/acs.macromol.8b02360.

(52) Hong, W.; Sun, B.; Aziz, H.; Park, W.-T.; Noh, Y.-Y.; Li, Y. A Conjugated Polyazine Containing Diketopyrrolopyrrole for Ambipolar Organic Thin Film Transistors. *Chem. Commun.* **2012**, *48* (67), 8413–8415. https://doi.org/10.1039/C2CC33998F.

(53) Grant, T. M.; Dindault, C.; Rice, N. A.; Swaraj, S.; Lessard, B. H. Synthetically Facile Organic Solar Cells with >4% Efficiency Using P3HT and a Silicon Phthalocyanine Non-Fullerene Acceptor. *Mater. Adv.* **2021**, *2* (8), 2594–2599. https://doi.org/10.1039/D1MA00165E.

(54) He, K.; Kumar, P.; Abd-Ellah, M.; Liu, H.; Li, X.; Zhang, Z.; Wang, J.; Li, Y. Alkyloxime Side Chain Enabled Polythiophene Donors for Efficient Organic Solar Cells. *Macromolecules* **2020**, *53* (20), 8796–8808. https://doi.org/10.1021/acs.macromol.0c01548.

(55) Marinova, N.; Valero, S.; Delgado, J. L. Organic and Perovskite Solar Cells: Working Principles, Materials and Interfaces. *Journal of Colloid and Interface Science* **2017**, *488*, 373–389. https://doi.org/10.1016/j.jcis.2016.11.021.

(56) Murgatroyd, P. N. Theory of Space-Charge-Limited Current Enhanced by Frenkel Effect. *J. Phys. D: Appl. Phys.* **1970**, *3* (2), 151–156. https://doi.org/10.1088/0022-3727/3/2/308.

(57)    Fu, Z.; Zhang, X.; Zhang, H.; Li, Y.; Zhou, H.; Zhang, Y. On the Understandings of Dielectric

Constant and Its Impacts on the Photovoltaic Efficiency in Organic Solar Cells. *Chinese Journal*

*of Chemistry* **2021**, *39* (2), 381–390. https://doi.org/10.1002/cjoc.202000289.

(58)    Wang, X.; Tang, A.; Chen, F.; Zhou, E. Ring Fusion of Thiophene–Vinylene–Thiophene (TVT)

Benefits Both Fullerene and Non-Fullerene Polymer Solar Cells. *Macromolecules* **2018**, *51*

(12), 4598–4607. https://doi.org/10.1021/acs.macromol.8b00805.

(59)    Zhang, T.; An, C.; Bi, P.; Lv, Q.; Qin, J.; Hong, L.; Cui, Y.; Zhang, S.; Hou, J. A Thiadiazole-

Based Conjugated Polymer with Ultradeep HOMO Level and Strong Electroluminescence

Enables 18.6% Efficiency in Organic Solar Cell. *Advanced Energy Materials n/a* (n/a),

2101705. https://doi.org/10.1002/aenm.202101705.

(60)    He, K.; Kumar, P.; Yuan, Y.; Zhang, Z.; Li, X.; Liu, H.; Wang, J.; Li, Y. A Wide Bandgap

Polymer Donor Composed of Benzodithiophene and Oxime-Substituted Thiophene for High-

Performance Organic Solar Cells. *ACS Appl. Mater. Interfaces* **2021**, *13* (22), 26441–26450.

https://doi.org/10.1021/acsami.1c02442.

(61)    He, Q.; Sheng, W.; Zhang, M.; Xu, G.; Zhu, P.; Zhang, H.; Yao, Z.; Gao, F.; Liu, F.; Liao, X.;

Chen, Y. Revealing Morphology Evolution in Highly Efficient Bulk Heterojunction and

Pseudo-Planar Heterojunction Solar Cells by Additives Treatment. *Advanced Energy Materials*

**2021**, *11* (7), 2003390. https://doi.org/10.1002/aenm.202003390.

(62)    A. Abdulahi, B.; Li, X.; Mone, M.; Kiros, B.; Genene, Z.; Qiao, S.; Yang, R.; Wang, E.;

Mammo, W. Structural Engineering of Pyrrolo[3,4- f ]Benzotriazole-5,7(2 H ,6 H )-Dione-

Based Polymers for Non-Fullerene Organic Solar Cells with an Efficiency over 12%. *Journal of*

*Materials Chemistry A* **2019**, *7* (33), 19522–19530. https://doi.org/10.1039/C9TA06385D.

(63)    Yeh, M.-L.; Wang, S.-Y.; Hardigree, J. F. M.; Podzorov, V.; Katz, H. E. Effect of Side Chain

Length on Film Structure and Electron Mobility of Core-Unsubstituted Pyromellitic Diimides

and Enhanced Mobility of the Dibrominated Core Using the Optimized Side Chain. *J. Mater. Chem. C* **2015**, *3* (13), 3029–3037. https://doi.org/10.1039/C4TC02611J.

(64)  Hong, J.; Kim, R.; Yun, H.; Park, J.-M.; Shin, S.; Kim, Y.-H. A Benzodithiophene-Based Semiconducting Polymer for Organic Thin Film Transistor. **2013**. https://doi.org/10.5012/BKCS.2013.34.4.1170.